University of Sussex

Single Photons from a Trapped-Ion Cavity-QED System

Thomas Walker

Submitted for the degree of Doctor of Philosophy
University of Sussex
June 2020

Declaration

I hereby declare that this thesis has not been and will not be submitted in whole or in part to another University for the award of any other degree.

Signature:

Thomas Walker

UNIVERSITY OF SUSSEX

Thomas Walker

Single Photons from a Trapped-Ion Cavity-QED System

Summary

Quantum networking is an established and growing field of research, with applications in many other fields of quantum technology, as well as fundamental research in quantum mechanics. A quantum network consists of multiple quantum devices that can interchange quantum information or be entangled with each other. Trapped ions coupled to optical cavities are among the most promising platforms in quantum technology broadly and networking specifically, with the ability to initialise and store quantum states in the ions and, via the cavity, transfer those states onto photons, which can interact with distant systems. This thesis describes two experiments using an ion trap with integrated high finesse optical cavity as a source of single photons. In the first, the photons were converted to a standard telecommunications wavelength through quantum frequency conversion and transmitted over 10 km of optical fibre. The attenuation experienced by the photons in optical fibre without frequency conversion would make transmission over such a long distance impractical. The converted photons were shown to maintain their nonclassical statistics, meaning such a system could be used to create quantum networks over long distances. A novel scheme for producing single photons from the ion-cavity system was demonstrated. This scheme significantly reduces the impact of decoherence in the system compared to commonly used schemes through selection of the initial state of the ion. This scheme may be directly applied to ion-photon entanglement and would lead to improved fidelity in ion-ion entanglement or state transfer. Both experiments represent significant steps towards the building of quantum networks based on ions coupled to optical cavities. They lay the groundwork for future experiments using the same system to entangle ions with photons and eventually with ions in other traps.

For Nan.

Acknowledgements

This thesis is is culmination of four years of learning and work. Of course I couldn't have done any of it without the help and support of the family, friends, and colleagues who have been there along the way.

I would like to begin by thanking Professor Matthias Keller, not only for his support and guidance as my supervisor, but for his belief and confidence in my abilities as a scientist, and the encouragement he's given me. It's been a pleasure working with you and learning from you. Thank you for the opportunities you've given me.

I'd like to thank my colleagues at ITCM, past and present, for their help and friendship over the years. Ours is a big research group, but everyone has helped me in some way, big or small. Thanks to the class of 2020 - Costas Christoforou, Callan Jobson, and Hamzah Shokier - and to Xavier Fernandez Gonzalvo, Laura Blackburn, Sam Snowden, David Kay, and Corentin Pignot. Thanks to our technician Alan Butler for all the work you do for us. Thanks to Hiroki Takahashi, without whom half of the lab wouldn't function. To Markus Vogt, who took me under his wing and taught me how to be a physicist, and paved the way for all the research I've been lucky enough to do. Thanks to Amy Gardner, Ezra Kassa, and Gurpeet Kaur Gulati Roy for your help when I was first starting. And special thanks to my friends and colleagues Samir Vartabi Kashanian and Travers Ward, who both put tremendous effort into our experiments while dealing with the challenges and experiencing the joys of new fatherhood. I wish all of you all the best wherever life takes you.

I would also like to mention Wolfgang Lange, who is sadly no longer with us. I only had the fortune of meeting him once, eight years ago on a visit to the university, but his warmth and enthusiasm for the subject is part of why I went into atomic physics and chose to do my master's project with ITCM. It's been an honour to work in the lab he started and to continue his research.

Thanks to all the friends who have made the last four years bearable. I can't list you all here individually but I hope you all know who you are and how much you mean to me.

I'd like to thank my parents Chris and Jenni, my brother Joe, my grandparents, and the rest of my family for their love and support. I hope I've made you proud.

The final and most important person to thank is Charlotte, my partner and best friend, without whom I wouldn't where I am today. Thank you for believing in me when I didn't believe in myself and always pushing me to be better. This wouldn't have been possible without you.

Contents

List of Figures

Chapter 1

Introduction

The development of quantum mechanics at the beginning of the 20th century led to technologies that now underpin both scientific research and daily life, from lasers to transistors, in what has become known as the quantum revolution. We are now in the early stages of a second quantum revolution, in which, rather than simply building technologies based on our understanding of underlying quantum principles, we are manipulating individual quantum objects and exploiting specific quantum effects [1]. Just seventy years after Schrödinger remarked that "we never experiment with just one electron or atom or (small) molecule" [2], it is now commonplace in labs across the world to do just that. Currently a vast array of quantum technologies are being explored on a range of platforms, from magnetometers based on Bose-Einstein condensates [3] to computer chips made of superconducting electronic circuits [4]. The basis for most quantum technologies is the qubit: a two-level quantum system analogous to the classical bit. The qubit can exist in a superposition of its two qubit states, or be entangled with other qubits. These intrinsically quantum properties open the path to quantum algorithms that can compute certain problems that are intractable on classical computers. By the 1980s it was understood that simulating quantum mechanics precisely using a classical computer comes with an exponentially growing overhead as the size of the system increases [5–7] and so a quantum approach would be required. Beginning with Benioff's proposed quantum mechanical Turing machine [8], Feynman's outlining of quantum simulation [9], and Deutsch's proposal for a universal digital quantum computer [10], quantum computing has developed into a broad and rapidly evolving field. The analogue simulation of simple Hamiltonians [11] and universal quantum simulators have been realised [12]. Beyond simulating quantum systems, a range of quantum algorithms, such as Shor's algorithm for prime factorisation [13] and Grover's search algorithm [14], offer exponential speed-up compared to classical algorithms for particular computational problems.

With the advent of quantum computers comes the need to transmit quantum information between individual processors. This is not only necessary for communication between distant devices, but also helps address the problem of scalability; many smaller interconnected nodes may act in concert to perform large computations, in what is known as distributed or modular quantum computing [15]. The natural choice for communication of quantum information is the photon, onto which information can be encoded, and which can be transmitted over long distances via optical fibres. Through these optical links, quantum networks can be built, and one can envision eventually a quantum internet of disparate and distant quantum devices [16]. To begin building a quantum network, we require not only a source of single photons but a platform for the storage and manipulation of quantum information. This platform should fulfil certain requirements, best

summarised as DiVincenzo's criteria [17]:

1. A scalable physical system with well characterized qubit
2. The ability to initialize the state of the qubits to a simple fiducial state
3. Long relevant decoherence times
4. A universal set of quantum gates
5. A qubit-specific measurement capability.

A promising candidate that meets the above criteria is the trapped ion. Ions can be confined and isolated in vacuum using electric fields, allowing their quantum properties to be studied without disturbance from the environment even at room temperature. The two qubit levels in an ionic qubit are usually two electronic states of the ion, which can be manipulated with lasers. The scalability criteria is partially fulfilled by the ability to microfabricate ion traps [18]. Trapped-ion qubit states can be prepared and read out with a fidelity of over 99.9% [19] and have coherence times typically on the order of tens of seconds, with over ten minutes being reported [20]. Qubit gates – operations performed on qubits to change their state – are the building blocks of quantum information processing. A set of gates is said to be universal if any quantum operation can be formed from a finite series of gates in that set. A universal set of gates may be implemented in ions [21], and one- and two-qubit gate fidelities of 99.99% and 99.9% respectively have been demonstrated [22]. The time taken to execute these gates is typically on the order of microseconds [23], far shorter than the coherence time of the qubit states.

Further, to be integrated into a network, the node should fulfil the following additional two criteria:

6. The ability to interconvert stationary and flying qubits.
7. The ability to faithfully transmit flying qubits between specified locations.

These properties are automatically available in a trapped ion system, which may transfer information with photons via absorption and stimulated or spontaneous emission. The efficiency of and degree of coherent control over these processes is limited, however, and thus an interface between ionic and photonic qubits which enhances these properties is desirable. Such an interface may be realised by cavity quantum electrodynamics (CQED) in the form of optical cavities [24]. Using a high-finesse optical cavity, the coupling of the ion to a particular electric field mode can be greatly enhanced, granting coherent control over the interaction. The output mode of the cavity can be matched to that of a single-mode fibre, allowing for efficient and high-fidelity interchange of quantum information between nodes. Additionally, ions are intrinsically identical, unlike solid-state qubits such as superconductors and quantum dots, meaning each node qubit in the network can be identical.

Two key approaches to quantum networking have been proposed. The earliest proposals were for deterministic networking, in which quantum information is transferred from a stationary qubit to a photon and then from the photon to another stationary qubit with a near unity probability of success [25] (see Fig. 1.1). Such an approach would require the strong coupling regime of CQED, in which the ion-cavity coupling strength is greater than any of the loss channels in the system. The strong coupling regime was recently achieved for the first time in ions [26] but remains technically challenging. The state of an ion has been successfully mapped onto a single photon [27] in a weakly coupled system, while matter-matter state transfer has been achieved with a coherent state in trapped neutral atoms, where strong coupling is technically simpler to achieve [28].

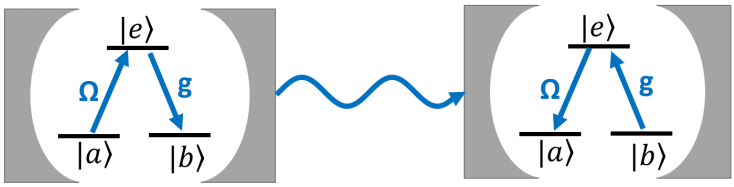

Figure 1.1: Illustration of a deterministic quantum networking scheme. A laser field denoted by Ω and cavity field g couple the qubit states $|a\rangle$ and $|b\rangle$ in the first ion-cavity system. The ion state $|\psi\rangle_{\text{atom}} = \alpha|a\rangle + \beta|b\rangle$ is mapped to the state of the photon emitted from the cavity $|\psi\rangle_{\text{photon}} = \alpha|0\rangle + \beta|1\rangle$. When this photon is absorbed by the second ion-cavity system, the photon state is mapped back onto $|\psi\rangle_{\text{atom}} = \alpha|a\rangle + \beta|b\rangle$ in the second ion.

The difficulty of achieving strong coupling and deterministic state transfer has led to the second approach: probabilistic networking. In this approach, the establishment of entanglement between distant nodes is heralded by the detection of photons. As a result, unity efficiency is no longer necessary – the process can be retried until successful [29, 30]. This approach requires speed to be sacrificed for technical simplicity, as high fidelities can be achieved even for low success probabilities. A scheme like the one shown in Fig. 1.2 was first demonstrated with trapped ions without an optical cavity with an entanglement fidelity of 63% [31]. More recently fidelities exceeding 90% have been demonstrated in similar schemes [32]. In experiments with ions emitting into free space, the photons are collected through high-numerical-aperture lenses and coupled to an optical fibre, and so the collection efficiency is limited by the solid angle of the lens and the mode matching to the fibre. In cavity-QED experiments by contrast, light is emitted directly into the cavity mode. This both increases the collection efficiency and allows for better mode matching to the fibre [33]. Ions coupled to optical cavities have been used to produce single photons [34], entangle ions with photons [35], and entangle two ions in the same trap [36].

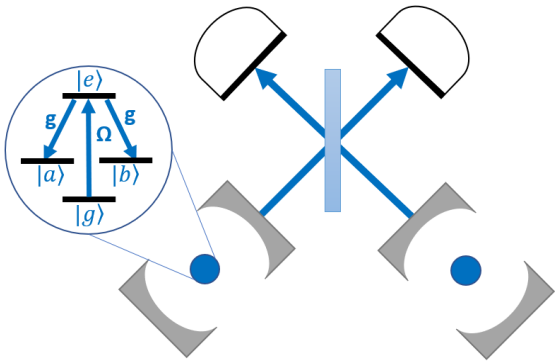

Figure 1.2: Illustration of the two-photon detection scheme for probabilistic quantum networking. Through a laser field denoted by Ω and cavity field g, an ion is put in a superposition of the qubit states $|a\rangle$ and $|b\rangle$. The polarisation of the cavity photon depends on the ion state; thus, two are in the entangled state $|\psi\rangle = (|a, H\rangle + |b, V\rangle)/\sqrt{2}$, where H and V denote orthogonal polarisation states. An identical process is performed in a second system, and the photons emitted from each system meet at a beam splitter. The photons can only leave from different ports if their polarisation is different [37]. A detection at both ports therefore projects the states of the ions onto the entangled state $|\psi\rangle = (|a, b\rangle + |b, a\rangle)/\sqrt{2}$.

Beyond their use in distributed quantum computing, single photon sources have uses in other areas

Photon Source	Wavelength	Rate	Efficiency	$g^{(2)}(0)$	V_{HOM}	refs
This work	IR, telecom	kHz	0.05	0.0017	0.81	
Ions in cavities	VIS, IR	10s kHz	0.88	0.0019	0.47	[33, 42, 43]
Atoms in cavities	VIS, IR	100s kHz	≈ 1	0.06	0.87	[44–46]
Parametric scattering	VIS, IR	MHz	0.84	0.004	0.99	[47, 48]
Quantum dots	IR, telecom	10s MHz	0.97	7.5×10^{-5}	0.9956	[47, 48]
NV centres	VIS, IR	100s kHz	0.35	0.07	0.66	[47, 48]
Four-wave mixing	IR, telecom	100s kHz	0.26	0.007	0.97	[47, 48]

Table 1.1: A comparison between several common single photon sources. The rate refers to a typical rate of generating single photons, while the efficiency is the best reported value for the probability to generate a photon on demand. $g^{(2)}(0)$ and V_{HOM} are measures of the singleness and distinguishability of the emitted photons defined later in the thesis ($g^{(2)}(0) = 0$ indicates a pure single photon source and $V_{\mathrm{HOM}} = 1$ indicates a source of indistinguishable photons) and the best reported values are given. Note that the values for a given platform were necessarily been reported simultaneously.

of quantum technology. For example, linear optical quantum computing uses photons themselves in combination with linear optics and single photon detectors for perform quantum computation[38]. They are also used in quantum key distribution to provide quantum-secured communication [39]. Both of these use cases rely on photon sources that are as ideal as possible; that is, they can produce exactly one photon in a pure, repeatable state on demand. Table 1.1 shows a comparison between the most common single photon sources and the results presented in this thesis. Based on this comparison, atoms and ions appear to be relatively underdeveloped as single photon sources, offering relatively low rates and a high degree of distinguishability compared to solid state platforms such as quantum dots. Further, the wavelength of light emitted from quantum dots can be fairly freely chosen at the manufacture stage, including telecom wavelengths [40], whereas atoms are restricted by their electronic transitions. The key advantage offered by atomic sources is that they are inherently identical, whereas great care and effort is required to manufacture an identical enough pair of quantum dots [41]. Neutral atom sources have thus far shown a higher single photon efficiency and distinguishability than ions. This is primarily due to these sources operating in the strong coupling regime, and the gap between the two platforms should shrink as technological improvements provide access to strong coupling with trapped ions. The long coherence and trapping times of ions also mean that they are more suited to act as quantum memories as well as emitters, compared to quantum dots or neutral atoms. This thesis aimed to improve upon current trapped-ion cavity photon sources in two areas: firstly, to use frequency conversion to extend the wavelength range into the telecom bands, and secondly, to produce highly indistinguishable photons.

This thesis describes a trapped-ion CQED system that can act as a node in a quantum network. Two experiments are presented which seek to improve the generation and transmission of single photons, key aspects of quantum networking. A single $^{40}Ca^{+}$ ion is confined in a linear Paul trap capable of trapping strings of ions. The cavity is colinear with the trap axis, so the entire string can be optimally coupled to the cavity simultaneously [49], allowing them to be entangled with each other [36]. In Chapter 2 the theoreticial background for the interaction of the trapped ion with laser and cavity fields is described. This framework is used to numerically simulate the dynamics of the system in the experiments. Chapter 3 covers generally the theory of ion trapping using Paul traps. Chapter 4 describes the ion trap and peripheral systems used to monitor, characterise, and run experiments using the trap. Chapter 5 covers an experiment demonstrating the transmission of single photons from a trapped ion over ten kilometres of optical fibre. This was achieved

by converting the photons to a standard telecom wavelength via quantum frequency conversion (QFC), the first instance of QFC being used with such a system. The implementation of QFC will prove vital in the construction of long-range quantum networks incorporating a variety of quantum devices. Chapter 6 presents a novel scheme for producing single photons in a CQED system and details an experiment carried out to demonstrate that this scheme produces photons with a greater degree of indistinguishability than more standard techniques. The indistinguishability of photons impacts the fidelity of quantum communication in both the deterministic and probabilistic schemes. The final chapter presents a summary and an outlook for future work.

Chapter 2

Atom-Light Interactions

This chapter describes the dynamics of the $^{40}Ca^{+}$ ion coupled to a bimodal optical cavity and how they are numerically simulated. Starting with a two-level atom coupled to a classical field, the full Hamiltonian of the ion-cavity system is built. A quantised cavity field is introduced, and the atom is expanded to a three-level system. The cavity STIRAP for producing single photons is described. The master equation formulation is used to include decay processes in the system, which is be solved numerically to simulate the system. The simulations were written using the Quantum Optics Toolbox in Python (QuTiP) [50] as part of the work for this thesis, based on previous code written for the MATLAB quantum optics toolbox [51] to model the $^{40}Ca^{+}$-cavity system.

The correlation functions used to describe the statistical properties of light are also introduced. These functions form the basis of the two experiments presented in this thesis. It is shown how they are numerically calculated by the same method that is used to simulate the atom-cavity system.

2.1 The Two-Level Atom

The simplest atomic system is the two-level atom (TLA). The total energy for a system of two levels, a ground state $|g\rangle$ with energy E_g, and excited state $|e\rangle$ with energy E_e, is

$$\hat{H}_0 = E_g |g\rangle \langle g| + E_e |e\rangle \langle e| . \tag{2.1.1}$$

Setting the energy of the ground state as 0, this becomes

$$\hat{H}_0 = \hbar\omega_0 \hat{\sigma}_{ee}, \tag{2.1.2}$$

where $\omega_0 = (E_e - E_g)/\hbar$ and $\hat{\sigma}_{ee} = |e\rangle \langle e|$. The state of the TLA can be written as

$$|\psi\rangle = \alpha |g\rangle + \beta |e\rangle , \tag{2.1.3}$$

where α and β are the complex probability amplitudes of the basis states.

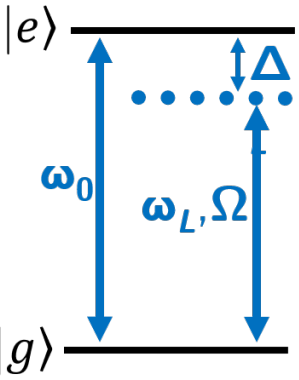

Figure 2.1: A two-level atom, with levels $|g\rangle$ and $|e\rangle$ separated by an energy $\hbar\omega_0$ and interacting with a laser with Rabi frequency Ω and frequency ω_L. The detuning of the laser $\Delta_L = \omega_0 - \omega_L$ is also indicated.

2.1.1 Coupling the levels with a classical field

The two levels may be coupled by way of an electric field, $\boldsymbol{E}(z,t)$. A classical monochromatic electric field with angular frequency ω_L, polarised along $\boldsymbol{\epsilon}$, is described by

$$\boldsymbol{E}(z,t) = \boldsymbol{\epsilon} E_0 \cos(\omega_L t - kz), \tag{2.1.4}$$

where E_0 is the amplitude of the field at the position of the atom. As optical wavelengths are significantly larger than the Bohr radius of a typical atom, we may take the dipole approximation, neglecting the spatial variation of the electric field. The electric field may therefore be rewritten as

$$\boldsymbol{E}(t) = \boldsymbol{\epsilon} E_0 \left(e^{i\omega_L t} + e^{-i\omega_L t}\right). \tag{2.1.5}$$

Modelling the atom as a dipole, $\hat{\boldsymbol{d}} = -q\hat{\boldsymbol{r}}$, with q being the elementary charge and $\hat{\boldsymbol{r}}$ being the dipole position operator, the Hamiltonian describing the interaction between the atom and the laser is given by

$$H_I = -\hat{\boldsymbol{d}} \cdot \boldsymbol{E}(t). \tag{2.1.6}$$

The operator $\hat{\boldsymbol{d}}$ may be written in terms of the atomic raising and lowering operators, $\hat{\sigma}^- = |g\rangle\langle e|$ and $\hat{\sigma}^+ = |e\rangle\langle g|$:

$$\hat{\boldsymbol{d}} = \hat{\sigma}^+ \boldsymbol{d}_{eg} + \hat{\sigma}^- \boldsymbol{d}_{ge}, \tag{2.1.7}$$

with $\boldsymbol{d}_{ij} = q\langle i|\,\hat{\boldsymbol{r}}\,|j\rangle$. Introducing the Rabi frequency,

$$\Omega = \frac{1}{2\hbar}(\boldsymbol{\epsilon} \cdot \boldsymbol{d}_{eg}) E_0, \tag{2.1.8}$$

the interaction Hamiltonian can be written as

$$H_I = \frac{\hbar}{2}(\Omega\hat{\sigma}^+ + \Omega^*\hat{\sigma}^-)(e^{i\omega_L t} + e^{-i\omega_L t}). \tag{2.1.9}$$

The total Hamiltonian for the system is $H = \hat{H}_0 + \hat{H}_I$. To simplify this Hamiltonian, we move to a frame rotating at the electric field frequency using the transformation

$$\tilde{H} = \hat{U}\hat{H}\hat{U}^\dagger - i\hbar\hat{U}\frac{\mathrm{d}\hat{U}^\dagger}{\mathrm{d}t}, \tag{2.1.10}$$

where $\hat{U} = e^{i\omega_L t\hat{\sigma}_{ee}}$. In this new frame, bare atomic Hamiltonian $\hat{H}_0$ becomes

$$\tilde{H}_0 = \hbar(\omega_L - \omega_0)\hat{\sigma}_{ee}. \tag{2.1.11}$$

The interaction term becomes

$$\tilde{H}_I = \frac{\hbar}{2}\left(\Omega\hat{\sigma}^+ + \Omega^* e^{-i2\omega_L t}\hat{\sigma}^-\right) + \text{h.c.} \tag{2.1.12}$$

where h.c. denotes the Hermitian conjugate. In the case that the laser frequency is similar to the atomic frequency ($\omega_L \approx \omega_0$), we can assume that the fast oscillating $2\omega_L$ terms have little impact on the system dynamics and can be neglected. This is known as the rotating wave approximation (RWA). Assuming a real Rabi frequency, the interaction part of the Hamiltonian in the RWA is

$$\tilde{H}_I = \frac{\hbar\Omega}{2}\left(\hat{\sigma}^+ + \hat{\sigma}^-\right). \tag{2.1.13}$$

We now have the full Hamiltonian in a time-independent form:

$$\begin{aligned}\hat{H} &= \hat{H}_0 + \hat{H}_I \\ &= \hbar\Delta\hat{\sigma}_{ee} + \frac{\hbar\Omega}{2}\left(\hat{\sigma}^+ + \hat{\sigma}^-\right),\end{aligned} \tag{2.1.14}$$

where we have introduced the detuning $\Delta = \omega_L - \omega_0$ and dropped the tilde notation. When the laser is on resonance with the atomic transition ($\omega_L = \omega_0$), the atomic population will oscillate between the two levels at the Rabi frequency through absorption and stimulated emission, in a process known as Rabi flopping. The generalised Rabi frequency $\tilde{\Omega} = \sqrt{|\Omega|^2 + \Delta^2}$ describes the frequency of oscillations when the laser is detuned.

2.1.2 The Jaynes-Cummings Hamiltonian

While the interaction of the atom and lasers used in our experiments may be handled semiclassically, with a classical electric field, we are interested in the quantum dynamics of the interaction between atom and an optical cavity. To describe this, we need to quantise our description of the electromagnetic field. The electric field as a function of position $\boldsymbol{r}$ is given by

$$\hat{\boldsymbol{E}}(\boldsymbol{r}, t) = \sum_{\boldsymbol{k},\nu} \sqrt{\frac{\hbar}{2\omega_{\boldsymbol{k}}\varepsilon_0 V}}\boldsymbol{\epsilon}_\nu u(\boldsymbol{r})\left(\hat{a}_{\boldsymbol{k}} e^{-i(\omega_{\boldsymbol{k}} t - \boldsymbol{k}\cdot\boldsymbol{r})} + \hat{a}^\dagger_{\boldsymbol{k}} e^{i(\omega_{\boldsymbol{k}} t - \boldsymbol{k}\cdot\boldsymbol{r})}\right). \tag{2.1.15}$$

V is the mode volume $V = \int |u(\boldsymbol{r})|^2 d\boldsymbol{r}$. $\hat{a}^\dagger_{\boldsymbol{k}}$ and $\hat{a}_{\boldsymbol{k}}$ are the creation and annihilation operators for the wavevector $\boldsymbol{k}$, which act on the number state $|n\rangle_{\boldsymbol{k}}$ as $\hat{a}^\dagger_{\boldsymbol{k}}|n\rangle_{\boldsymbol{k}} = \sqrt{n+1}\,|n+1\rangle_{\boldsymbol{k}}$ and $\hat{a}_{\boldsymbol{k}}|n\rangle_{\boldsymbol{k}} = \sqrt{n}\,|n-1\rangle_{\boldsymbol{k}}$. $u(\boldsymbol{r})$ describes the spacial profile of the field. $\nu = 1, 2$ gives two orthonormal polarisation modes $\boldsymbol{\epsilon}_{1,2}$.

The Hamiltonian for the field is

$$\hat{H}_{\text{Field}} = \sum_{\boldsymbol{k}} \hbar\omega_{\boldsymbol{k}}\left(\hat{a}^\dagger_{\boldsymbol{k}}\hat{a}_{\boldsymbol{k}} + \frac{1}{2}\right), \tag{2.1.16}$$

where $\hbar\omega_{\boldsymbol{k}}$ is the energy of a single excitation of the mode $\hat{a}_{\boldsymbol{k}}$. A two-level atom placed in the field

will interact with this field similar to the case of the classical field above:

$$\hat{H}_I = -\hat{\boldsymbol{d}} \cdot \boldsymbol{E}(t) = \hbar \sum_{\boldsymbol{k}} g_{\boldsymbol{k}}(\boldsymbol{r}) \left(\hat{\sigma}^+ + \hat{\sigma}^-\right) \left(\hat{a}_{\boldsymbol{k}} e^{-i\omega_{\boldsymbol{k}} t} + \hat{a}^\dagger_{\boldsymbol{k}} e^{-i\omega_{\boldsymbol{k}} t}\right). \tag{2.1.17}$$

where we have introduced the mode coupling strength

$$g_{\boldsymbol{k}}(\boldsymbol{r}) = u(\boldsymbol{r}) \sqrt{\frac{k\omega_{\boldsymbol{k}}^2}{2\hbar\varepsilon_0 c V}} \boldsymbol{d} \cdot \boldsymbol{\epsilon}. \tag{2.1.18}$$

Using a high-finesse optical cavity with properly chosen parameters, it is possible to enhance the coupling of the atom to a single mode of the electric field by reducing the effective mode volume. Considering a single polarisation mode and a single frequency ω_c, the Hamiltonian of the cavity field is

$$\hat{H}_c = \hbar\omega_c \left(\hat{a}^\dagger \hat{a} + \frac{1}{2}\right), \tag{2.1.19}$$

This is the form of the simple quantum harmonic oscillator. The $\frac{1}{2}$ factor represents the vacuum energy and is disregarded by shifting the zero-point by $\hbar\omega_c/2$. The eigenstates of the cavity are the photon number states $|n\rangle$ with energies

$$E_n = \hbar\omega_c \left(n + \frac{1}{2}\right). \tag{2.1.20}$$

Considering only this single mode, the interaction Hamiltonian reduces to

$$\hat{H}_I = \hbar g(\boldsymbol{r}) \left(\hat{\sigma}^+ + \hat{\sigma}^-\right) \left(\hat{a} e^{-i\omega_c t} + \hat{a}^\dagger e^{-i\omega_c t}\right). \tag{2.1.21}$$

We now assume the atom sits at the peak of the field intensity and drop the position dependence. By taking the rotating wave approximation as previously, we may neglect the $\hat{\sigma}^+\hat{a}^\dagger$ and $\hat{\sigma}^-\hat{a}$ terms, and are left with

$$H_I = \hbar g \left(\hat{\sigma}^+ \hat{a} + \hat{\sigma}^- \hat{a}^\dagger\right) \tag{2.1.22}$$

with

$$g = \sqrt{\frac{d_{eg}^2 \omega_c}{2\hbar\varepsilon_0 V}}. \tag{2.1.23}$$

The Hamiltonian of the TLA-cavity system is then

$$\begin{aligned} \hat{H} &= \hat{H}_0 + \hat{H}_I && (2.1.24)\\ &= \hat{H}_{\text{atom}} + \hat{H}_c + \hat{H}_I && (2.1.25)\\ &= \hbar\omega_0 \hat{\sigma}_{ee} + \hbar\omega_c \hat{a}^\dagger \hat{a} + \hbar g(\hat{a}^\dagger \hat{\sigma}^- + \hat{a}\hat{\sigma}^+) && (2.1.26) \end{aligned}$$

This is the well-known Jaynes-Cummings Hamiltonian. The eigenstates of the bare atom-cavity Hamiltonian $\hat{H}_0$ with n excitations are $|g, n\rangle$ and $|e, n-1\rangle$, separated by the cavity detuning $\Delta = \omega_0 - \omega_c$. As the experiments detailed in this thesis deal with a single-photon source, it is sufficient to truncate the photon number space to a single excitation; that is, $n = 0, 1$. The states of the Jaynes-Cummings model are shown in Fig. 2.2.

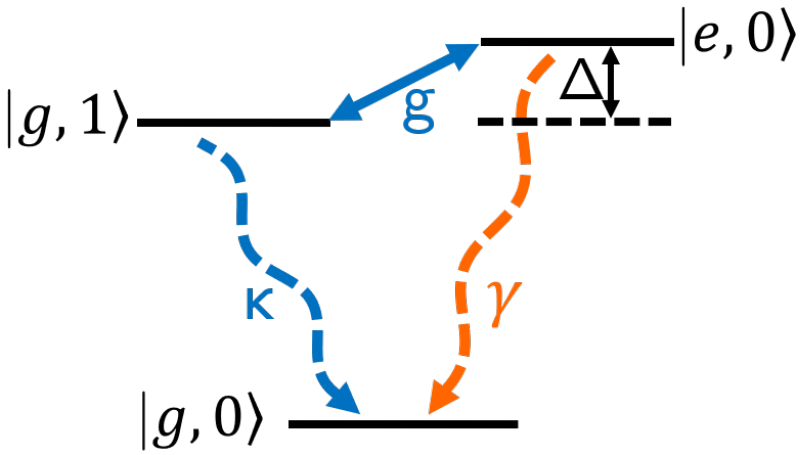

Figure 2.2: The Jaynes-Cummings model showing the bare states up to $n = 1$, including the atomic and cavity decay rates γ and κ.

2.2 Dissipation

We can find the evolution of the closed atom-cavity system by solving the Schrödinger equation:

$$i\hbar\frac{d}{dt}|\psi\rangle = \hat{H}|\psi\rangle\,. \tag{2.2.1}$$

Here, the evolution is coherent, and no energy is gained or lost by the system. In reality, we must account for the coupling of the system to the environment. The environment acts a bath to which energy can be lost, but which will not put energy into the system. We can now no longer use a quantum state $|\psi\rangle$ to describe the evolution of the system; we must instead use a density matrix for the combined system and environment $\rho_{\text{tot}} = \sum_n p_n |\psi_n\rangle\langle\psi_n|$, describing a probability distribution of states $|\psi_n\rangle$. The time evolution of the density matrix is given by the master equation, which here takes the form of the von Neumann equation:

$$\frac{\mathrm{d}}{\mathrm{d}t}\hat{\rho}_{\text{tot}} = -\frac{i}{\hbar}[\hat{H}_{\text{tot}}, \hat{\rho}_{\text{tot}}]. \tag{2.2.2}$$

We can decompose the total Hamiltonian into that of the system, the environment, and the interaction between them:

$$\hat{H}_{\text{tot}} = \hat{H}_{\text{sys}} + \hat{H}_{\text{env}} + \hat{H}_{\text{int}}. \tag{2.2.3}$$

Provided the interaction between environment and system is weak and that the environment acts as a bath (Born approximation), that correlations in the environment decay faster than the time-scales of the system dynamics (Markov approximation), and that the transition frequencies of the system are much faster than the time-scales of the system dynamics (secular approximation), we may reduce the total density matrix to that of the system by taking a partial trace: $\rho_{\text{sys}} = \text{Tr}_{\text{env}}[\rho_{\text{tot}}]$. This leaves us with the Lindblad form of the master equation:

$$\frac{\mathrm{d}\hat{\rho}}{\mathrm{d}t} = -\frac{i}{\hbar}[\hat{H}, \rho] + \frac{1}{2}\sum_n \left[2\hat{C}_n\rho\hat{C}_n^{+} - \hat{\rho}\hat{C}_n^{\dagger}\hat{C}_n - \hat{C}_n^{\dagger}\hat{C}_n\hat{\rho}\right]. \tag{2.2.4}$$

This essentially splits the total system into unitary and non-unitary parts. $\hat{H}$ and ρ are the Hamiltonian and density matrix for the atom-cavity system, and the C terms are collapse operators, which describe the ways in which the system loses energy to the environment. These collapse

operators take the form $C_n = \sqrt{2\gamma_n}A_n$, where A_n is an operator describing a quantum jump and $2\gamma_n$ is the rate at which the jumps occur.

The atom-cavity system has two means of coupling to the environment. The first is the atom's coupling to the vacuum field. When deriving the Jaynes-Cummings Hamiltonian, we neglected the coupling of the atom to all but one mode of the free space field. While the coupling any particular mode is vanishingly small, summing all the modes leads to a non-negligible coupling. This gives rise to the irreversible process of spontaneous emission; an atom may emit a photon into the bath, but has an effectively zero probability of reabsorption. The rate of spontaneous emission is given by

$$\gamma = \frac{\omega_0^3 d_{eg}^2}{3\pi\varepsilon_0\hbar c^3}. \tag{2.2.5}$$

$\Gamma = 2\gamma$ is the natural linewidth of the transition. The operator describing the decay is the atomic lowering operator, which projects the atom from the excited state to the ground state and so the corresponding collapse operator is

$$C_{\text{spon}} = \sqrt{2\gamma}\hat{\sigma}^-. \tag{2.2.6}$$

The second way the system couples to the environment is through photons leaving the cavity, either via transmission through the mirrors, scattering from imperfections in the mirror surfaces, or absorption by the mirrors. Loss through this channel is described by the photon annihilation operator $\hat{a}$. The rate of this loss from the cavity, κ, is equal to the half-linewidth of the cavity. The collapse operator for the cavity decay is then

$$C_{\text{cav}} = \sqrt{2\kappa}\hat{a}, \tag{2.2.7}$$

Through these decay channels, the states $|g,1\rangle$ and $|e,0\rangle$ are coupled to the ground state $|g,0\rangle$. If no laser is present to couple the states $|g,0\rangle$ and $|e,0\rangle$, the system will eventually decay to this state, where the evolution will cease.

The dynamics of the atom-cavity system vary greatly depending on the relative strengths of the coherent and incoherent couplings. If the cavity coupling rate is greater than the dissipation rates ($g \gg \gamma, \kappa$), the strong coupling regime, the dynamics are dominated by the vacuum Rabi oscillations discussed previously. If either of the dissipation rates are greater than the cavity coupling, the system is said to be in the weak coupling regime. The weak coupling regime can be divided into two limits: the bad cavity limit, $\kappa \gg g, \gamma$, and the bad atom limit, $\gamma \gg g, \kappa$, where the dynamics are dominated by the cavity decay and spontaneous emission processes, respectively. The system described in this thesis is in the bad atom limit, with $\gamma \gg g > \kappa$.

2.3 The Three-Level Atom

Real atoms have more complex level schemes than the simple two-level atom, though a reduced level scheme is often sufficient to describe experiments. One common level scheme in atomic physics experiments is the three-level Λ-type system, as shown in Fig. 2.3, composed of two ground states $|S\rangle$ and $|D\rangle$, and a short-lived excited state $|P\rangle$. Lasers couple the transitions $|S\rangle \leftrightarrow |P\rangle$ and $|D\rangle \leftrightarrow |P\rangle$,, which we label the drive and repumping beams respectively, while a cavity couples the states $|D\rangle$ and $|P\rangle$. We introduce the atomic raising and lowering operators corresponding to the allowed transitions in the system: $\hat{\sigma}_{SP} = |S\rangle\langle P|, \hat{\sigma}_{DP} = |D\rangle\langle P|$, along with laser and cavity frequencies and coupling strengths $\omega_{\text{driv}}, \Omega_{\text{driv}}$, $\omega_{\text{rep}}, \Omega_{\text{rep}}$, and ω_c, g. The total Hamiltonian for

this system is

$$\hat{H} = \hat{H}_0 + \hat{H}_{\text{driv}} + \hat{H}_{\text{rep}} + \hat{H}_c, \tag{2.3.1}$$

$$\hat{H}_0 = E_S\hat{\sigma}_{SS} + E_P\hat{\sigma}_{PP} + E_D\hat{\sigma}_{DD} + \hbar\omega_c\hat{a}^\dagger\hat{a}, \tag{2.3.2}$$

$$\hat{H}_{\text{driv}} = \frac{\hbar\Omega_{\text{driv}}}{2}\left(e^{i\omega_{\text{driv}}t} + e^{-i\omega_{\text{driv}}t}\right)\left(\hat{\sigma}_{SP} + \hat{\sigma}_{PS}\right), \tag{2.3.3}$$

$$\hat{H}_{\text{rep}} = \frac{\hbar\Omega_{\text{rep}}}{2}\left(e^{i\omega_{\text{rep}}t} + e^{-i\omega_{\text{rep}}t}\right)\left(\hat{\sigma}_{DP} + \hat{\sigma}_{PD}\right), \tag{2.3.4}$$

$$\hat{H}_c = \hbar g\left(\hat{a}^\dagger + \hat{a}\right)\left(\hat{\sigma}_{DP} + \hat{\sigma}_{PD}\right). \tag{2.3.5}$$

As with the TLA, we can simplify this Hamiltonian and remove the time dependence by moving

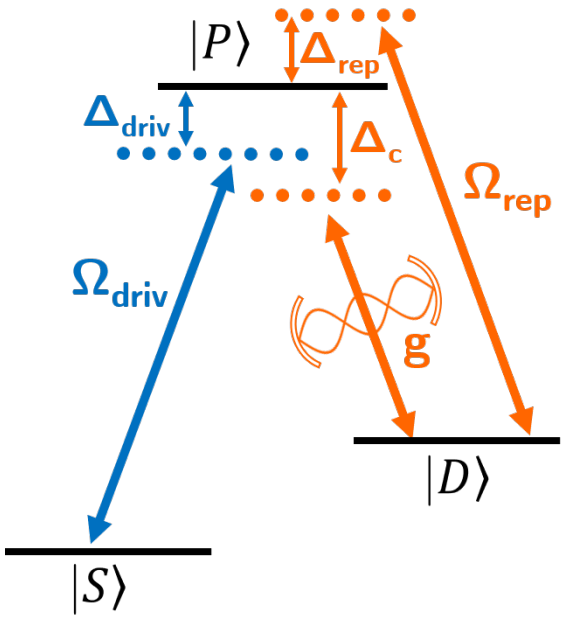

Figure 2.3: A three-level atom, with levels $|S\rangle$, $|P\rangle$, and $|D\rangle$. The state $|P\rangle$ is coupled to the state $|S\rangle$ by a laser of Rabi frequency Ω_{driv} and detuning Δ_{driv} and to the state $|D\rangle$ by a cavity of coupling strength g and detuning Δ_c and a laser of Rabi frequency Ω_{rep} and detuning Δ_{rep}.

to the interaction picture and taking the rotating wave approximation. We apply three rotations:

$$\hat{U} = \exp\left(i\hat{a}^\dagger\hat{a}\omega_{\text{rep}}t\right)\exp(i\hat{\sigma}_{DD}\omega_{\text{rep}}t)\exp(i\hat{\sigma}_{SS}\omega_{\text{driv}}). \tag{2.3.6}$$

With E_P as our reference energy, the total Hamiltonian becomes

$$\hat{H}_0 = \hbar\left(\Delta_{\text{driv}}\hat{\sigma}_{SS} + \Delta_{\text{rep}}\hat{\sigma}_{DD} + (\Delta_c - \Delta_{\text{rep}})\hat{a}^\dagger\hat{a}\right), \tag{2.3.7}$$

$$\hat{H}_{\text{driv}} = \frac{\hbar\Omega_{\text{driv}}}{2}\hat{\sigma}_{SP} + \text{h.c.}, \tag{2.3.8}$$

$$\hat{H}_{\text{rep}} = \frac{\hbar\Omega_{\text{rep}}}{2}\hat{\sigma}_{DP} + \text{h.c.}, \tag{2.3.9}$$

$$\hat{H}_c = \hbar g(\hat{a}^\dagger\hat{\sigma}_{DP} + \hat{a}\hat{\sigma}_{PD}), \tag{2.3.10}$$

$$\tag{2.3.11}$$

with laser and cavity detunings

$$\Delta_{\text{driv}} = \frac{E_S - E_P}{\hbar} - \omega_{\text{driv}}, \tag{2.3.12}$$

$$\Delta_{\text{rep}} = \frac{E_D - E_P}{\hbar} - \omega_{\text{rep}}, \tag{2.3.13}$$

$$\Delta_c = \frac{E_D - E_P}{\hbar} - \omega_c. \tag{2.3.14}$$

$$\tag{2.3.15}$$

2.3.1 Single photons

The Λ system may be used an ideal source of single photons emitted from the cavity [34, 52, 53]. Starting with the atom prepared in the $|S\rangle$ state with no photon in the cavity, the atom is coherently transferred to the $|D\rangle$ state while exciting a photon in the cavity. The scheme is shown in Fig. 2.4. Let us assume the repumping laser is off ($\Omega_{\text{rep}} = 0$). As the cavity only couples states with unequal photon number, the atom-cavity system may exist in the states $|S,0\rangle$, $|P,0\rangle$, or $|D,1\rangle$. When the drive field and cavity have equal detuning, known as the Raman resonance condition, an effective coherent coupling is created between states $|S,0\rangle$ and $|D,1\rangle$. The state of the atom-cavity system interacting with the laser can be written in terms of the dressed states:

$$|a^0\rangle = \cos\theta\,|S,0\rangle - \sin\theta\,|D,1\rangle \tag{2.3.16}$$

$$|a^+\rangle = \cos\phi\sin\theta\,|S,0\rangle - \sin\phi\,|P,0\rangle + \cos\phi\cos\theta\,|D,1\rangle \tag{2.3.17}$$

$$|a^-\rangle = \sin\phi\sin\theta\,|S,0\rangle - \cos\phi\,|P,0\rangle + \sin\phi\cos\theta\,|D,1\rangle\,. \tag{2.3.18}$$

where θ and ϕ are

$$\tan\theta = \frac{\Omega_{\text{driv}}}{2g} \quad \text{and} \quad \tan\phi = \frac{\sqrt{4g^2 + \Omega_{\text{driv}}^2}}{\sqrt{4g^2 + \Omega_{\text{driv}}^2 + \Delta^2} - \Delta}. \tag{2.3.19}$$

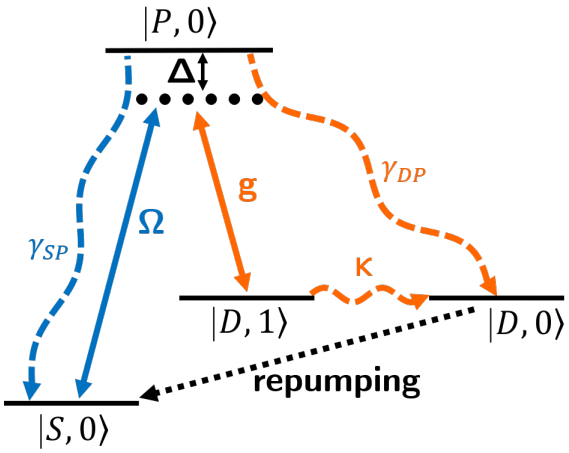

Figure 2.4: The level scheme for the cavity-STIRAP process. The atom-cavity system is coherently transferred from $|S,0\rangle$ to $|D,1\rangle$ by a laser with Rabi frequency Ω and a cavity with coupling g. Decoherence processes with rates γ_{SP}, γ_{DP}, and κ are shown. The atom may be repumped to state $|S,0\rangle$ to reset the system.

Preparing the ion in state $|S,0\rangle$ with $\Omega_{\text{driv}} = 0$ is equivalent to preparing the system in $|a^0\rangle$ with $\theta = 0$. If we now introduce a time dependence to the drive beam Rabi frequency, we may vary the mixing angle θ from 0 to $\pi/2$ ($\Omega_{\text{driv}} \gg 2g$) and transfer the system to the state $|D,1\rangle$. If

$\Omega_{\text{driv}}(t)$ is varied slowly, the system evolves adiabatically and remains in the dressed state $|a^0\rangle$, and thus the excited state will not be populated. The system will eventually decay to the state $|D,0\rangle$ through the cavity decay channel, emitting photon from the cavity. From here the system stops evolving, ensuring no more than a single photon can be emitted. This process is the cavity-stimulated adiabatic Raman passage (cavity-STIRAP) [54]. The cavity-STIRAP process is a type of cavity- or vacuum-stimulated Raman transition, though this term is sometimes reserved for the related process in which the excited state is adiabatically eliminated by detuning the laser and cavity far from resonance [55]. The repumping laser may be used to prepare the atom in the $|S,0\rangle$. In this way, the system can produce a stream of single photons through a repeating sequence of STIRAP and repumping.

The condition for adiabaticity is

$$\frac{\mathrm{d}}{\mathrm{d}t}|\theta| \ll \left|\omega^0 - \omega^{\pm}\right|. \tag{2.3.20}$$

For a Gaussian-shaped pulse of width $\Delta\tau$ and peak amplitude Ω_0, the adiabaticity condition is fulfilled for

$$\Delta\tau g,\ \Delta\tau\Omega_0 \gg 1. \tag{2.3.21}$$

The evolution must also occur slowly enough that the photon has time to decay from the cavity ($\Delta\tau > (2\kappa)^{-1}$). If the process occurs too quickly the atom will move back to the $|S,0\rangle$ state before the photon decays from the cavity. If the process occurs much slower than the cavity decay time, the emitted photon shape will closely follow that of the drive beam. Cavity-STIRAP may therefore be used to produce near-arbitrary photon shapes with high efficiency [46]. We must also consider the effect of spontaneous emission. In the absence of spontaneous emission, this scheme is entirely coherent, with the probability of producing a single photon governed only by the mixing angle θ and adiabaticity of the process. While the Raman transition does not populate $|P,0\rangle$, the cavity decay diminishes the coherence between $|S,0\rangle$ and $|D,1\rangle$, projecting the system onto the dressed states $|a^{\pm}\rangle$, which include $|P,0\rangle$. From here, spontaneous emission comes into play. The decay γ_{SP} projects the system onto the $|S,0\rangle$ state, diminishing further the coherence between $|S,0\rangle$ and $|D,1\rangle$, while γ_{DP} projects the system onto the state $|D,0\rangle$ without producing a cavity photon, where it no longer interacts with the laser or cavity. This limits the success probability of the Raman process. The effects of spontaneous emission are explored in greater detail in Chapter 6.

The cavity-STIRAP process can be used in both the deterministic and probabilistic quantum networking approaches outlined Chapter 1. An arbitrary atomic superposition state

$$|\psi_i\rangle = \alpha\,|S\rangle + \beta\,|D\rangle\,, \tag{2.3.22}$$

can be transformed to

$$|\psi\rangle = |D,0\rangle \otimes (\alpha\,|0\rangle_{\text{out}} + \beta\,|1\rangle_{\text{out}})\,. \tag{2.3.23}$$

where $|\psi\rangle_{\text{out}}$ is the state of the cavity output mode. If this photon is absorbed by an identical atom-cavity system, and a time-reversed drive pulse $\Omega_{\text{driv}}(-t)$ is applied, the state $|\psi_i\rangle$ will be written to the second atom, allowing for deterministic quantum state transfer. For the probabilistic scheme, two cavity STIRAP processes can be driven simultaneously to two different ground states $|\uparrow\rangle$ and $|\downarrow\rangle$ such that the transitions produce photons of orthogonal polarisation H and V, leaving the atom-photon system in the maximally entangled state $|\psi\rangle = \alpha\,|\uparrow,H\rangle + \beta\,|\downarrow,V\rangle$.

2.4 The $^{40}Ca^{+}$ Ion

So far we have dealt with simple model two- and three-level systems to explore the interactions between atoms and light. We will now apply these models to the real atom used in experiments, singly-ionised calcium-40, and derive the Hamiltonian used to simulate the full ion-system. The $^{40}Ca^{+}$ ion has a level scheme well-suited to CQED experiments, with transitions readily accessible by commercially available diode lasers. The $4^2S_{1/2}$ ground state, the $4^2P_{1/2}$ excited state, and the metastable $3^2D_{3/2}$ state form a Λ system, shown in Fig. 2.5. The lifetime of the $D_{3/2}$ state is on the order of a second, far longer than other experimental processes, and so may be neglected in most cases. The $D_{3/2} \leftrightarrow P_{1/2}$ transition is chosen for the optical cavity. While the $S_{1/2} \leftrightarrow P_{1/2}$ transition has a larger dipole moment and would therefore provide a greater cavity coupling strength, it is far more technically challenging to produce high-finesse cavities at UV wavelengths than near infra-red [56]. A 397 nm laser couples the $S_{1/2}$ and $P_{1/2}$ states as a drive field and a 866 nm laser is used as the repumper. This system is well established as a source of single photons [33, 34].

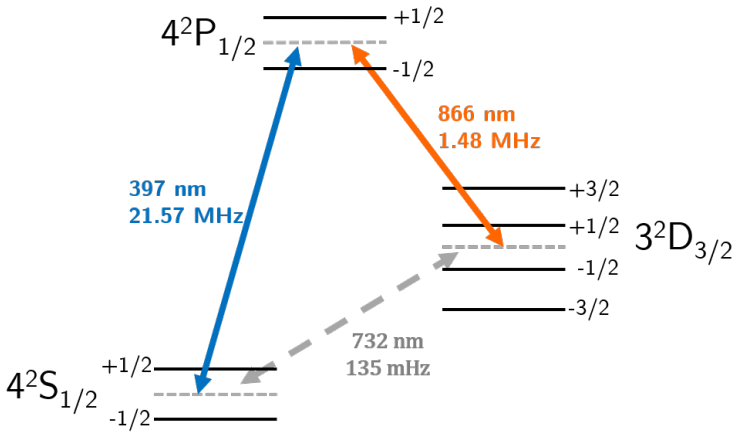

Figure 2.5: The reduced energy level scheme for $^{40}Ca^{+}$ showing the Λ system formed by the $4^2S_{1/2}$, $4^2P_{1/2}$, and $3^2D_{3/2}$ levels. The Zeeman sublevels are shown, for a total of eight levels. The transition wavelengths and linewidths $\Gamma/(2\pi)$ are also shown.

Each of the atomic levels shown in Fig. 2.5 consists of $2J+1$ Zeeman sublevels $|J, m_J\rangle$, where J is the total angular momentum of the level and $m_J = -J, -J+1 ... J$. Taking these into account, the three-level Λ system is extended to an eight-level system. In the presence of a magnetic field, the degeneracy of energy levels will be lifted. The splitting of the energy levels induced by a magnetic field of strength B is

$$\Delta E_{J,m_J} = m_J g_J \mu_B B, \tag{2.4.1}$$

where μ_B is Bohr magneton and g_J is the Landé g-factor, given by

$$g_J = 1 + \frac{J(J+1) - L(L+1) + S(S+1)}{2J(J+1)}. \tag{2.4.2}$$

When the magnetic field is large enough that the splitting is greater than the laser and cavity linewidths, Raman transitions can be driven between individual Zeeman sublevels. When the splitting is small, multiple Raman transitions will be coupled simultaneously.

Considering the Zeeman structure of the atomic levels leads to the inclusion of a geometric factor in the electric dipole interaction in Eq. (2.1.6) which depends on the J and m_J numbers of the coupled levels. This factor is known as the Clebsch-Gordan coefficient of the transition. The Clebsch-

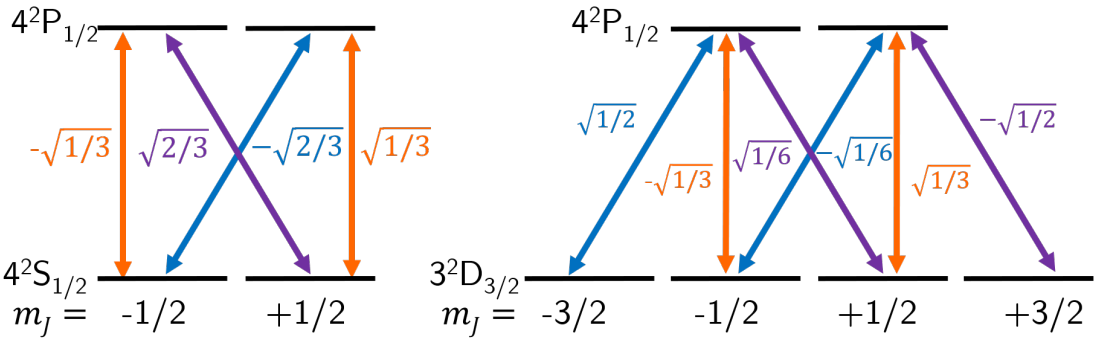

Figure 2.6: The Clebsch-Gordan coefficients for the transitions in $^{40}Ca^{+}$[57]. Transition types are indicated by colour: blue for σ^{+}, purple for σ^{-}, and orange for π.

Δm_J	Transition type	Polarisation	Cartesian coordinates
+1	σ^{+}	$\boldsymbol{\epsilon}_L$	$\boldsymbol{u}_x + i\boldsymbol{u}_y$
-1	σ^{-}	$\boldsymbol{\epsilon}_R$	$\boldsymbol{u}_x - i\boldsymbol{u}_y$
0	π	$\boldsymbol{\epsilon}_z$	$\boldsymbol{u}_z$

Table 2.1: Transition types and corresponding polarisations with the quantisation axis along the $\boldsymbol{u}_z$ direction. $\boldsymbol{\epsilon}_{L,R}$ correspond to left and right circular polarisation.

Gordan coefficients for $^{40}Ca^{+}$ are shown in Fig. 2.6. The coupling between Zeeman sublevels is reduced from the total coupling of the levels by the square of the relevant Clebsch-Gordan coefficient.

Coupling between these sublevels requires a field with the correct polarisation, determined by the difference in the m_J numbers of the sublevels. There are three transition types: σ^{+}, σ^{-}, and π, corresponding to a change in m_J of $\Delta m_J = +1, -1$, or 0. The coupling between levels depends on field's polarisation in the frame of the atom, defined by the magnetic field direction. With the magnetic field pointed along the direction $\boldsymbol{u}_z$, the photon polarisation coupling two levels with $m_J = m_a, m_b$ can be found in Table 2.1. The magnetic field in the system described in this thesis is typically aligned along the cavity axis, meaning that the cavity couples only to $\sigma^{\pm}$ transitions, which map to left- and right-circular light in the cavity. A π transition corresponds to linear light polarised along the cavity axis.

2.4.1 Ion-cavity Hamiltonian

We will now write the full Hamiltonian of the eight-level ion coupled to a cavity supporting two orthogonal polarisation modes. We model the system in the rotating frame described in Eq. (2.3.6) to obtain a time-independent Hamiltonian. As before, the full Hamiltonian can be decomposed into the bare Hamiltonian and interaction parts, $\hat{H} = \hat{H}_0 + \hat{H}_I$. The bare Hamiltonian can be further broken down in the atom, magnetic field, and cavity parts:

$$\hat{H}_0 = \hat{H}_{0,\text{atom}} + \hat{H}_{0,\text{cav}}. \tag{2.4.3}$$

The bare ion Hamiltonian, including Zeeman sublevels and the magnetic field splitting, is

$$\hat{H}_{0,\text{atom}} = \hat{H}_S + \hat{H}_D, \tag{2.4.4}$$

with

$$\hat{H}_S = \hbar \sum_{m_J} (\Delta_{\text{driv}} + m_J g_s \mu_B B) \hat{\sigma}_{S,m_J;S,m_J} \tag{2.4.5}$$

and

$$\hat{H}_D = \hbar \sum_{m_J} (\Delta_{\text{driv}} + m_J g_s \mu_B B) \hat{\sigma}_{D,m_J;D,m_J}, \tag{2.4.6}$$

where $g_{S,D}$ are the Landé g-factors for $S_{1/2}$ and $D_{3/2}$, and we have introduced the atomic operators $\sigma_{A,m_a;B,m_b} = |A, m_a\rangle \langle B, m_b|$ to describe the Zeeman sublevels. We explicitly include the two cavity polarisations $\boldsymbol{\epsilon}_L$ and $\boldsymbol{\epsilon}_R$. Each polarisation mode has its own Fock space, $|n\rangle_a$ and $|n\rangle_b$, with annihilation operators $\hat{a}$ and $\hat{b}$ that act only on the corresponding Fock space. We assume there is negligible birefringence in the cavity, so the two modes are degenerate, and that both share a cavity coupling strength g. The bare cavity Hamiltonian is then

$$\hat{H}_{0,\text{cav}} = \hbar(\Delta_c - \Delta_{\text{rep}}) \left(\hat{a}^\dagger \hat{a} + \hat{b}^\dagger \hat{b} \right) \tag{2.4.7}$$

The interaction Hamiltonian encompasses the laser and cavity interactions:

$$\hat{H}_I = \hat{H}_L + \hat{H}_c \tag{2.4.8}$$

As before, the interaction Hamiltonians are given by the scalar product between the atomic dipole operator and the electric field operator:

$$\hat{H}_I = -\hat{\boldsymbol{d}} \cdot \hat{\boldsymbol{E}}. \tag{2.4.9}$$

The dipole operator can be expanded in terms of the atomic operators:

$$\hat{\boldsymbol{d}} = \frac{1}{2} \sum_{A,B} \sum_{m_a,m_b} \boldsymbol{d}^{B,m_b}_{A,m_a} \left(\hat{\sigma}_{A,m_a;B,m_b} + \hat{\sigma}_{B,m_b;A,m_a} \right), \tag{2.4.10}$$

where $A, B = S_{1/2}, P_{1/2}, D_{3/2}$ and $\boldsymbol{d}^{B,m_b}_{A,m_a}$ is the dipole moment for the transition $A, m_a \leftrightarrow B, m_b$. $\boldsymbol{d}^{B,m_b}_{A,m_a}$ is defined as

$$\boldsymbol{d}^{B,m_b}_{A,m_a} = C^{B,m_b}_{A,m_a} \boldsymbol{\epsilon}, \tag{2.4.11}$$

where $\boldsymbol{C}^{B,m_b}_{A,m_a}$ is the Clebsch-Gordan coefficient for the transition, shown in Fig. 2.6, and $\boldsymbol{\epsilon}$ is the polarisation of the field required to couple the transition, given in Table 2.1. The laser interaction Hamiltonian can be decomposed into the parts for each laser, $\hat{H}_L = \hat{H}_{SP} + \hat{H}_{DP}$, where

$$\hat{H}_{SP} = \frac{\hbar \Omega_{\text{driv}}}{2} \sum_{m_S} \sum_{m_P} \left[\boldsymbol{\epsilon}_{\text{driv}} \cdot \boldsymbol{d}^{P,m_p}_{S,m_S} \hat{\sigma}_{P,m_P;S,m_S} + \text{h.c.} \right] \tag{2.4.12}$$

and

$$\hat{H}_{DP} = \frac{\hbar \Omega_{\text{rep}}}{2} \sum_{m_D} \sum_{m_P} \left[\boldsymbol{\epsilon}_{\text{rep}} \cdot \boldsymbol{d}^{P,m_p}_{D,m_D} \hat{\sigma}_{P,m_P DS,m_D} + \text{h.c.} \right]. \tag{2.4.13}$$

The ion-cavity interaction Hamiltonian is the sum of the interaction Hamiltonians for the two supported polarisation modes, $\hat{H}_c = \hat{H}_a + \hat{H}_b$, where

$$\hat{H}_a = \hbar g \sum_{m_D} \sum_{m_P} \left[\boldsymbol{\epsilon}_L \cdot \boldsymbol{d}^{P,m_p}_{D,m_D} \hat{\sigma}_{P,m_P;S,m_D} \hat{a} + \text{h.c.} \right]. \tag{2.4.14}$$

and

$$\hat{H}_b = \hbar g \sum_{m_D} \sum_{m_P} \left[\boldsymbol{\epsilon}_R \cdot \boldsymbol{d}^{P,m_p}_{D,m_D} \hat{\sigma}_{P,m_P;S,m_D} \hat{b} + \text{h.c.} \right]. \tag{2.4.15}$$

Dissipation

The decay processes in the system are expanded from Section 2.3 in a manner similar to the above, with the atomic decay rate modified by the Clebsch-Gordan coefficient. For a decay from A to B, with polarisation $\boldsymbol{\epsilon}$,

$$\hat{C}_{\boldsymbol{\epsilon},AB} = \sqrt{2\gamma_{AB} \left(\boldsymbol{\epsilon} \cdot \boldsymbol{d}^{B,m_b}_{A,m_a} \right)} \hat{\sigma}_{A,m_a;B,m_b}. \tag{2.4.16}$$

Each of the cavity modes has an associated collapse operator with a common rate κ:

$$\hat{C}_a = \sqrt{2\kappa}\hat{a} \tag{2.4.17}$$

and

$$\hat{C}_b = \sqrt{2\kappa}\hat{b}. \tag{2.4.18}$$

We also model the linewidth of the lasers δ_{driv} and δ_{rep} as dissipation processes. Until now we have assumed the lasers field are at a single frequency, but fluctuations in the emission frequency of real lasers lead to a frequency distribution. The result of this linewidth is a dephasing in the atomic levels, described by the operator $\sigma_{z,A} = \sum_{m_a} \sigma_{A,m_a;A,m_a}$ for a laser coupling the level $A = \mathrm{S}_{1/2}$, $\mathrm{D}_{3/2}$ to $\mathrm{P}_{1/2}$ [58]:

$$\hat{C}_{\delta,A} = \sqrt{2\delta}\sigma_{z,A}. \tag{2.4.19}$$

Extended level scheme

The ion is typically Doppler cooled on the $\mathrm{S}_{1/2} \leftrightarrow \mathrm{P}_{1/2}$ transition using a 397 nm laser due to its high branching ratio (see Section 4.2.3). Due the possibility of electromagnetically induced transparency or coherent population trapping occurring in this Λ-type system if an 866 nm laser is used on the $\mathrm{D}_{3/2} \leftrightarrow \mathrm{P}_{1/2}$ transition [59], we use the extended level scheme shown in Fig. 2.7. A 850 nm laser is used instead to excite to the $\mathrm{P}_{3/2}$ level, which decays to $\mathrm{S}_{1/2}$ with a high branching ratio. An 854 nm laser is needed to pump the population that decays into the $\mathrm{D}_{5/2}$ level. The 850 nm and 854 nm lasers are collectively referred to as the repumpers. Considering the Zeeman subelevels, the total number of atomic levels in the extended model is eighteen. The Hamiltonian can be built for the eighteen level system in the same way as described above for the eight level system. The wavelengths and linewidths for the transitions are shown in Table 2.2.

Transition	Wavelength /MHz	Linewidth $/2\pi$
$4^2\mathrm{S}_{1/2} \leftrightarrow 4^2\mathrm{P}_{1/2}$	396.847	21.57 MHz
$4^2\mathrm{S}_{1/2} \leftrightarrow 4^2\mathrm{P}_{3/2}$	393.366	21.48 MHz
$3^2\mathrm{D}_{3/2} \leftrightarrow 4^2\mathrm{P}_{1/2}$	849.802	1.482 MHz
$3^2\mathrm{D}_{3/2} \leftrightarrow 4^2\mathrm{P}_{3/2}$	854.209	152 kHz
$3^2\mathrm{D}_{5/2} \leftrightarrow 4^2\mathrm{P}_{3/2}$	866.214	1.35 MHz
$4^2\mathrm{S}_{1/2} \leftrightarrow 4^2\mathrm{D}_{3/2}$	729.147	136 mHz
$4^2\mathrm{S}_{1/2} \leftrightarrow 4^2\mathrm{D}_{5/2}$	732.389	135 mHz

Table 2.2: Wavelengths and linewidths for $^{40}\mathrm{Ca}^+$. Linewidths for the transitions involving $\mathrm{P}_{1/2}$ from [60], for the $\mathrm{P}_{3/2}$ from [61, 62], and for the $4^2\mathrm{S} \leftrightarrow 3^2\mathrm{D}$ transition from [63].

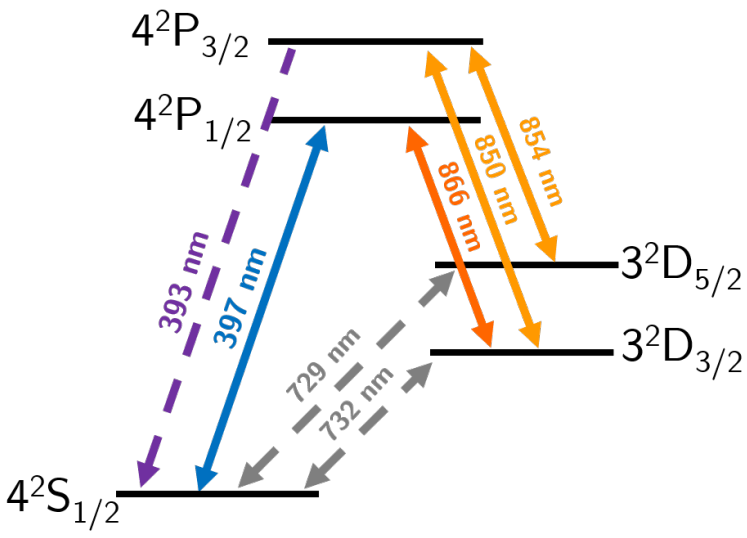

Figure 2.7: The reduced energy level scheme for $^{40}Ca^{+}$ showing the levels relevant to the experiments discussed in this thesis. Solid arrows indicate transitions addressed with lasers. The dotted arrow shows transitions not coupled by lasers in experiments. The Zeeman structure of the atomic levels is not shown.

2.5 Photon Statistics

Much of the work presented in this thesis involves examining the statistical properties of light. These statistical properties are typically described by correlation functions. Of particular interest to us are the first- and second-order two-time correlation functions, which take the forms

$$G^{(1)}_{ab}(t_1, t_2) = \left\langle \hat{a}(t_1)\hat{b}^{\dagger}(t_2) \right\rangle, \tag{2.5.1}$$

and

$$G^{(2)}_{ab}(t_1, t_2) = \left\langle \hat{a}^{\dagger}(t_1)\hat{b}^{\dagger}(t_2)\hat{b}(t_2)\hat{a}(t_1) \right\rangle, \tag{2.5.2}$$

which describe correlations between the fields $\hat{a}$ and $\hat{b}$ at times t_1 and t_2. For classical fields, the quantum mechanical ladder operators may be replaced by the complex electric field. The first-order correlation function describes correlations in the amplitudes of the fields, and therefore how well their phase relation is preserved over time. The second-order correlation function describes intensity or photon number correlations; with each field incident on a detector, it is related to the conditioned probability of detecting a photon in $\hat{b}$ at time t_2 given the detection of a photon in field $\hat{a}$ at a time t_1. Often we are interested only in the relative delay τ between the times t_1 and t_2, and so we may rewrite the correlation functions as

$$G^{(1)}_{ab}(t, t+\tau) = \left\langle \hat{a}(t)\hat{b}^{\dagger}(t+\tau) \right\rangle, \tag{2.5.3}$$

and

$$G^{(2)}_{ab}(t+\tau) = \left\langle \hat{a}^{\dagger}(t)\hat{b}^{\dagger}(t+\tau)\hat{b}(t+\tau)\hat{a}(t) \right\rangle. \tag{2.5.4}$$

We can integrate these two-time correlation functions over a period T to obtain correlation functions only in terms of the time difference τ:

$$G^{(1)}_{ab}(\tau) = \int_T \left\langle \hat{a}(t)\hat{b}^{\dagger}(t+\tau) \right\rangle dt, \tag{2.5.5}$$

and

$$G^{(2)}_{ab}(\tau) = \int_T \left\langle \hat{a}^\dagger(t)\hat{b}^\dagger(t+\tau)\hat{b}(t+\tau)\hat{a}(t) \right\rangle dt. \tag{2.5.6}$$

The integral must be taken over a long enough time to capture the relevant statistics of the fields. In the case of pulsed light, for example, it must encompass the entire optical pulse.

2.5.1 Degree of first-order coherence

The degree of first-order coherence of a field is defined by normalising the first-order auto-correlation function to the expectation value of the photon number,

$$g^{(1)}(\tau) = \int \frac{\left\langle \hat{a}(t)\hat{a}^\dagger(t+\tau) \right\rangle}{\langle \hat{n}(t) \rangle} dt. \tag{2.5.7}$$

It describes the ability of a field to interfere with itself. It gives the visibility of interference fringes in a Mach-Zehnder interferometer, for example. The value of $g^{(1)}$ ranges from 0 (incoherent) to 1 (fully coherent). The coherence time τ_c of a source is the time over which a source is considered to be coherent. After this time the phase of the field becomes unpredictable. It is calculated from the first-order coherence as

$$\tau_c = \int_{-\infty}^{\infty} |g^{(1)}(\tau)|^2 d\tau \tag{2.5.8}$$

The power spectrum of a field $F(\omega)$ is related to its first-order coherence by the Fourier transform:

$$F(\omega) = \frac{1}{2\pi} \int_{-\infty}^{\infty} g^{(1)}(\tau) e^{i\omega\tau} d\tau. \tag{2.5.9}$$

Therefore, any broadening of the frequency spectrum of a field will reduce its coherence time. The spectrum for an ideal single-frequency laser is a delta function. Its first-order coherence function therefore has the form

$$g^{(1)}(\tau) = e^{-i\omega_0\tau}. \tag{2.5.10}$$

The magnitude of this function is unity for all τ, and so the coherence time is infinite. Light undergoing homogeneous or inhomogeneous broadening will have have a Lorentzian or Gaussian frequency spectrum, respectively. This light has a first order coherence of the form

$$g^{(1)}(\tau) = e^{-i\omega_0\tau - |\tau|/\tau_c} \tag{2.5.11}$$

for a Lorentzian profile, or

$$g^{(1)}(\tau) = e^{-i\omega_0\tau - \frac{\pi}{2}(\tau/\tau_c)^2}, \tag{2.5.12}$$

for a Gaussian profile. Photons produced by the cavity-STIRAP process have a spectrum limited by the Fourier transform of their temporal profile, but they are also broadened by effects such as the drive laser frequency jitter or magnetic field noise. Thus the coherence length of these photons will be shorter than their temporal width.

2.5.2 Degree of second-order coherence

Similarly to the first-order coherence, the degree of second-order coherence of a field is defined as the normalised second-order correlation function

$$g^{(2)}(\tau) = \int dt \frac{\left\langle \hat{a}^\dagger(t)\hat{a}^\dagger(t+\tau)\hat{a}(t+\tau)\hat{a}(t)\right\rangle}{\left\langle \hat{a}^\dagger(t_1)\hat{a}(t_1)\right\rangle^2}. \tag{2.5.13}$$

In the context of photon sources, the second-order coherence of a source is the normalised probability of emitting a second photon at time τ conditioned on the emission of a first photon. A coherent laser source exhibits Poissonian statistics and no correlations in its emission. The second-order coherence is therefore unity for all τ. A single-frequency laser is thus both first- and second-order coherent. A thermal source has a second-order coherence given by

$$g^{(2)}(\tau) = 1 + \left|g^{(1)}(\tau)\right| = 1 + e^{-\tau/\tau_c}. \tag{2.5.14}$$

This gives a means to distinguish thermal and Lorentzian-broadened laser light sources, despite them having the same first-order coherence. A thermal source exhibits photon-bunching; a photon is more likely to be emitted a short time after the previous emission of a photon. We see this in the coherence function as $g^{(2)}(0) > g^{(2)}(\tau)$. Thermal light follows super-Poissonian statistics: $g^{(2)}(0) > 1$.

For all classical light, $g^{(2)}(\tau) \geq 1$ and $g^{(2)}(0) \geq g^{(2)}(\tau)$. However, non-classical source may exhibit antibunching ($g^{(2)}(0) < g^{(2)}(\tau)$) or sub-Poissonian statistics ($g^{(2)}(\tau) < 1$). A stationary Fock state with photon number n, for example, has a second-order coherence function of

$$g^{(2)}(\tau) = 1 - \frac{1}{n}, \tag{2.5.15}$$

and a two-level atom resonantly excited by a laser may exhibit photon anti-bunching in its emission. For a pure single-photon source, $g^{(2)}(0) = 0$, as there is no chance of two simultaneous photon emissions. This is equivalent to a Fock state of photon number $n = 1$.

2.6 Simulating the Ion-Cavity System

The full ion-cavity system is difficult to solve analytically, but may be solved numerically. The Lindblad master equation (Eq. (2.2.4)) can be written in terms of a single Liouvillian superoperator $\mathcal{L}$:

$$\frac{\mathrm{d}\hat{\rho}}{\mathrm{d}t} = \hat{\mathcal{L}}\hat{\rho} \tag{2.6.1}$$

Provided a known Liouvillian and initial density matrix $\rho(0)$, the system may be solved as an ordinary differential equation to find the density matrix of the system at an arbitrary time $\rho(t)$ or the steady state solution of the system. The expectation values of observables such as the atomic state or cavity population may be found as a function of time by taking the trace of the relevant operators acting on the density matrix:

$$\langle \hat{A}(t)\rangle = \mathrm{Tr}[\hat{\mathrm{A}}\hat{\rho}(\mathrm{t})]. \tag{2.6.2}$$

The populations of the atomic states are given by the expectation values of the relevant projection operator $\langle \hat{\sigma}_{A,m_a;A,m_a}\rangle$. From the cavity input-output formalism [64], the output mode of the cavity

$\hat{a}_{\text{out}}(t)$ is related to the field in the cavity $\hat{a}$ by

$$\hat{a}_{\text{out}}(t) = \sqrt{2\kappa}\hat{a}(t), \tag{2.6.3}$$

and so can be found by taken the expectation value $\langle \hat{a}(t) \rangle$. The temporal shape of the photon emitted from the cavity is similarly given by the expectation value of the number operator

$$n_{\text{out}} = 2\kappa \langle \hat{n}(t) \rangle . \tag{2.6.4}$$

The single photon efficiency – the probability of emitting a photon from the cavity – is given by

$$\eta_{\text{emit}} = 2\kappa \int \langle \hat{n}(t) \rangle \, dt. \tag{2.6.5}$$

Alternatively, a Monte Carlo method may be used to solve the system. Rather than incorporating quantum jumps into the dynamics of the system and looking at the evolution of the ensemble average as in the density matrix formalism, the Monte Carlo method looks at the unitary evolution of the state of the system and introduces quantum jumps stochastically. At each time step of the simulation, the solver determines whether a particular quantum jump has occurred by comparing the relevant decay rate to a random number, at which point the system is projected into a state determined by the collapse operator. Performing this process many times and averaging the results captures the full dynamics of the system as the number of runs tends to infinity. This formalism has the advantage of being able to extract information about the system dynamics such as when specific collapses occur.

Simulating correlation functions

First- and second-order correlation functions can also be calculated from the master equation, by the same method as the other simulations of the ion-cavity system. A first-order two-time correlation function in the Heisenberg picture has the form $\langle \hat{A}(t+\tau)\hat{B}(t) \rangle$. The quantum regression theorem [65] shows that

$$\langle \hat{A}(t+\tau)\hat{B}(t) \rangle = \text{Tr}[\hat{A}\hat{V}(t+\tau, t)\{\hat{B}\hat{\rho}(t)\}] \tag{2.6.6}$$

where $\hat{V}(t_2, t_1)$ is the propagator defined by the equation

$$\hat{\rho}(t_2) = \hat{V}(t_2, t_1)\hat{\rho}(t_1) \tag{2.6.7}$$

for the system density matrix $\hat{\rho}(t)$. $\hat{V}(t+\tau, t)\{\hat{B}\hat{\rho}(t)\}$ may then be calculated by solving the system with $\hat{B}\hat{\rho}(t)$ as the new initial density matrix. $\langle \hat{A}(t+\tau)\hat{B}(t) \rangle$ can therefore be written in terms of the initial density matrix:

$$\langle \hat{A}(t+\tau)\hat{B}(t) \rangle = \text{Tr}[\hat{A}\hat{V}(t+\tau)\{\hat{B}\hat{V}(t, 0)\{\hat{\rho}(0)\}\}]. \tag{2.6.8}$$

The time-reversed version, $\langle \hat{A}(t)\hat{B}(t+\tau) \rangle$ is given similarly by:

$$\langle \hat{A}(t)\hat{B}(t+\tau) \rangle = \text{Tr}[\hat{B}\hat{V}(t+\tau, t)\{\hat{\rho}(t)\hat{A}\}] \tag{2.6.9}$$

A similar process is used to find second-order correlation functions of the form

$$\langle \hat{A}(t)\hat{B}(t+\tau)\hat{C}(t+\tau)\hat{D}(t) \rangle = \text{Tr}[\hat{B}\hat{C}\hat{V}(t+\tau, t)\{\hat{D}\hat{\rho}(t)\hat{A}\}]. \tag{2.6.10}$$

The simulations presented in this thesis were performed using the Quantum Optics Toolbox in Python (QuTiP). This toolbox allows the evolution of quantum systems to be solved numerically provided a system Hamiltonian and collapse operators to form the Liouvillian. The full eighteen-level $^{40}Ca^{+}$ system coupled to a bimodal cavity described in this chapter has been modelled in QuTiP, though the reduced eight-level scheme is sufficient for simulating the single-photon processes. In Chapter 5, the temporal shape of the photon and emission probability are calculated. In Chapter 6, the first- and second-order coherence functions of the cavity output are calculated to simulate the Hong-Ou-Mandel interference effect.

Chapter 3

Ion Traps

This chapter describes how charged particles may be confined using electric fields. The electrode configuration of the linear Paul trap is presented, along with the equations of motion for a trapped ion. The effects of micromotion caused by stray dc fields or radiofrequency phase offsets are discussed.

3.1 The Paul Trap

To stably confine a particle to a small region of space, the particle must experience zero force at the centre of the region, and a restorative force towards the centre if the particle begins to move away. Charged particles, such as atomic ions, have the benefit over their neutral counterparts that they may be easily manipulated by means of electric fields.

Earnshaw's theorem states: "A charge acted on by electrostatic forces cannot rest in stable equilibrium" [66], meaning that it is not possible to confine an ion using only static fields. Earnshaw's theorem is readily apparent as a consequence of Laplace's equation for an electric potential Φ:

$$\frac{\partial^2\Phi}{\partial x^2} + \frac{\partial^2\Phi}{\partial y^2} + \frac{\partial^2\Phi}{\partial z^2} = 0. \tag{3.1.1}$$

We want the particle to sit at a point of potential minimum in all three dimensions. For a potential minimum in a given direction to exist, the second order derivative along that direction must be positive at zero, but for the Laplace equation to hold, there must be at least one term with a positive sign and one with a negative. Consider a quadrupole electric field:

$$\Phi(x, y, z) = \Phi_0 \left(\alpha x^2 + \beta y^2 + \gamma z^2\right). \tag{3.1.2}$$

The Laplace equation gives us

$$\Phi_0 \left(2\alpha + 2\beta + 2\gamma\right) = 0 \tag{3.1.3}$$

If any given pair of coefficients were both positive, then for Eq. (3.1.3) to hold, the third would have to be negative, and therefore there would be a maximum in the corresponding direction. Thus an ion acted upon only by electric fields will always feel a force pushing it out of the trapping region.

There are several ways around this problem. One is to combine electric fields with a magnetic field, as is the case in the Penning trap [67]. Another is the Paul trap, the type of trap used in this thesis, which uses radiofrequency (rf) electric fields to create a pseudopotential minimum that

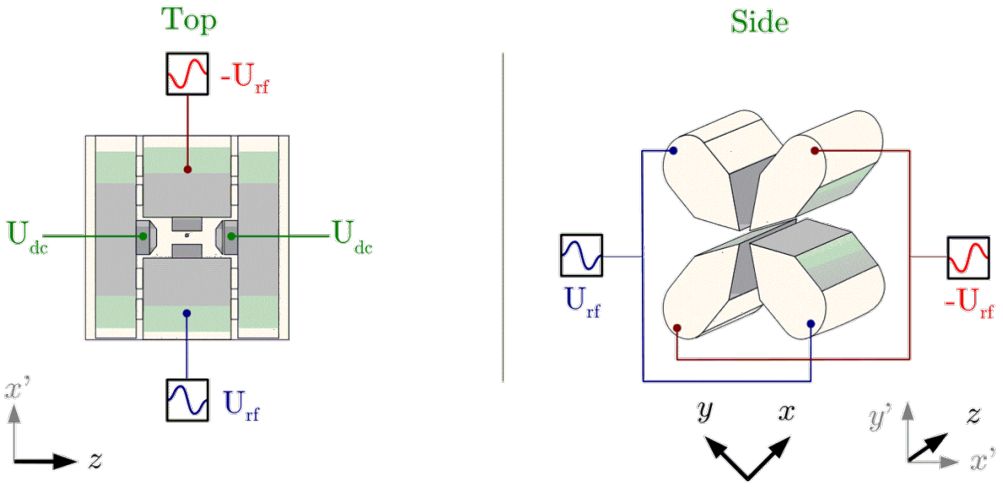

Figure 3.1: The trap electrodes, showing applied rf and dc voltages U_{rf} and U_{dc}. Diagram from [68].

keeps the ion stably localised at the trap centre, albeit with a small driven motion dependant on the strength and frequency of the rf field.

The exact mathematical description of the Paul trap depends on the particular geometry used, the choice of which depends on the particular requirements of the experiment. The trap featured in this thesis is a linear blade trap, consisting of four blade-shaped electrodes pointing inward in a cross-configuration, and two end-cap electrodes at either end of the blades. The blade electrodes define the trap axis, running parallel to the blade tips. The endcap electrodes sit on this axis pointing towards the trap centre. An rf potential of amplitude U_{rf} and frequency Ω_{rf} is applied to the blade electrodes, confining the ion to the trap axis (radial confinement), while a static potential U_{dc} is applied to the end-caps, pushing the ion to he centre of the trap (axial confinement).

The potential on the rf electrodes is given by $U(t) = U_{\mathrm{rf}} \cos(\Omega_{\mathrm{rf}} t)$. Opposing pairs of electrodes are in phase with each other and in antiphase with the other pair. The trap geometry leads to a contribution from the end-cap electrodes to the radial potential seen by the ion. The electric potential seen by a positively charged ion is

$$\phi(x, y, t) = -\frac{1}{2} U_{\mathrm{rf}} \cos(\Omega_{\mathrm{rf}} t) \left[\frac{x^2 - y^2}{r_0^2}\right] - \frac{1}{2} \eta U_{\mathrm{dc}} \left[\frac{x^2 + y^2}{z_0^2}\right]. \tag{3.1.4}$$

r_0 is the distance from the trap centre to the blade electrodes, $2z_0$ is the distance between the end-cap electrodes, and η is a geometric factor. The directions $\hat{x}$, $\hat{y}$, and $\hat{z}$ are defined in Figure 3.1.

The equations of motion in the x- and y-directions for a particle of mass m and charge Q is

$$\ddot{x} + \frac{Q}{m} \frac{\partial \phi(x, y, t)}{\partial x} = 0 \tag{3.1.5}$$

$$\ddot{y} + \frac{Q}{m} \frac{\partial \phi(x, y, t)}{\partial x} = 0 \tag{3.1.6}$$

The following substitutions are made to simplify the solution to the equation:

$$q = \frac{2QU_{\mathrm{rf}}}{m\Omega_{\mathrm{rf}}^2 r_0^2}, \tag{3.1.7}$$

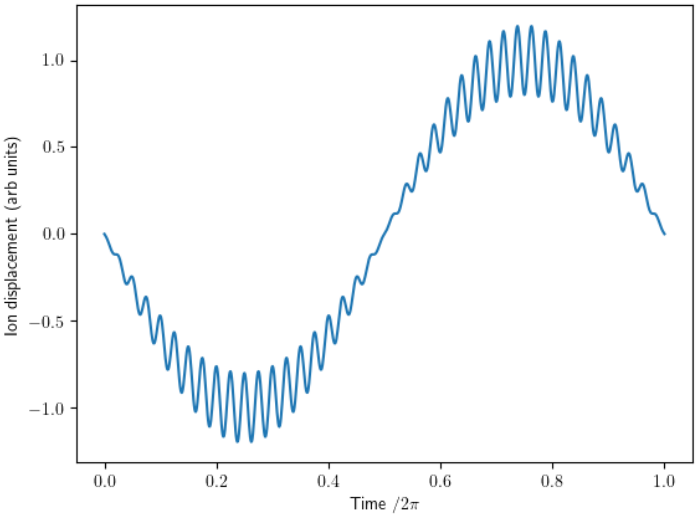

Figure 3.2: The radial motion of the ion, showing motion at the secular frequency ω_r and trap drive frequency $\Omega_{\mathrm{rf}} = 40\omega_r$. $q = 0.2$.

$$a = \frac{4\eta Q U_{\mathrm{dc}}}{m\Omega_{\mathrm{rf}}^2 z_0^2}, \tag{3.1.8}$$

and

$$\tau = \frac{\Omega_{\mathrm{rf}} t}{2}. \tag{3.1.9}$$

The equations of motion can now be written as

$$\frac{\mathrm{d}^2 x}{\mathrm{d}\tau^2} - (a - 2q\cos(2\tau))x = 0 \tag{3.1.10}$$

$$\frac{\mathrm{d}^2 y}{\mathrm{d}\tau^2} - (a + 2q\cos(2\tau))y = 0 \tag{3.1.11}$$

The equations have the form of a Mathieu equation. The Mathieu equation has stable solutions only for certain combinations of q and a, which are known as the stability parameters. Generally, $a \ll q \ll 1$ are physically realistic and provide stable motion, and so are typical in ion traps. For small displacements, the solution to the Mathieu equation is

$$x(t) = x_0(1 - q\cos(\Omega_{\mathrm{rf}} t)) \cdot \cos(\omega_r t), \tag{3.1.12}$$

where $x_0 = x(t = 0)$ and ω_r is the radial secular frequency,

$$\omega_r = \frac{\sqrt{q^2/2 + a}}{2}\Omega_{\mathrm{rf}}. \tag{3.1.13}$$

For the y-direction:

$$y(t) = y_0(1 + q\cos(\Omega_{\mathrm{rf}} t)) \cdot \cos(\omega_r t), \tag{3.1.14}$$

Here it becomes clear that the ion exhibits motion in the radial direction at both the secular and trap drive frequencies. Due to the small value of q, the slower harmonic motion at the secular frequency is dominant. The smaller motion at the trap drive frequency is known as the intrinsic micromotion of the ion. If the micromotion is neglected, the ion's motion reduces to that of a two-dimensional harmonic oscillator.

The potential in the axial direction is

$$\phi(z) = \eta U_{\mathrm{dc}} \frac{z^2}{z_0^2}. \tag{3.1.15}$$

This results in simple harmonic motion,

$$\ddot{z}(t) + \frac{a}{2}\Omega_{\mathrm{rf}}^2 z = 0, \tag{3.1.16}$$

$$z = z_0 \cos(\omega_z t), \tag{3.1.17}$$

where ω_z is the axial secular frequency,

$$\omega_z = \sqrt{\frac{a}{2}}\Omega_{\mathrm{rf}}. \tag{3.1.18}$$

3.2 Micromotion

We have already seen that the nature of the trapping field leads to intrinsic micromotion at the trap rf frequency. There also exists so-called extrinsic or excess micromotion, caused by perturbations in the trapping potential. Unlike intrinsic micromotion, extrinsic micromotion can be eliminated. The ability to eliminate micromotion is an important feature in ion trap design. The two main sources of excess micromotion are stray dc fields, and phase mismatch between the rf electrodes. Stray dc fields, which can be caused by patch potentials on the surface of the blade electrodes, lead

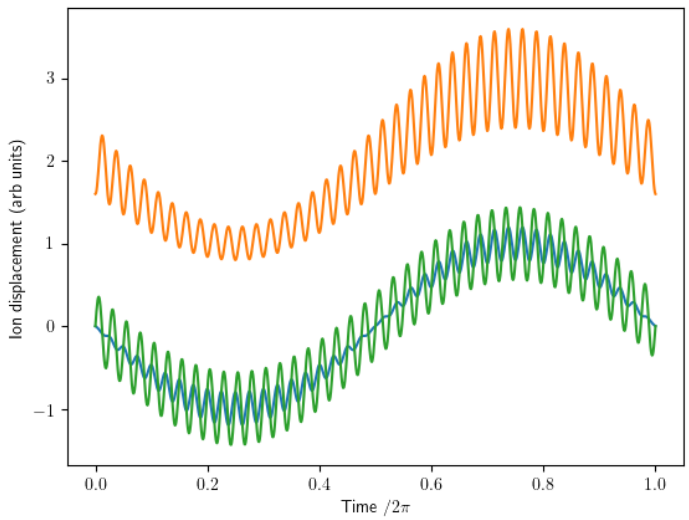

Figure 3.3: The radial motion of the ion without excess micromotion (blue), with a dc offset voltage (orange), and an rf phase mismatch (green), with motion at the secular frequency ω_r and trap drive frequency $\Omega_{\mathrm{rf}} = 40\omega_r$. $q = 0.2$.

to an offset in the ion's position from the trap rf centre. Consider a static field with magnitude E_x in the x-direction. The equation of motion becomes

$$\frac{\mathrm{d}^2 x}{\mathrm{d}t^2} + \frac{\Omega^2}{4}(a - 2q\cos(\Omega t))x = \frac{QE_x}{m}. \tag{3.2.1}$$

The solution of which is

$$x(t) = (1 - q\cos(\Omega_{\mathrm{rf}}t)) \cdot (x_{\mathrm{dc}} + x_0\cos(\omega_r t)), \tag{3.2.2}$$

with

$$x_{\mathrm{dc}} = \frac{QE_x}{m\omega_r^2}, \tag{3.2.3}$$

exhibiting a displacement of the average ion position and an additional driven motion proportional to E_x at the trap frequency. This motion may be eliminated by applying a dc voltage to the electrodes to create a field opposite to E_x.

A phase mismatch φ between the rf electrodes, which can occur due to asymmetries in the trap electronics, also leads to additional driven motion. Consider a phase φ between the electrodes along the x-axis, such that the voltages are

$$U_{1,2}(t) = U_{\mathrm{rf}}\cos\left(\Omega_{\mathrm{rf}}t \pm \frac{1}{2}\varphi\right). \tag{3.2.4}$$

For small φ, we may approximate this as

$$U_{1,2}(t) = U_{\mathrm{rf}}\cos(\Omega_{\mathrm{rf}}t) \mp \frac{1}{2}U_{\mathrm{rf}}\varphi\sin(\Omega_{\mathrm{rf}}t). \tag{3.2.5}$$

The ion's position then picks up an additional term proportional to to the phase mismatch angle: $-\frac{1}{4}qr_0\varphi\sin(\Omega_{\mathrm{rf}})$. This means that the micromotion caused by mismatched phase cannot be compensated by applying dc fields, and must instead be addressed directly. Any residual phase offset between the electrodes will therefore lead to residual micromotion.

Chapter 4

The Experimental Set-up

The work presented in this thesis was carried out using a linear Paul trap with an integrated high-finesse optical cavity, capable of trapping $^{40}Ca^{+}$ ions. The ion-trap cavity system, including vacuum chamber and trap electronics, was designed Matthias Keller and built by Nicolas Seymour-Smith, Peter Blythe and Dan Crick. Additional work was performed by Stephen Begley and Markus Vogt to improve the rf confinement of the trap and the finesse of the cavity, which involved taking the trap out of vacuum. The optics and locking systems for the lasers are the results of the work of too many project students, doctoral students, and postdocs to name. The brief description of the ion trap in Chapter 3 will be expanded upon here, along with a description of the experimental cavity and the peripheral systems for detection and lasers. A more thorough description of the trap, along with information about its construction, may be found in [68], [69], and [70].

4.1 The Ion Trap

The ion trap is a linear Paul trap, consisting of four blade-shaped electrodes providing raidal confinement and two dc endcap electrodes providing axial confinement. This trap design was chosen for its ability to trap long strings of ions in a 1D lattice, though the experiments presented here only trap a single ion at a time. The trap is housed inside a vacuum chamber shown in Fig. 4.2. All components used are ultra-high vacuum (UHV) compatible.

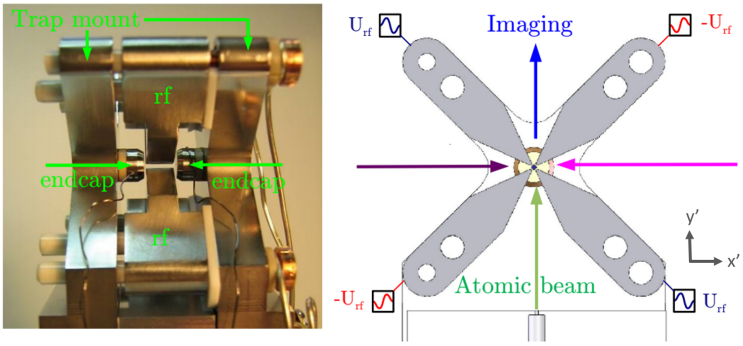

Figure 4.1: Left: Photograph of the ion trap with electrodes and trap mount indicated. Right: Schematic of the trap along the z axis. The purple and pink arrows show the direction of laser light for photoionisation and interacting with the ion. Taken from [68]

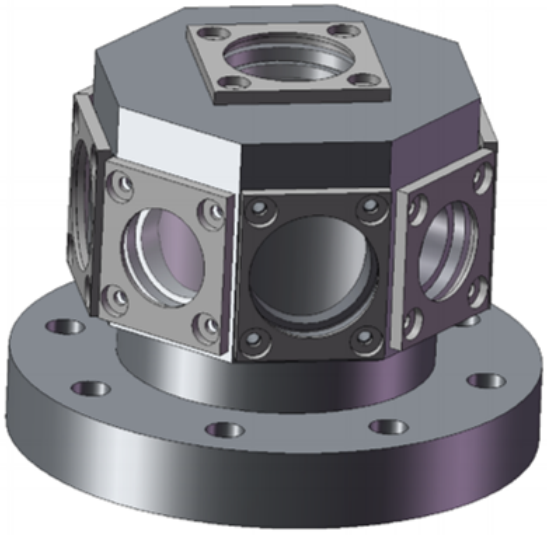

Figure 4.2: 3D CAD design of the vacuum chamber. Designed by Matthias Keller, taken from [70]

The ion trap mounting structure and electrodes Fig. 4.1 were created from a single stainless steel block through electrical discharge machining (EDM). Macor, a machinable glass-ceramic, is used for electrical isolation. Before EDM, holes were drilled for ceramic dowels and copper screws used to hold the structure together, and the fixtures were inserted to keep the structure aligned during the EDM process. The rf voltage is supplied to the blade electrodes via the screws, which are isolated from the trap mount by ceramic sleeves. The screws are connected to the rf electronics outside the trap by copper feedthroughs. Ceramic spacers further isolate the electrodes from the mount and position them at the centre of the trap structure. The distance between opposing blade electrodes is 0.93 mm.

The flattened dome-shaped end-cap electrodes are glued to PEEK (polyether ketone, a vacuum compatible plastic) mounts, which are in turn glued to the trap mount. The end-cap electrodes sit 5 mm apart. The dc voltage is supplied to the end-caps by spot-welded tantalum wires which pass through feedthroughs to the outside of the chamber. 1 mm holes are drilled in the centre of the electrodes, behind which sit the mirrors that form the optical cavity.

Below the trapping region sits an aluminium plate with a 1 mm hole in the centre. Below this hole is an oven consisting of a tube filled with grated calcium and tantalum wires spot-welded to the tube. The hole in the aluminium plate acts as a collimator for the atomic beam produced by the oven when the wires are resistively heated.

The vacuum chamber is octagonal with 1.5”-diameter, ultraviolet and infrared anti-reflection coated windows on each side for laser access and one on top for imaging and fluorescence detection. Under normal operating conditions, the pressure in the chamber is around 10^{-9} mbar. At this pressure the typical lifetime is tens of minutes to a few hours.

Ions in the trap are detected by their 397 nm and 393 nm fluorescence, either using a CCD or a photomultiplier tube (PMT), selectable via a rotatable mirror. A microscope objective mounted on a 3D micrometre stage above the trap provides x10 magnification. A periscope mirror guides the light from the objective through an iris and a bandpass filter centred at 397 nm to remove background scatter, then through an imaging lens pair. The CCD camera allows individual ions to be resolved to see their relative brightness, position, and motion (see Fig. 4.3. The PMT provides

high signal-background ratio (typically around 100:1) fluorescence counting, allowing spectroscopy or state detection to be carried out on the ion.

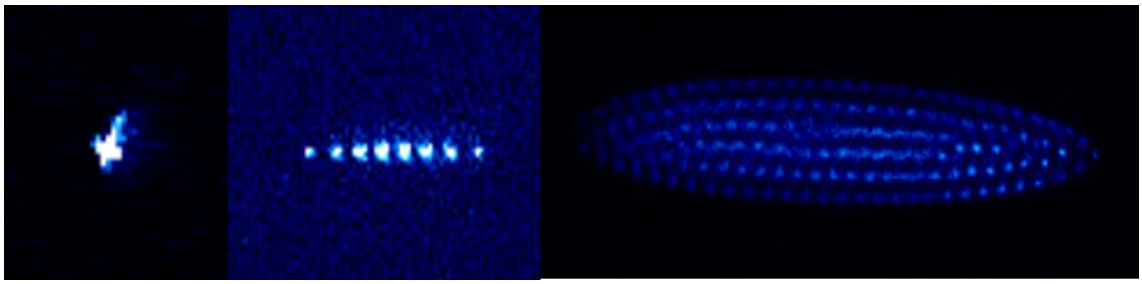

Figure 4.3: Images from the CCD camera showing a single ion (left), a string of eight ions (centre), and a Coulomb crystal with hundreds of ions, taken from [70]. The inter-ion spacing is on the order of 10 µm.

4.1.1 Trap electronics

The rf voltages used to create the trapping potential in the ion trap are supplied by a resonant circuit shown in Fig. 4.4. An rf frequency signal is supplied to a copper wire coil by a function generator via a 5 W amplifier. This coil is inductively coupled to a another coil, forming an rf transformer. The coil turn ratio is approximately 10:1. The resonator coil is centre-tapped to ground, so that it generates two voltages of equal amplitude and frequency with a relative π phase shift at each of its terminals. The signal from each terminal is split in two and passed to opposing pairs of the trap blade electrodes. The dominant capacitance in the resonator circuit is that between the electrodes, at approximately 25 pF. In series with each of the four arms is a variable capacitor to allow the amplitude on each electrode to be independently adjusted. By adjusting the capacitors in tandem, the pseudopotential minimum may be moved with micrometre precision without significant perturbation of the potential shape or increased micromotion [71]. A fixed resistor in parallel with each arm allows a dc offset voltage to be applied to the signal for micromotion compensation. It is important that the circuit be symmetric so as not to incur a relative phase between the electrode voltages, which would lead to excess micromotion. The dc voltage applied to the endcap electrodes is supplied by a single high-voltage supply.

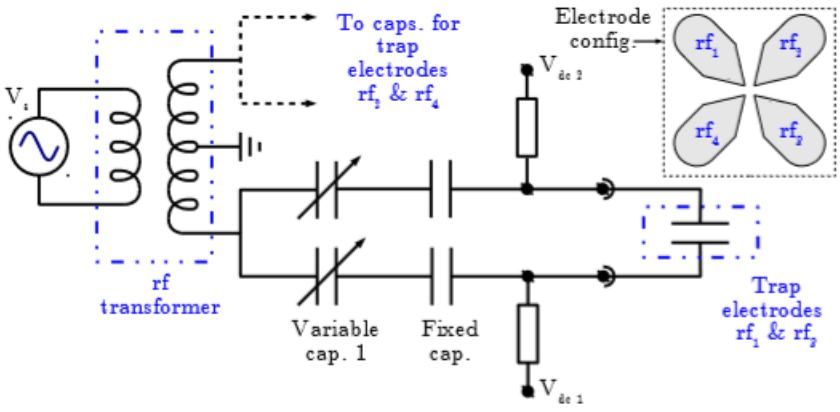

Figure 4.4: The resonant circuit used to supply the rf trapping voltage. Diagram from [68].

4.1.2 Trapping parameters

As described in Chapter 3, the trapping potential seen by the ion is determined by three physical parameters: the amplitude and frequency of the rf voltage, U_{rf} and Ω, and the dc voltage, U_{dc}. These lead to the radial and axial confinements, usually presented in terms e secular frequencies ω_r and ω_a. The earlier discussion of trap dynamics already mentioned a geometrical factor in the relationship between U_{dc} and ω_a. Similarly, deviations from the ideal hyperbolic trap geometry lead to a geometric factor for the radial secular frequency, and asymmetries in the trap lead to a splitting of the radial secular frequency into two frequencies ω_x and ω_y. While it is possible to obtain approximate values for the geometric factors from analysis and simulation of the trap geometry and voltages, to calculate the secular frequencies, they can also be directly measured. If the ion is excited at one its secular frequencies it will begin to oscillate along the corresponding axis with a large amplitude. This may be observed directly on the camera or indirectly as a drop in fluorescence. An additional rf field may be applied to the ion via the aluminium plate used to collimate the atomic beam from the oven. The ion's secular frequencies are determined by sweeping the frequency applied to the plate and observing the camera or PMT counts. Secular frequencies of $\omega_{\mathrm{ax}} = 0.90\,\mathrm{MHz}$ and $\omega_{\mathrm{x,y}} = 0.94\,\mathrm{MHz}$ and $0.95\,\mathrm{MHz}$ were measured using this method for the trap settings used in this thesis.

An ion will only remain trapped if its kinetic energy is less than the effective potential depth of the trap. The trap must therefore be sufficiently deep that it is able to capture an ion passing through the trap centre from the atomic oven. The depth in a direction i is given by

$$\phi_i = \frac{1}{2} m \omega_i^2 i_0^2, \tag{4.1.1}$$

where m is the ion mass, and i_0 is the distance between the trap centre and corresponding electrode. The trap depth is usually stated as being as the lowest depth in any direction. In the case of this trap, this is the radial direction, with a depth of $\phi_r = 2\,\mathrm{eV}$, equivalent to a temperature on the order of $10^6\,\mathrm{K}$. As Doppler cooling takes the ion to a few hundred microkelvin, an ion undergoing Doppler cooling is at no risk of falling out of the trap. Thus the limiting factor in ion lifetime is the background gas collision rate, which goes proportionally with the vacuum pressure.

4.1.3 Micromotion measurement and compensation

In Chapter 3 we introduced excess micromotion, a driven motion at the trap drive motion caused by stray dc fields or a phase mismatch in the rf trapping field. This motion reduces the ion-cavity coupling and can lead to Doppler or light shifts, and so it should be eliminated. The excess micromotion caused by stray dc fields can be reduced compensating for them with dc voltages applied to the rf electrodes. As the micromotion caused by the phase-mismatch is uncompensatable, care was taken to keep this mismatch small when assembling the trap electronics.

The micromotion in the radial direction is treated in the lab-frame horizontal and vertical directions for simplicity. The total compensation dc potential is also decomposed into its horizontal and vertical components:

$$H = (U_1 + U_2) - (U_3 + U_4), \quad V = (U_1 + U_4) - (U_2 + U_3), \tag{4.1.2}$$

where U_i is the voltage on the electrode i.

Eq. (3.2.3) shows that the position offset due to stray fields is inversely proportional to the square

of the amplitude of the radial potential. This provides a means of detecting stray fields: if the rf amplitude is changed, the ion's position will change if it is offset from the trap centre. We are able to observe a change in the ion's position in the horizontal direction on the CCD camera. With the rf potential being continuously swept over a range of values, the horizontal component of the compensation field is adjusted until the ion's position remains constant. At this point, the micromotion has been compensated in the horizontal direction. The precision of this method is limited by the resolution of the camera, and so is only viable for coarse micromotion compensation. Also, while the same effect occurs for the vertical direction, the motion of the ion in this direction cannot be seen on the camera. Therefore another method for precise detection of micromotion in two dimensions is required.

To this end, the technique described by Berkeland *et al* [72], known as the correlation technique, is used. The technique requires n cooling beams to compensate micromotion in n dimensions; in our case we require two, as we assume negligible micromotion in the axial direction. Micromotion along the direction of a laser beam will cause a modulation in the laser's frequency as seen by the ion due to the Doppler effect. This modulation will occur at the trap rf frequency. If the cross-correlation of the ion's fluorescence as detected by the PMT and the trap rf signal is taken, it will show a sinusoidal relationship. The visibility of this sine curve is related to the micromotion amplitude. It is also sensitive to the gradient of the absorption profile, so the laser frequency should be stabilised. The measurement will be most sensitive at $\Delta_L = \gamma$ as the gradient is largest at this point. When the micromotion in the direction of the laser is minimised, the visibility of this curve will be zero. For any given value of H, there is a corresponding optimal value of V, with a linear relationship. However, there will still be micromotion in the direction perpendicular to the laser, except for one pair of H and V. A second beam is therefore needed at some non-zero angle from the first. The 2D micromotion minimum occurs at the intersection of the $H - V$ lines for the two beams. Unlike the previous method, this method for micromotion detection is sensitive to the rf phase mismatch. While we are unable to compensate this source of micromotion, the measurement indicates that the residual micromotion is not significant enough to interfere with experiments.

The residual micromotion amplitude can be estimated using the optical cavity. Due to the modulation of the laser frequency in the ion's frame, Raman resonance occurs not just when the cavity detuning Δ_c is equal to the laser detuning Δ_L, but at $\Delta_c = \Delta_L \pm n\Omega_{\mathrm{rf}}$, where $n = 0, 1, 2, 3...$. This will appear as sidebands in a cavity Raman spectroscopy scan. The amplitude of these sidebands corresponds approximately to the micromotion amplitude x_{mm} perpendicular to the probe beam direction as

$$kx_{\mathrm{mm}} \approx 2R^{1/2}, \tag{4.1.3}$$

where k is the wavenumber of the probe beam and R is the ratio of the amplitudes of the sideband and carrier resonances [73]. Typically we have R on the order of 5 %, corresponding to a micromotion amplitude on the order of 10 nm. For the experiments in this thesis, the main impact of micromotion is a loss of single photon efficiency, and so $R \approx 5\,\%$ is tolerable. The deviation is negligible compared to the waist of the cavity mode and so does not greatly impact cavity coupling (see Section 4.3.3). In experiments that depend more strongly on the ion's temperature or on the coherence of the ion's motion, it can have a more significant impact.

4.1.4 Magnetic field

The strength and direction of the magnetic field seen by the ion affects how it interacts with the electromagnetic fields of the cavity and lasers. The strength of the field determines the level of

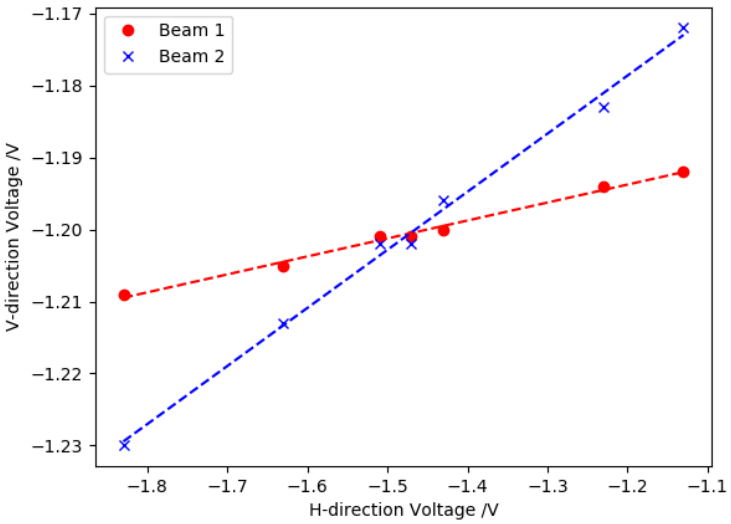

Figure 4.5: Effective micromotion compensation voltages applied in the horizontal (H) and vertical (V) directions, with lines of best fit, for two 397 nm beams. The optimal micromotion compensation voltages are found from the crossing point of both lines.

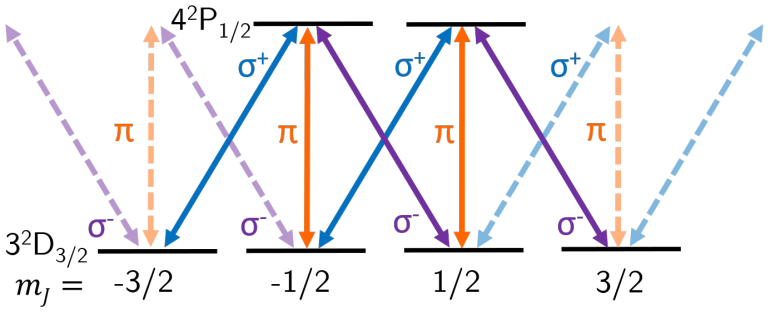

Figure 4.6: The transitions between the Zeeman sublevels of $D_{3/2}$ and $P_{1/2}$, with polarisations shown. Impossible transitions are greyed out.

splitting between the Zeeman sublevels of the ion's electronic states, and the direction of the field defines its quantisation axis. Therefore, the ambient field must be well understood so that can it can be nullified and a field of the desired strength and orientation may be applied.

Magnetic fields are applied to the trap in the x-, y-, and z-directions via pairs of Helmholtz coils. The coil pairs have separations approximately equal to their radii and are centred on the ion trap centre, such that they produce highly homogeneous fields at the position of the ion. The current-field strength gradient has been measured using a magnetometer and by observing the splitting in the cavity Raman emission spectrum. Current is supplied to the coils by a supply with a specified current noise of $< 1\%$ of the maximum current. This would result in fluctuations in the magnetic field on the order of a few milligauss, equivalent to a few kilohertz of Zeeman splitting, or a rotation in the field direction of $\approx 0.5°$. No magnetic shielding is used around the trap, so the ion is susceptible to fluctuations in the ambient field. The fluorescence of the ion may be used to measure the ambient magnetic field. The possible transitions between the Zeeman sublevels of $D_{3/2}$ and $P_{1/2}$ are shown in Fig. 4.6. For any polarisation of 866 nm laser light, there exists a superposition $|\psi\rangle = \sum_m \alpha_m |D_{3/2}, m\rangle$ for which the ion is dark. For example, in the case of π-polarised light (parallel to the B-field), the dark state is any superposition of $|D_{3/2}, m_J = \pm 3/2\rangle$. With the ion being pumped by a 397 nm laser to depopulate $S_{1/2}$, the ion's population is distributed

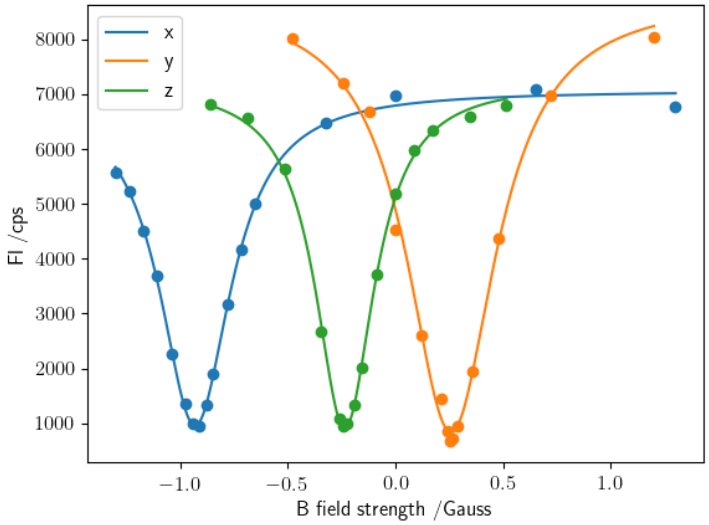

Figure 4.7: Ion fluorescence vs magnetic field strength in the x-, y-, and z-directions. In each case, the magnetic fields in the other two directions are fully compensated. Lorentzian curves are fitted to the data to extract minima, which occur at $B_{x,y,z}$=(−0.93, 0.26 and −0.24) G.

between the $D_{3/2}$ states until it reaches a dark state and ceases to fluoresce. If the magnetic field is rotated, the fluorescence of the ion increases as $\sigma^{\pm}$ transitions become coupled. This gives us a tool to find the direction of the magnetic field. First the 866 nm laser is polarised along a chosen direction, say x. The magnetic fields applied by the coils in the perpendicular directions are then scanned iteratively to find the fluorescence minimum. At this point, the magnetic field is aligned exactly along x, and so the ambient field has been nullified in the y and z directions. The laser polarisation is then rotated 90° and the applied magnetic field along the x direction is scanned again to find the fluorescence minimum. The magnetic field is now fully nullified. The results of this process are shown in Fig. 4.7.

4.2 Lasers

The laser light used in the experiment comes from external-cavity diode lasers (ECDLs) with linewidths on the order of a few hundred kilohertz. Feedback to stabilise the frequency of the lasers is applied to piezos to adjust the external cavity. There are two main sets of lasers: the photoionisation lasers and the main experimental lasers. All lasers are shared between multiple ion traps in the lab. The beams are divided by half-wave plates and beam splitter cubes into one or more arms for each experiment and coupled into optical fibres to be delivered to the various traps.

A two-stage photoionisation process, shown in Fig. 4.8, is used to produce the $^{40}Ca^{+}$ ions used in the experiment. The first step uses 423 nm laser light to excite the neutral calcium atoms. In the second step, 375 nm laser light excites an electron from the atoms into the continuum, leaving singly ionised calcium. As the 423 nm laser excites a specific transition, it is frequency stabilised to ≈ 50 MHz using a wavemeter. The wavelength of the 375 nm laser doesn't need to be so precise, as it it well below the ionisation threshold of 389 nm, and so is allowed to drift.

The main experimental lasers are at 397 nm, 850 nm, 854 nm, and 866 nm. The 397 nm beam

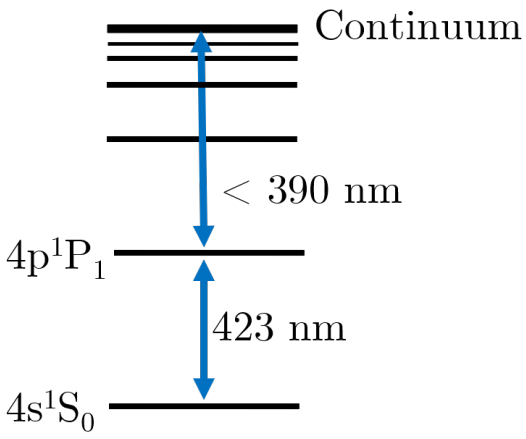

Figure 4.8: The two-stage photoionisation process for creating calcium ions from neutral atoms. The atom is first excited by the 423 nm before a 375 nm laser excites a single election into the continuum.

is produced by frequency doubling a 793 nm beam using a second harmonic generation crystal. The IR lasers all come directly from ECDLs. The laser beams all pass through acousto-optic modulators (AOM), where the first-order diffracted beam is sent to the trap. By adjusting an rf voltage applied to the AOM, the frequency and intensity of the beams may be adjusted. The 850 nm and 854 nm lasers are overlapped at a PBS and pass through the same AOM. A half-wave plate rotates the beams' polarisations before they are coupled into a polarisation-maintaining fibre (PMF). The two 866 nm beams and two 397 nm beams each go through a double-pass AOM set-up before being coupled into the PMFs, so that their frequency can be adjusted by the AOM without loss of coupling to the fibre [74]. The beams from the optical fibres at the trap are collimated and then focused down to a few tens of micrometers as they pass through the trap centre. This prevents them from scattering from the trap electrodes and causing background counts on the PMT or electrically charging the electrodes. Both 397 nm and 866 nm beams pass through a quarter- and half-wave plate pair to transform their polarisation from linear to the desired polarisation.

Each AOM is driven by a voltage-controlled oscillator (VCO). The VCOs generate rf signals centred at 200 MHz with a bandwidth of 50 MHz. They take two control voltages for modulating amplitude (AM) and frequency (FM). These are typically controlled from a PC via a digital-analogue converter (DAC). By driving the AM input with an arbitrary waveform generator (AWG), custom laser pulse shapes may be produced. The rf voltage passes from the VCO through an rf switch controlled by a TTL input which extinguishes the signal at 50 dB. The switches are controlled by an FPGA, allowing for the laser to be switched on and off in preprogrammed pulse sequences. The lasers have a fall time on the order of ten of nanoseconds.

4.2.1 Spectroscopy-stabilised frequency reference

The frequencies of all lasers used in the experiments and the length of the optical cavity are stabilised using a reference laser at 894 nm. This diode laser has its frequency stabilised by absorption spectroscopy and its linewidth narrowed by an optical cavity. A schematic of the locking scheme may be seen in Fig. 4.10, and the optical setup is shown in Fig. 4.11. The basic operating principle is thus: the laser frequency is locked to resonance with the optical cavity. The cavity length is then in turn locked to the error signal produced by saturation spectroscopy with the laser and a Cs reference cell. In this way, the long-term frequency stability of the atomic reference is transferred

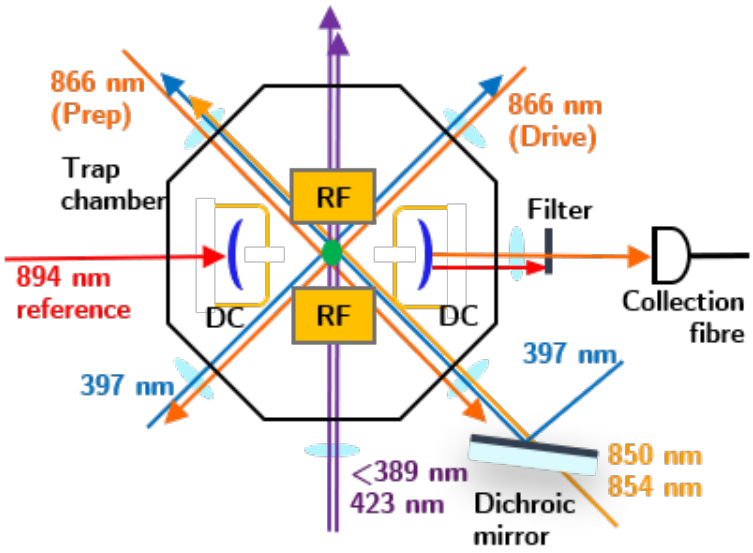

Figure 4.9: The directions of the laser beams passing through the trap centre from a top-down view.

to the laser via the cavity, while the cavity transfers its short-term stability to the laser. This setup was originally built by Nic Seymour-Smith and Peter Blythe [68] and later improved by Ezra Kassa and Hiroki Takahashi.

The laser output first passes through an optical isolator for stability, then a small amount of its power picked off by a wedge plate and sent to a wavemeter to monitor the frequency of the laser. The remaining light is then split by a series of half-wave plates and polarising beam splitters and sent to the spectroscopy circuit, the cavity circuit, and optical fibres leading to the experimental cavity and the stability transfer cavity (see Section 4.2.2). In the spectroscopy circuit, the light is first reflected at a PBS and then passes through a caesium vapour reference cell. There is enough power in the beam to saturate a transition in the atomic vapour. This pump beam then has its polarisation transformed to circular by a QWP and approximately half is retroreflected; the rest is dumped. The reflected part, the probe beam, passes back through the reference cell, is transmitted through the PBS, and is detected by a photodiode. The saturation caused by the pump beam leads to a Lamb dip in the absorption spectrum of the cell, which is used to create an error signal. In the cavity circuit, the light passes through a PBS and its polarisation is made circular by a QWP and coupled into a Fabry-Pérot cavity. A pair of APDs measure the transmitted and reflected signals. The transmitted signal is used to find resonance, while the reflected part generates the PDH error signal. The laser current is modulated at 10 MHz to generate the error signal. The laser frequency is locked simultaneously by two PID controllers: one for current and one for the grating angle, to provide feedback on different time scales. A width of 40 kHz has been measured for the lock, much narrower than the required width for the cavity and lasers used in the experiment.

4.2.2 Scanning-cavity transfer lock

Processes such as laser cooling and Raman transitions require the lasers used in the experiment to be frequency stabilised. For Doppler cooling, the laser frequency drift must be much smaller than the cooling transition linewidth. This may be fairly simply achieved by measuring the laser's wavelength on a commercial wavemeter an feeding back to compensate for laser drifts. using this method a standard deviation on the order of 1 MHz can be achieved. For cavity-assisted

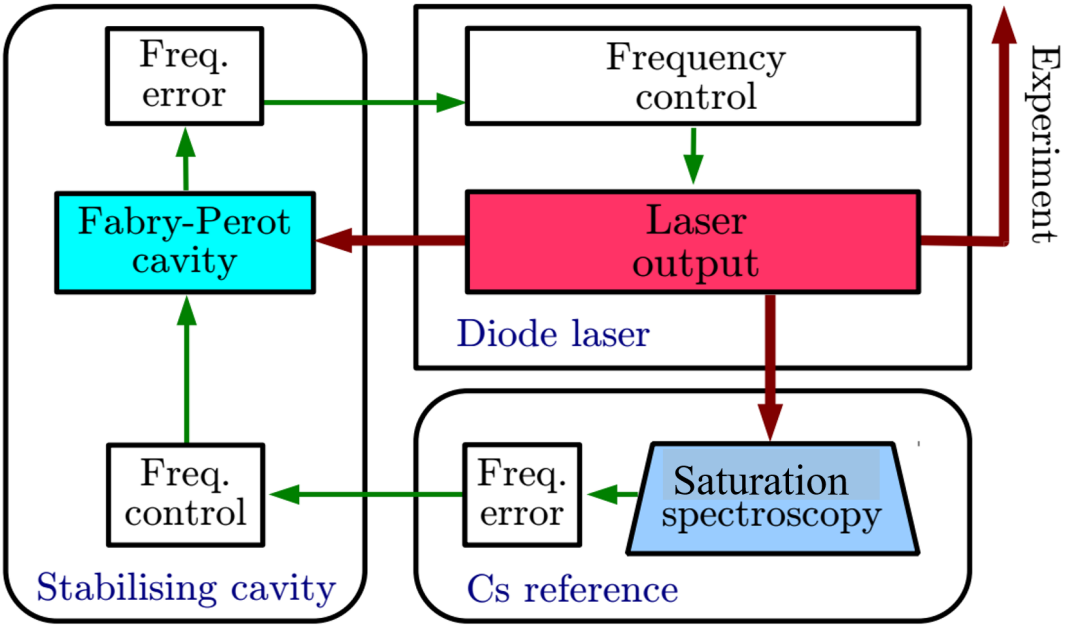

Figure 4.10: Schematic of the locking system for the reference laser from [70]. The laser frequency is locked to resonance with the optical cavity, which is then locked such that the laser remains resonant with a transition in the Cs reference cell.

Raman transitions, the requirements are more stringent. Meeting the Raman resonance condition requires the laser to be stable to within 2κ, around 500 MHz. To achieve this, the stability of the Cs reference laser is transferred to the experimental lasers by way of a scanning cavity stability transfer lock (SCL). The SCL optics and control electronics were originally designed and built by Peter Blythe and Nic Seymour-Smith [75]. It was then adapted to support two independent channels as part of the work for this thesis. The lock has been shown to have a stability of better than 10 kHz on timescales over 1 s. This method allows multiple lasers operating at different frequencies to be simultaneously locked to a single reference, making it a cost-effective approach that allows lasers to be locked with a high degree of stability even when no convenient transition for a spectroscopy-based technique is available.

The SCL transfers the frequency stability of a master laser to a number of slave lasers via an optical cavity. The master laser is coupled into the cavity, the mirrors of which are mounted on ring piezos. A triangle voltage from a function generator is applied to one of the mirror piezos. The scan amplitude is chosen such that the cavity length is scanned across slightly more than one free spectral range for the wavelength of the master laser, meaning the master laser is resonant with the cavity twice in a single scan. The transmission through the cavity is detected by a photodiode, the output of which goes to a peak detector, a combination of a discriminator and a differentiator. The peak detector generates a TTL pulse whenever the photodiode detects a peak. The TTL is sent to an FPGA which records the time of the peak. The time difference between the two peaks produced when the master laser is resonant with the cavity, τ_0, depends on the average length of the cavity. The FPGA produces a feedback voltage which is sent to one of the mirror piezos via a high voltage supply to keep τ_0 constant. Stability of the master laser frequency is thus transferred to the length of the cavity.

The synchronisation signal from from the function generator is also sent to the FPGA and recorded

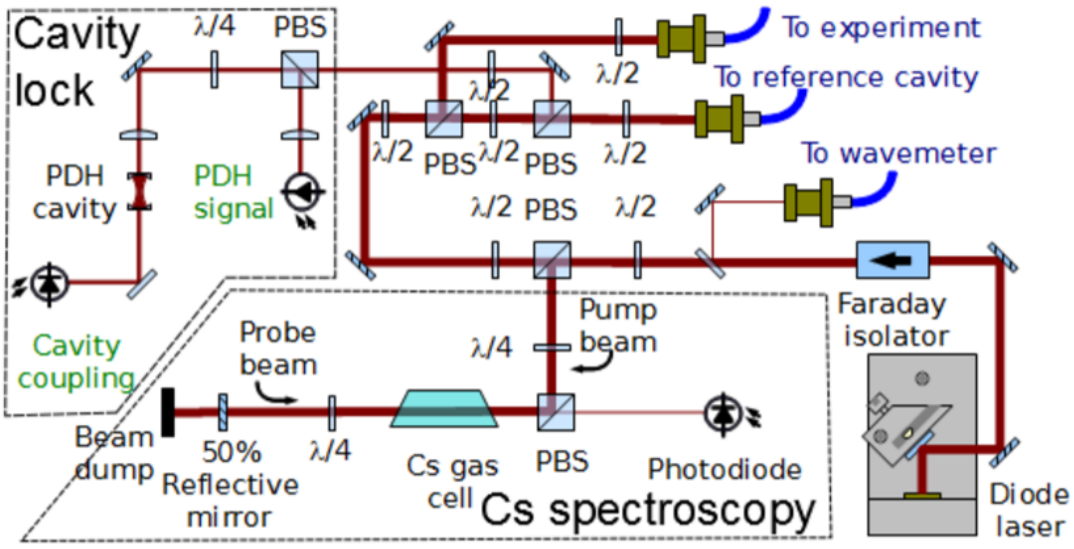

Figure 4.11: Optics and electronics for locking the frequency of the reference laser. PBS: polarising beam splitter. $\lambda/2$: half-wave plate. $\lambda/4$: quarter-wave plate. Diagram by [70].

as a reference for the beginning of the scan. If a slave laser is injected into the cavity, it will be resonant with the cavity at a time τ_1 after the sync signal. Its frequency can be stabilised by keeping τ_1 constant through a feedback voltage generated by the FPGA. This, however, isn't robust to drifts in the scan frequency, and so the ratio $r_1 = \tau_1/\tau_0$ is kept constant. The stability of the cavity, and therefore the master laser, is thereby transferred to the laser. A computer interface for the FPGA allows for manual identification of the master and slave lasers. It also allows the set point for feedback r_1 to be adjusted, allowing for accurate fine adjustment of the laser frequency. This can be done for multiple lasers, as long as they can be resolved by the peak detector and do not cross over one another when their frequency is adjusted, as this will cause the FPGA to feed back to the wrong laser.

In total, up to six lasers at a time are locked to the SCL. This leads to the issue that it is difficult to find a FSR in which all lasers are well enough separated in the cavity scan that they can have their frequency changed without overlapping. To get around this issue, the SCL was split into two channels, each supporting three slave lasers. Both channels share the same optical cavity and master laser, but have their own photodiodes and peak detectors, and are distinguished by polarisation. The lasers are delivered to the SCL system via optical fibres and overlapped in free space using 50:50 beam splitter cubes and dichroic mirrors. The transmission from the cavity first meets a polarising beam splitter, the output ports of which lead to two photodiodes. The slave lasers have their polarisations set so that they are either fully transmitted (channel 1) or reflected (channel 2). Each photodiode output goes to an independent peak detector, both of which send their TTLs to the same FPGA. This means that a laser on channel 1 can appear at the same time as channel 2 in the cavity scan without affecting the feedback, effectively doubling the number of lasers that can be used with the SCL at once.

4.2.3 Laser cooling

Optimally coupling the ion to the optical cavity and coherent manipulation of its electronic state requires a low temperature. This is achieved through Doppler cooling, in which a laser red-detuned

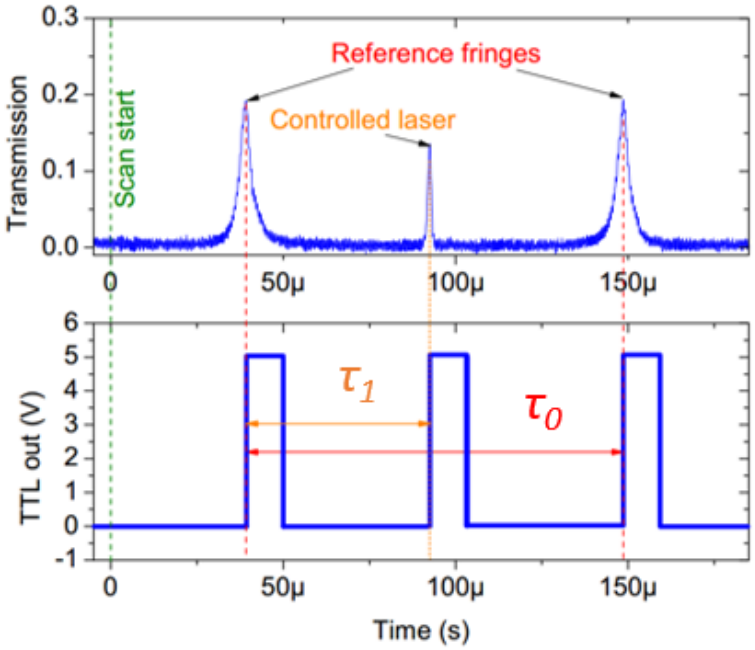

Figure 4.12: Top: Transmission through the scanning transfer cavity showing two peaks from the reference beam and one from a laser to be stabilised. Bottom: The TTL output from a peak detector. τ_0 is kept constant by feeding back to the cavity length, and τ_1/τ_0 is kept constant by feeding back to the laser frequency. Diagram from [68].

from resonance with the ion produces a damping force that reduces the thermal motion of the ion. The temperature achievable through Doppler cooling is limited by the linewidth of the transition used. This Doppler limit is given by

$$T_D = \frac{\hbar\Gamma}{2k_B}. \tag{4.2.1}$$

This limit is reached in the steady state when the laser is detuned by $\Gamma/2$, assuming a two-level system. The limit for the $S_{1/2} \leftrightarrow P_{1/2}$ transition is $T_D = 518\,\mu K$, though this assumes a two-level system. The practical limit will be affected by factors such as the branching fraction to the $D_{3/2}$ state, the Zeeman structure of the atom, and laser linewidth. There are several ways to reduce the ion's temperature past the Doppler limit, even to its motional ground state, such as sideband cooling [76] or EIT cooling [77]. For the experiments carried out in this doctoral work, however, Doppler cooling is sufficient. In future work discussed in Chapter 7, such as ion-photon or ion-ion entanglement, ground-state cooling techniques may become necessary to achieve high fidelities.

4.3 The Experimental Cavity

The experimental optical cavity is a Fabry-Pérot etalon designed to be resonant with the 866 nm $D_{3/2} \leftrightarrow P_{1/2}$ transition in $^{40}Ca^+$. The axis of the cavity is co-linear with the trap axis, such that, in multi-ion experiments, all of the ions can couple to the cavity field. The cavity is formed of two concave mirrors of radius of curvature $R = 25\,mm$ separated by a distance $L = 5.75\,mm$. Each mirror is a 1 mm diameter highly reflective coating applied to a substrate. The substrates are 10 mm long, 3 mm diameter fused silica rods, tapered at one end. The substrate sits inside a collet, which is glued at the back surface to a piezo-electric crystal (lead zirconate titanate, PZT) which in turn is glued to the collet mount. A PEEK screw fastens the substrate in place. The

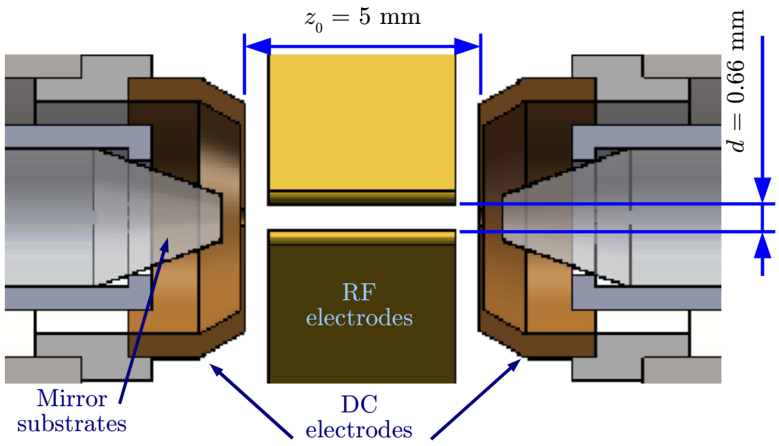

Figure 4.13: The cavity inside the trap structure.

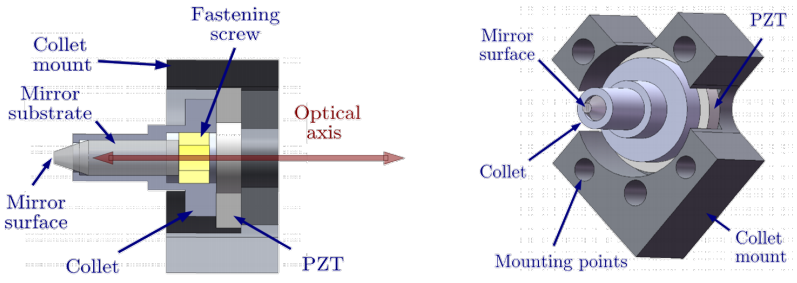

Figure 4.14: Cavity substrates and collet mounts. Left: Side-view cross-section by Nic Seymour-Smith. Right: 3D CAD design of the collet mounting structure by Matthias Keller, taken from [70].

PZT allows each mirror to be translated independently up to 2 µm along the cavity axis, allowing the length of the cavity or the position of the cavity with respect to the ion to be changed. This range of movement gives access to approximately 6 free spectral ranges (FSR).

The cavity output mode is collimated by a lens outside of the trap. Two band pass filters with a cut-off between 894 nm and 866 nm filter out the cavity locking light to within the noise of the detector dark counts. Each has a transmittance of 90% at 866 nm. Depending on the requirement of the experiment, quarter- and half-wave plates and a polarising beam splitter cube may be used to rotate and filter the circularly polarised light emitted from the cavity. The cavity output is coupled into a PMF with an efficiency of 66%. The cavity emission is detected by a superconducting nanowire single-photon detector (SSPD). Two channels at each of 866 nm and 1530 nm are available for correlation measurements. The 866 nm detectors have a specified quantum efficiency of $> 80\%$ and dark counts of 1 cps. The 1530 nm detectors have a specified quantum efficiency of $> 90\%$ and dark counts of 4 cps.

4.3.1 Cavity parameters

The parameters of interest for the optical cavity in CQED are the ion-cavity coupling strength g and the cavity decay rate κ. As discussed in Chapter 2, the cavity coupling strength is given by

$$g = \sqrt{\frac{d_{PD}^2 \omega_c}{2\hbar\varepsilon_0 V}}. \tag{4.3.1}$$

where V is the mode volume and d_{PD} is the transition dipole moment between the states $P_{1/2}$ and $D_{3/2}$. The ion couples to the fundamental Gaussian mode of the cavity, the volume of which is

$$V = \frac{\pi L w_0^2}{2}, \tag{4.3.2}$$

where w_0 is the cavity waist [78]. The waist is given by

$$w_0 = \sqrt{\frac{\lambda}{2\pi}(L(2R-L))^{1/2}}. \tag{4.3.3}$$

For our cavity, this gives $w_0 = 47\,\mu\mathrm{m}$. From this we calculate $g_0 = 2\pi \times 0.795\,\mathrm{MHz}$.

The length of the cavity is calculated from a measurement of the free spectral range (FSR) of the cavity, which is the inverse of the round-trip time in the cavity;

$$\mathrm{FSR} = \frac{c}{2L}. \tag{4.3.4}$$

The procedure for measuring the free spectral range is as follows:

- Lock the cavity length using a reference beam
- Shine laser light into the cavity at a known wavelength (e.g. using a wavemeter) and tune it to resonance with a particular mode by observing the cavity transmission
- Tune the laser wavelength up or down until it reaches resonance with the next longitudinal mode

The difference in wavelengths is equal to the FSR. We measured an FSR of 26.04(4) GHz, which gives a cavity length of 5.75(1) mm.

The decay rate of the cavity is related to the finesse of the cavity, $\mathcal{F}$. The finesse is a measure of losses in the cavity; if, after one round-trip in cavity, some fraction ρ of the cavity population is lost, the finesse is given by

$$\mathcal{F} = \frac{2\pi}{\rho}. \tag{4.3.5}$$

The cavity mirrors have specified transmissivities of 100 ppm and 5 ppm, chosen to give a high degree of directionality to the cavity emission, and giving a finesse of $\approx 60,000$. The finesse is also defined as the ratio of the FSR and spectral linewidth of the cavity, $\Delta\nu$. We can use the relation $2\kappa = 2\pi \times \Delta\nu$ to find the expected decay rate of the cavity:

$$2\kappa = \frac{\mathrm{FSR}}{\mathcal{F}} = 2\pi \times 0.434\,\mathrm{MHz}. \tag{4.3.6}$$

The decay rate may also be directly measured using a cavity ringdown measurement. By coupling laser light into the cavity for long enough for the system to reach a steady state, and then turning off the laser, the cavity lifetime can be determined by observing the decay in cavity emission. An exponential fit to the cavity emission decay data in Fig. 4.15 gives a lifetime of 296(8) ns, leading to a decay rate $2\kappa = 0.537(7)\,\mathrm{MHz}$. The higher κ than expected from Eq. (4.3.6) implies that the mirror transmissivities are higher than specified, or that there are non-negligible mirror losses, or that the cavity length is fluctuating. The losses can be due to scattering from imperfections in the mirror surfaces or absorption by the mirror. Such losses could be caused by contamination on the mirror surfaces, possibly due to the atomic oven, or from when the cavity was outside of vacuum. An initial test of the mirrors before they were installed in the system showed results

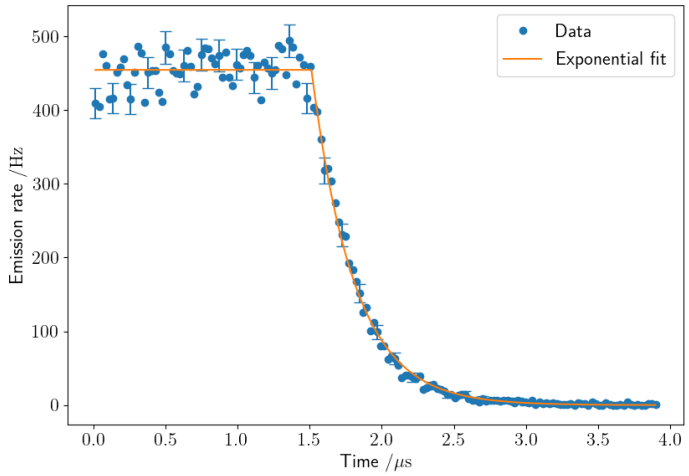

Figure 4.15: Cavity ringdown measurement, showing cavity emission over time. Error bars are from counting statistics, shown only on every fifth point for clarity. The data were fitted to an exponential decay.

consistent with the specifications. Assuming the specified transmissivities are correct, the losses in the mirrors are 25 ppm. With 5 ppm leaving through the input mirror, and 25 ppm losses, $\approx 77\%$ of the cavity population will leave through the 100 ppm output mirror, which sets the upper limit of efficiency of single-photon generation using the cavity.

4.3.2 Cavity locking

For efficient ion-cavity interactions, it is important to be able to stabilise the length of the cavity, both on long time scales to maintain resonance, and short time scales to keep the effective linewidth of the cavity narrow. This is achieved by locking the cavity to the Cs spectroscopy reference laser used to lock the laser. It is also necessary to be able to finely adjust the cavity length to change its detuning from resonance with the ion. As the reference laser frequency is fixed by the Cs atomic transition, the cavity is locked to tunable sidebands applied to the laser light. The fundamental mode of the reference laser in the cavity cannot be used, as as the high intensity at the position of the ion would cause significant Stark shifts. Instead, the cavity is locked to the TEM_{70} mode, as this mode has a low intensity at the centre. In a particular free spectral range of the cavity, this mode falls 272 MHz from resonance with the $D_{3/2} \leftrightarrow P_{1/2}$ transition.

The locking optics and electronics are shown in Fig. 4.16. The Pound-Drever-Hall (PDH) locking technique is employed, using the reflection from the 5 ppm mirror and feeding back to the piezo of the 100 ppm mirror. The reference laser is phase-modulated by an electro-optic modulator driven by a 10 MHz function generator to create the PDH error signal and a tunable rf generator with a range of 500 Hz-500 MHz to produce the sidebands. The reference light passes through a half-wave plate (HWP) and then through a polarising beam splitter cube (PBS). The HWP rotates the laser light to horizontal for maximum transmission through the cube. The polarisation of the light is then transformed to circular by a quarter-wave plate (QWP). The beam reflected from the cavity is then rotated to vertical by the QWP and reflected from the PBS and coupled into an avalanche photodiode detector (APD). The output of the APD is mixed with a 10 MHz rf signal producing a a PDH error signal. The error signal is fed into a proportional-integral-differential (PID) controller, which feeds back to the cavity piezo via a high-voltage supply, keeping the cavity length resonant

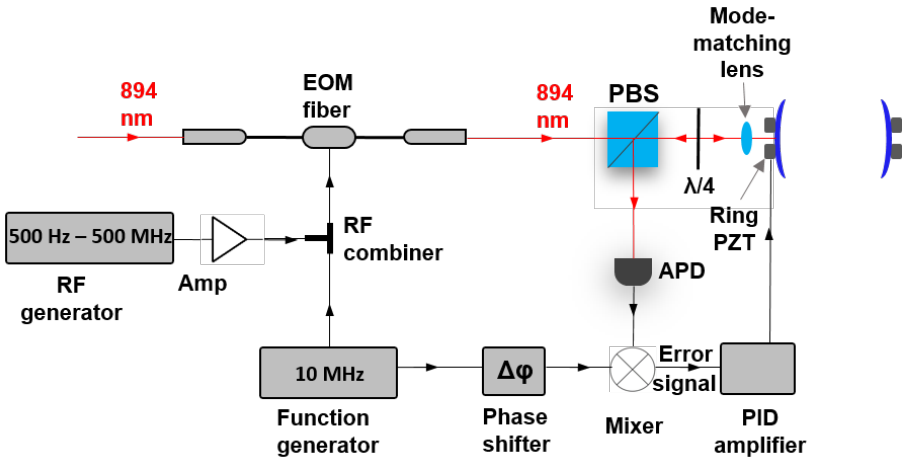

Figure 4.16: Optics and electronics for locking the length of the experimental cavity. Diagram from [70].

with one of the sidebands of the reference laser. Typically, only the proportional and integral parts of the PID circuit are used.

4.3.3 Positioning the ion in the cavity

As discussed in Chapter 2, the ion-cavity coupling depends on the amplitude of the cavity field at the ion's position. As we want to maximise the ion-cavity coupling, the ion should be positioned at a maxima of the field. The spatial profile of the fundamental mode of the cavity has the form:

$$u(z) = \frac{w_0}{w(z)} \exp\left(\frac{-x^2}{w(z)^2}\right) \exp\left(\frac{-y^2}{w(z)^2}\right) \cos\left(kz + \frac{kr^2}{2R(z)} + \psi(z)\right), \tag{4.3.7}$$

where k is the wavenumber of the cavity field, w is the mode radius, $w_0 = w(z = 0)$ is the mode waist, $R(z)$ is the radius of curvature of the beam, and $\psi(z)$ is the Gouy phase. Near the centre of the cavity, the term including the radius of curvature can be neglected. The Gouy phase can also be neglected here.

The cavity coupling can be measured using the cavity emission rate. With the cavity at Raman resonance with the 397 nm beam and the $D_{3/2}$ state being continuously repumped, the rate of cavity emission R_{em} is proportional to the intensity of the cavity field $I(x, y, z)$ at the ion's position, assuming efficient repumping and that the $S_{1/2} \leftrightarrow P_{1/2}$ transition isn't saturated. The ion is positioned radially by adjusting the relative amplitudes on the rf electrodes, and axially by translating the cavity mirrors using the piezos. These are adjusted until the emission rate is maximised, at which point we have optimised the cavity coupling.

Until now we have assumed the ion is a point particle that sits at a specific point in the cavity field. However, as the ion has some non-zero temperature, its thermal motion causes it to probe a region of the field over time. On time scales longer than the secular frequency of the ion, the ion experiences an averaged effective coupling to the field dependant on its spatial distribution. This gives us a means to measure the temperature of the ion. At typical ion temperatures the deviation of the ion from the centre is small enough relative to the mode diameter that the radial motion can be neglected, so we only need to consider the sinusoidal axial profile. The classical spatial

probability density $|\Psi|^2$ of the ion at temperature T is a Gaussian distribution of width with

$$\Delta z^2 \approx \frac{2k_B T}{m\omega_{\text{sec}}^2}, \tag{4.3.8}$$

where k_B is the Boltzmann constant and ω_{sec} is the secular frequency in the relevant direction. The average cavity emission rate R is proportional to the convolution of the intensity of the cavity field and the spatial probability density function of the ion:

$$R_{\text{em}}(z) \propto \int_{-\infty}^{\infty} |\Psi(z')|^2 I(z - z')\, dz' \tag{4.3.9}$$

$$\propto \left(1 + e^{-k^2 \Delta z^2} \cos(2kz)\right). \tag{4.3.10}$$

A derivation of the solution to the integral may be found in [70]. It is clear that as the ion is translated along the standing wave of the cavity the emission rate changes sinusoidally, with minima and maxima determined by the width of the ion's position distribution. The visibility of the emission rate is related to the spread of the ion's spatial profile by

$$V = \frac{R_{\text{max}} - R_{\text{min}}}{R_{\text{max}} + R_{\text{min}}} = e^{-k^2 \Delta z^2}, \tag{4.3.11}$$

which can be used with Eq. (4.3.8) to determine the ion's temperature. When Doppler cooling, visibilities of around 60% are observed, corresponding to a spread of $\Delta z = 100\,\text{nm}$ and a temperature of 750 µK, or 1.4 times the Doppler temperature limit. The achievable temperature is likely limited by residual micromotion. We may also use this method to calculate the time-averaged ion-cavity coupling:

$$g_{\text{eff}} = \frac{1}{\sqrt{2\pi}\Delta z} \int_{-\infty}^{\infty} e^{-\frac{z^2}{2\Delta z^2}} g_0 \cos(kz) dz. \tag{4.3.12}$$

A spread of $\Delta z = 100\,\text{nm}$ gives an effective coupling of $g_{\text{eff}} = 2\pi \times 0.62\,\text{MHz} = 0.77 g_0$.

Chapter 5

Frequency Conversion of Single Photons

Large-scale quantum networks will require optical fibre connections over tens or hundreds of kilometres. This poses a challenge for trapped-ion-based quantum networks, as the emission from ions tends to be in the visible and near-infrared (NIR) regions of the electromagnetic spectrum, where attenuation in optical fibres tends to be prohibitively high. For the system presented here with 866 nm emission, the attenuation is $\approx 3\,\mathrm{dB\,km^{-1}}$. One way to deal with this issue is the use of quantum repeaters [79], which would be placed along quantum channels and facilitate the entanglement between distant network nodes. However, no such quantum repeaters have thus far been demonstrated, and it is unclear whether enough repeaters could realistically be built and maintained to enable communication using NIR photons in optical fibre. An alternative approach is to convert from the lossy ion wavelength to a less lossy one, such as the telecom wavelength bands used in commercial optical fibre telecommunications. This allows not only far longer transmission distance, but also opens the option of using existing telecom fibre channels as the backbone of the quantum network. The least lossy and most common telecom wavelength band is the C-band at 1530 nm to 1565 nm, which exhibits losses in optical fibres of $\approx 0.2\,\mathrm{dB\,km^{-1}}$. Converting to a telecom frequency has the added benefit of allowing disparate quantum systems, which may emit and absorb light at mutually incompatible wavelengths, to interface with each other by interconverting via a single shared wavelength.

Quantum frequency conversion (QFC) is the process of converting light from one frequency to another while preserving its quantum state[80]. QFC has been demonstrated in a wide variety of systems, including quantum dots [81, 82], atomic ensembles [83–86]. When the work presented in this chapter was carried, out, QFC had not yet been demonstrated with photons from a trapped ion system. Since then, several demonstrations have been performed [87–89], showing the interest in this avenue of research into quantum networking. The quantum state of photons [90–92] and entanglement [88, 89] are preserved with near-unity fidelity through the frequency conversion process, making it suitable for use in quantum networks. The entanglement of two quantum memories separated by dozens of kilometres has been demonstrated [93].

In the experiment presented in this chapter, 866 nm light produced by cavity-assisted Raman transitions was converted to 1530 nm and transmitted through 10 km of optical fibre, at the time the furthest transmission of photons from a trapped ion source. The second-order coherence function was measured before and after conversion and long-distance transmission to demonstrate

that the ion-QFC systems acts as a pure source of single photons. The frequency conversion setup was built by the group of Nobuyuki Imoto from the Graduate School of Engineering Science, Osaka University. This was published as a letter titled "Long-Distance Single Photon Transmission from a Trapped Ion via Quantum Frequency Conversion" [87].

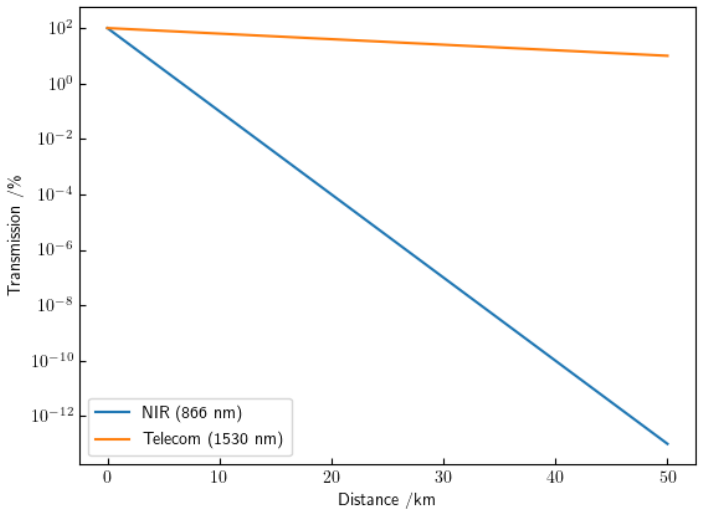

Figure 5.1: Percentage of signal transmitted through an optical fibre at 866 nm and 1530 nm.

5.1 Frequency Conversion

Frequency conversion is performed by taking advantage of nonlinear effects in various media. We are interested in particular in difference frequency generation (DFG), a second-order nonlinear effect in which a field is generated with a frequency equal to the difference of two input fields (see Fig. 5.2). Here I will present a classical derivation of this effect, and show how the state of converted photons is preserved in the quantum mechanical description. A full quantum derivation is beyond the scope of this thesis, but the quantum description follows easily from the classical description [94, 95].

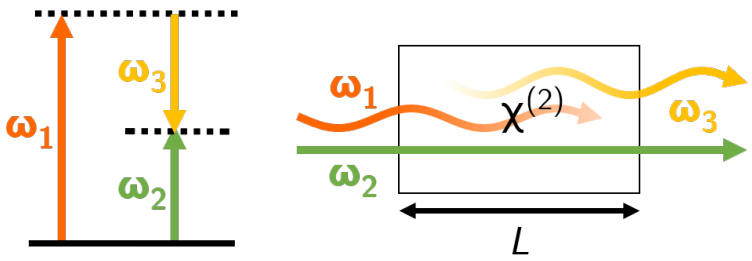

Figure 5.2: Difference frequency generation. A weak input field and strong pump beam of angular frequencies ω_1 and ω_2 mix in a waveguide with a significant second-order susceptibility $\chi^{(2)}$ to produce a field of frequency $\omega_3 = \omega_1 - \omega_2$.

5.1.1 Difference frequency generation

We can describe nonlinear effects in a medium by looking at its polarisation density $\boldsymbol{P}$, which depends on the its electric susceptibilities $\chi^{(i)}$ and the electric field $\boldsymbol{E}$ in the medium:

$$\boldsymbol{P} = \sum_{i=1}^{\infty} \boldsymbol{P}^{(i)} \tag{5.1.1}$$

$$= \sum_{i=1}^{\infty} \varepsilon_0 \chi^{(i)} \boldsymbol{E}^i. \tag{5.1.2}$$

In linear optics, the higher-order χ terms are vanishingly small, and the polarisation density is proportional to the electric field. The presence of a non-negligible $\chi^{(i)}$ term is referred to as ith-order nonlinearity. It can be shown from Maxwell's equations that this nonlinearity in a medium gives rise to the driven wave equation:

$$\nabla^2 \boldsymbol{E} - \frac{n^2}{c^2} \frac{\partial^2 \boldsymbol{E}}{\partial t^2} = \frac{1}{\varepsilon c^2} = \frac{n^2}{c^2} \frac{\partial^2 \boldsymbol{P}_{NL}}{\partial t^2}, \tag{5.1.3}$$

where n is the refractive index and $\boldsymbol{P}_{NL} = \sum_{i=2}^{\infty} \boldsymbol{P}^{(i)}$ is the nonlinear part of the polarisation density. Consider two electric fields with angular frequencies ω_1 and ω_2 propagating in a waveguide along the z-direction. We may write the total electric field in the medium as

$$E(t) = E_1 e^{-i\omega_1 t} + E_2 e^{-i\omega_2 t} + \text{c.c.}, \tag{5.1.4}$$

where c.c. denotes the complex conjugate. We have dropped the vector notation as the waveguide used only supports a single polarisation and propagation along a single direction. The spatial dependence of the field is given by $E_j(x, y, z) = u_j(x, y) A_j e^{ik_j z}$, where $k_j = n_j \omega_j / c$ is the wavenumber. The second-order polarisation density in the medium is

$$P^{(2)}(t) = \varepsilon_0 \chi^{(2)} [E_1^2 e^{-i2\omega_1 t} + E_2^2 e^{-i2\omega_2 t} \tag{5.1.5}$$

$$+ 2E_1 E_2 e^{-i(\omega_1+\omega_2)t} + 2E_1 E_2^* e^{-i(\omega_1-\omega_2)t} + \text{c.c.}] \tag{5.1.6}$$

$$+ 2\varepsilon \chi^{(2)} [|E_1|^2 + |E_2|^2]. \tag{5.1.7}$$

We can express this in terms of its different frequency components:

$$\begin{aligned} P(2\omega_1) &= \varepsilon_0 \chi^{(2)} E_1^2 && \text{(SHG)} \\ P(2\omega_2) &= \varepsilon_0 \chi^{(2)} E_2^2 && \text{(SHG)} \\ P(\omega_1 + \omega_2) &= \varepsilon_0 \chi^{(2)} E_1 E_2 && \text{(SFG)} \\ P(\omega_1 - \omega_2) &= \varepsilon_0 \chi^{(2)} E_1 E_2^* && \text{(DFG)} \\ P(0) &= \varepsilon_0 \chi^{(2)} [|E_1|^2 + |E_2|^2], && \text{(OR)} \end{aligned} \tag{5.1.8}$$

with $P^{(2)} = \sum_n P(\omega_n) e^{-i\omega_n t}$. The first two terms correspond to the doubling of the frequency of each field, known as second-harmonic generation (SHG). The third (fourth) term corresponds to three-wave mixing between the two input fields and a field at the sum (difference) of their frequencies. These are sum and difference frequency generation (SFG and DFG). The dc component corresponds to optical rectification (OR). As Eq. (5.1.3) hold for all frequency terms, the DFG term implies a field

$$E(z, t) = A_3 e^{i(k_3 z - \omega_3 t)} + c.c \tag{5.1.9}$$

with $\omega_3 = \omega_1 - \omega_2$. The nonlinearity of the medium gives A_3 a slowly-varying dependence on z. Solving the wave equation for each field gives us the coupled equations

$$\frac{\mathrm{d}A_1}{\mathrm{d}z} = -i\kappa A_2^* A_3 e^{-i\Delta k z} \tag{5.1.10}$$

$$\frac{\mathrm{d}A_2}{\mathrm{d}z} = -i\kappa A_1^* A_3 e^{-i\Delta k z} \tag{5.1.11}$$

$$\frac{\mathrm{d}A_3}{\mathrm{d}z} = -i\kappa A_1 A_2 e^{-i\Delta k z}, \tag{5.1.12}$$

where

$$\kappa = \varepsilon\chi^{(2)} \left(\frac{2\hbar\omega_1\omega_2\omega_3 Z_0^3}{n_1 n_2 n_3} \right)^{1/2} \cdot \Theta \tag{5.1.13}$$

is the coupling coefficient with mode overlap

$$\Theta = \iint \chi^{(2)} u_1(x,y) u_2(x,y) u_3(x,y) \mathrm{dxdy} \tag{5.1.14}$$

and $Z_0 = \sqrt{\mu_0/\varepsilon_0}$. Δk is the phase mismatch given by $\Delta k = k_1 - k_2 - k_3$. Let us consider the case that A_2 is a strong pump beam that is undepleted by the nonlinear mixing; that is, A_2 remains constant ($A_2(z) = A_2(0) = A_p$), while A_1 is a weak input beam. Assuming perfect phase matching ($\Delta k = 0$) and initial conditions $A_1(0) = A_0$, $A_3(0) = 0$, the solutions to the coupled equations are

$$A_1(z) = A_0 \cos(\kappa A_p z) \tag{5.1.15}$$

$$A_3(z) = A_0 \sin(\kappa A_p z). \tag{5.1.16}$$

In a waveguide of length L with pump power $P_p = |\dot{A}_p|^2$, the conversion efficiency η is defined as the ratio of the intensities of the input $|A_0|^2$ and output $|A_3(L)|^2$:

$$\eta = \frac{|\mathrm{A}_3(L)|^2}{|A_0|^2} = \eta_0 \sin^2\left(\sqrt{\kappa^2 P_p} L \right), \tag{5.1.17}$$

where η_0 is the maximum efficiency. Maximum conversion is achieved when $\sqrt{\kappa^2 P_p} L = \pi/2$. The function is sinusoidal as the converted wave mixes with the pump and back-converts to the input frequency. Once the waveguide is manufactured, the pump power is the only freely tunable parameter, so κ and L must be chosen to allow this condition to be met at a reasonable pump power. Once the waveguide is in place, κ and η_0 can be determined empirically by measuring the conversion efficiency versus pump power. Fig. 5.3 shows the efficiency versus pump power curve obtained for the waveguide used in this experiment. Values of $\eta_0 = 0.56$ and $\kappa^2 L^2 = 9.3\,\mathrm{W}^{-1}$ were obtained, giving an optimal pump power of $0.265\,\mathrm{W}$. η_0 is limited both by controllable factors such as the coupling of the input beam into the waveguide, and by fixed factors such the quality of the machining of the waveguide structure. Thus there is a hard limit to conversion efficiency for a given waveguide.

Quasi-Phase-Matching

In the above analysis we assumed zero phase mismatch; that is,

$$\begin{aligned} \Delta k &= k_1 - k_2 - k_3 \\ &= \frac{n_1\omega_1}{c} - \frac{n_2\omega_2}{c} - \frac{n_3\omega_3}{c} = 0 \end{aligned} \tag{5.1.18}$$

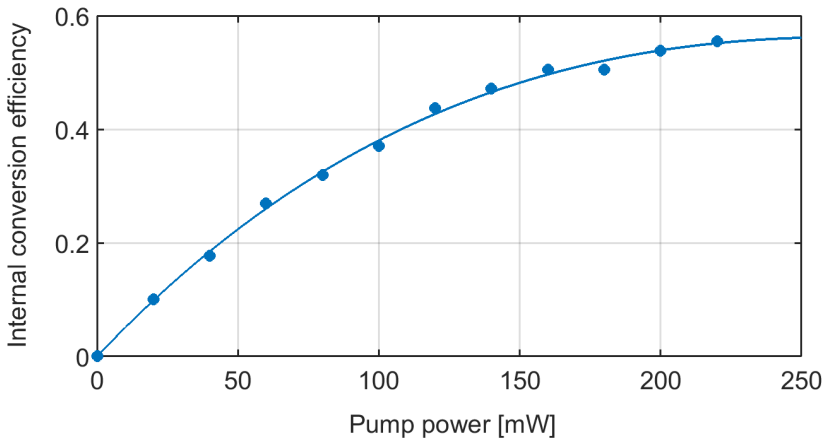

Figure 5.3: The internal conversion efficiency from 866 nm to 1530 nm measured for the PPLN waveguide used in the experiment. A solid curve is obtained by fitting the experimental data with a function $\eta_0 \sin^2(\sqrt{\kappa^2 P_p} L)$, where P_p is the power of the pump light at 1995 nm. The fitting parameters were calculated to be $\eta_0 = 0.56$ and $\kappa^2 L^2 = 9.3\,\mathrm{W}^{-1}$.

In practice this won't be the case, as materials tend to exhibit increasing refractive index with frequency (normal dispersion). The resulting phase mismatch causes the converted field to interfere with itself and oscillate in amplitude along the waveguide with a period governed by the coherence length $L_c = \pi/\Delta k$. To combat this, the material may be periodically poled, meaning the orientation of the crystal axis is inverted at intervals of $\Lambda = 2L_c$, such that in regions where the amplitude would decrease, it instead increases. This is called quasi-phase-matching (QPM) and is demonstrated in Fig. 5.4. As can be seen in the figure, by using periodic poling the amplitude increases monotonically, albeit at a slower rate than the perfect phase matching case, and so high conversion efficiencies are still achievable.

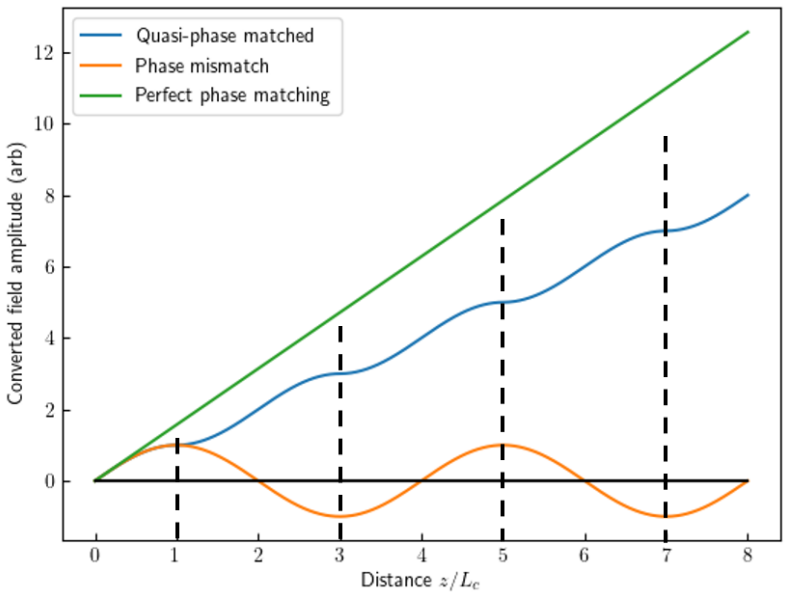

Figure 5.4: Amplitude of the converted field versus travel distance through the medium for perfect phase-matching, QPM, and no phase matching. Dashed lines show the points where the crystal axis is flipped.

Quantum frequency conversion

For DFG to be useful in quantum networking it must preserve the quantum state of the input field when converting to the target field. To show this, we must move a quantum mechanical description of the process. We define the photon creation and annihilation operators for each field $\hat{a}_i^\dagger$ and $\hat{a}_i$ that act on the states $|\psi\rangle_i$ with $i = 1, 2, 3$. The interaction Hamiltonian for the fields in the medium is

$$\hat{H}_I = i\hbar\kappa(\hat{a}_1\hat{a}_2^\dagger\hat{a}_3^\dagger - \hat{a}_3\hat{a}_2\hat{a}_1^\dagger), \tag{5.1.19}$$

where κ is a coupling constant analogous to the one defined in Eq. (5.1.13). We see that the annihilation of a photon in mode des_1 leads to the creation of a photon in each of $\hat{a}_2$ and $\hat{a}_3$ and vice versa, aligning with the DFG relation $\omega_3 = \omega_1 - \omega_2$. If we again assume a strong pump, then the addition or subtraction of a single photon negligibly affects the field. We may treat therefore this field classically, and write the Hamiltonian as

$$\hat{H}_I = i\hbar\kappa A_p(\hat{a}_1\hat{a}_3^\dagger - \hat{a}_3\hat{a}_1^\dagger), \tag{5.1.20}$$

Using the Heisenberg equation we find the coupled rate equations for the fields:

$$\frac{\mathrm{d}\hat{a}_1}{\mathrm{d}t} = \kappa A_p\hat{a}_3 \tag{5.1.21}$$

$$\frac{\mathrm{d}\hat{a}_3}{\mathrm{d}t} = -\kappa A_p\hat{a}_1. \tag{5.1.22}$$

The solution to the rate equations is

$$\hat{a}_1(t) = \hat{a}_1(0)\cos(\kappa A_p t) - \hat{a}_3(0)\sin(\kappa A_p t) \tag{5.1.23}$$

$$\hat{a}_3(t) = \hat{a}_3(0)\cos(\kappa A_p t) + \hat{a}_1(0)\sin(\kappa A_p t). \tag{5.1.24}$$

With the initial conditions that there is a single excitation in mode $\hat{a}_1$ and no excitation in mode $\hat{a}_3$; that is, $\hat{n}_1(0) = 1$ and $\hat{n}_3(0) = 0$, where $\hat{n}_i(t) = \hat{a}_i^\dagger(t)\hat{a}_i(t)$, these reduce to the same results as in the classical case, but as a function of time rather than distance.

Consider the expectation values of some observable for the two modes $\langle\hat{f}_1\rangle = \langle\Psi|\hat{f}_1(\hat{a}_1)|\Psi\rangle$ and $\langle\hat{f}_3\rangle = \langle\Psi|\hat{f}_3(\hat{a}_3)|\Psi\rangle$ for a system state $|\Psi\rangle = |\psi_1, \psi_3\rangle$ At $t = 0$, these are

$$\langle\hat{f}_1\rangle_{t=0} = \langle\psi_1|\hat{f}_1(\hat{a}_1(0))|\psi_1\rangle_1 \tag{5.1.25}$$

$$\langle\hat{f}_3\rangle_{t=0} = \langle\psi_3|\hat{f}_3(\hat{a}_3(0))|\psi_3\rangle_3\,. \tag{5.1.26}$$

Upon complete conversion ($T = \pi/2\kappa A_p$), we have $\hat{a}_1(T) = \hat{a}_3(0)$ and $\hat{a}_3(T) = \hat{a}_1(0)$. The expectation value at time $t = T$ are then

$$\langle\hat{f}_1\rangle_{t=T} = \langle\psi_3|\hat{f}_1(\hat{a}_3(0))|\psi_3\rangle_3 \tag{5.1.27}$$

$$\langle\hat{f}_3\rangle_{t=T} = \langle\psi_1|\hat{f}_3(\hat{a}_1(0))|\psi_1\rangle_1\,. \tag{5.1.28}$$

Thus the properties of mode $\hat{a}_1$ are transferred to mode $\hat{a}_3$ after conversion. The fidelity of this transfer depends on how well the condition $T = \pi/2\kappa A_p$ is met.

5.2 The Frequency Conversion Setup

The frequency conversion setup is composed of two sections: the pump light generation section, and the telecom conversion section.

5.2.1 Telecom conversion

The telecom conversion setup is shown in Fig. 5.5, and begins with 1995 nm pump light and 866 nm signal photons from the ion-cavity system overlapped at a dichroic mirror. They are each guided by mirrors into a periodically-poled $LiNbO_3$ (PPLN) waveguide, where frequency conversion occurs. The pump light is polarised vertically (V) with respect to the optical bench for optimum conversion. The signal photons are an approximately even mixture of left- and right-circular polarisation. Both of these polarisations are projected onto horizontal or vertical with a 50% probability, so approximately half of the signal light passes through the crystal without mixing. A pump power of $P_p = 0.2\,\mathrm{W}$ is used, corresponding to an internal conversion efficiency of $\eta_{\mathrm{int}} = 0.5$. This value is less than the value calculated to optimise conversion efficiency of 0.26 W. As the pump light can leak through to the detectors and lead to additional background counts, a trade-off between conversion efficiency and stray photon counts must be made to optimise the signal-background ratio. The optimal value of $P_p = 0.2\,\mathrm{W}$ was found experimentally. The output

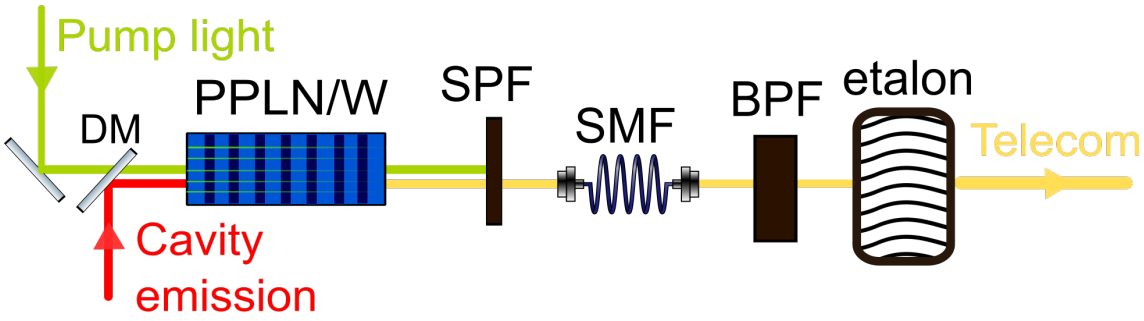

Figure 5.5: Diagram showing the setup for producing telecom light through frequency conversion. DM: dichroic mirror. PPLN/W: PPLN waveguide. SPF: short-pass filter. SMF: single mode fibre. BPF: band-pass filter.

of the waveguide is a mixture of pump light, unconverted signal light, and converted telecom light, plus additional light at different frequencies created through Raman scattering of the pump light. This output goes through several stages of filtering to remove, as far as possible, all but the telecom photons. The first stage is a short-pass filter with a cut-off between 1530 nm and 1995 nm and a transmission at 1530 nm of 50%. At the next stage, the light is coupled into a single-mode fibre (SMF) with an efficiency of 60% and passes through a fibre-coupled band-pass filter (BPF) with a width of 0.2 nm and a Fabry-Perot etalon with a bandwidth of 700 MHz, both centred at the converted wavelength. The transmission at 1530 nm of this stage is 14%. The BPF has a transmission of 20%, with the rest of the losses coming from mode-matching to the SMF and loss in the etalon. The total conversion efficiency from the beginning of the telecom conversion stage to the HBT setup is $\eta_{\mathrm{ext}} = 3\,\%$. This was measured directly using 866 nm laser light and a power meter before and after conversion. With the external efficiency of our frequency conversion setup, over short distances the direct cavity emission is more efficient than frequency conversion. For distances greater than 5 km, the attenuation in the optical fibre means that frequency conversion becomes more efficient, as can be seen from Fig. 5.6.

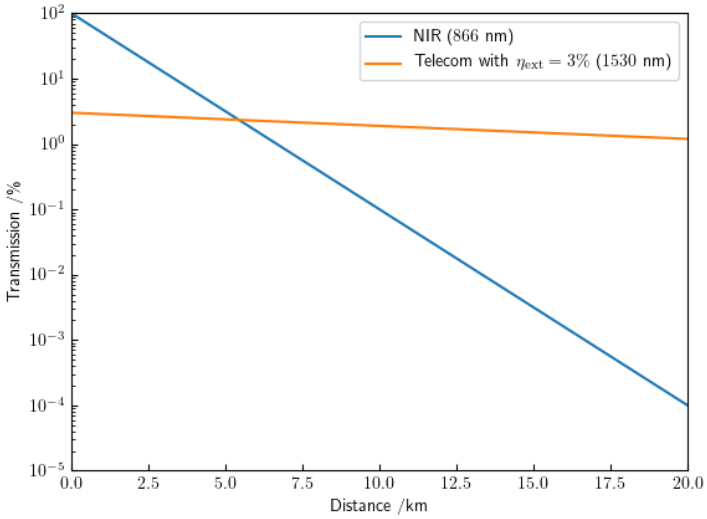

Figure 5.6: Percentage of the signal transmitted through optical fibre at 866 nm and 1530 nm with a 3% initial efficiency.

5.2.2 Pump light generation

The 1995 nm pump light used for frequency conversion to telecom was itself generated through frequency conversion; in this case, DFG between 1530 nm and 866 nm laser light. The 1530 nm laser light was generated by a distributed feedback laser with a linewidth of 10 MHz and amplified by an erbium-doped fibre amplifier with a maximum output of 450 mW. The 866 nm laser light was produced by an external-cavity diode laser with a linewidth on the order of a few MHz. The wavelength of this laser is set to resonance with the experimental cavity and locked using PID feedback with a wavemeter. The wavemeter is accurate to around 10 MHz. Both these lasers are overlapped at a dichroic mirror coupled into a second PPLN waveguide, producing light at 1995 nm. This light passes through a band pass filter centred at 2000 nm with a width of 50 nm to filter out unwanted light, particularly 1530 nm light which would pass through the filter at the telecom conversion stage. The pump light is then amplified by a thulium-doped fibre amplifier up to 1 W and sent to the telecom conversion system by a single-mode fibre.

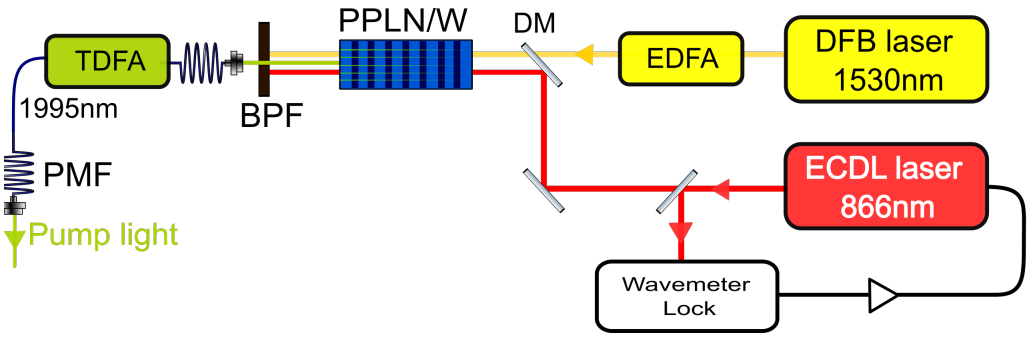

Figure 5.7: Diagram showing the setup for producing 1995 nm light through frequency conversion.

5.2.3 The Hanbury-Brown-Twiss setup

As discussed in Chapter 2, the statistics of a photon source may be characterised by its second-order coherence function $g^{(2)}(\tau)$, which describes correlations in photon number or intensity. For a single photon source, $g^{(2)}(0) = 0$, and $g^{(2)}(\tau) < 1$ indicates sub-Poissonian (and therefore nonclassical) statistics. The aim of this experiment was to demonstrate that, after frequency conversion, our source remained verifiably nonclassical, and that, after subtraction of background, could be shown to be a pure single photon source.

The measurement of the second-order correlation function of a source requires, in theory, a single detector and a time-to-digital converter (TDC). However, real detection equipment has a deadtime; after a photon detection, there is some amount of time before which no photons can be detected. This would lead to an artificial drop in coincidence counts around zero delay and obscure the presence of multi-photon events. In our case, the main source of deadtime was the discriminator that converted the NIM-like output signal of the detectors to a 5 V TTL signal that could be read by the TDC. An input into the discriminator produced a ≈ 200 ns TTL. If another photon were to be detected during this time window, the TTL would be extended rather than reset. As the TDC triggers on a rising or falling TTL edge, it would register only one count despite two photons being detected. To get around this a Hanbury-Brown-Twiss setup is used, in which two detectors, each with a channel on the TDC, are used after a 50:50 beam splitter (see Fig. 5.8). In this setup, if two photons are produced at the same time, there is a 50% chance that they will each go to different detectors, and so would both be counted. The normalised cross-correlation function of the detectors is equivalent to the second-order coherence function of the source. Two HBT setups for each of 866 nm and 1530 nm were used to measure the statistics of the light before and after conversion.

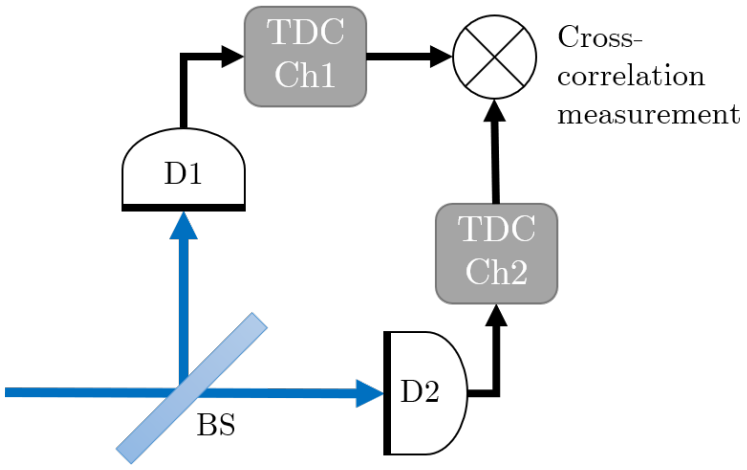

Figure 5.8: The Hanbury-Brown-Twiss setup for measuring the second-order coherence function of a photon source. The beam is split by a 50:50 beam splitter (BS), the outputs of which go to two detectors (D1 and D2). Detections are recorded by a time to digital converter (TDC).

5.2.4 Producing single photons

Single photons were produced in this experiment in a three-step sequence. In the first step the ion is Doppler cooled with a 397 nm beam red-detuned by $\Gamma/2$ from resonance and repumped with a 850 nm and 854 nm beam for 5.5 µs. In the second step, the cooling beam is extinguished, and the repumpers optically pump the population into $S_{1/2}$, distributed approximately evenly across the

$m_J = \pm 1/2$ states. The repumpers are then extinguished, and, after a delay of 0.7 µs, a 2.3 µs-long pulse of 397 nm light drives a cavity-assisted Raman transition. The pulse has a Gaussian temporal shape with a width $\Delta w = 0.5$ µs and an amplitude $\Omega = 0.3\Gamma$. The delay is to ensure that the cavity population built up in the cooling and state preparation stages can decay, and so will not be emitted during the single photon detection window. A delay of 0.5 µs after the Raman drive pulse ensures the single photon does not overlap with the cooling phase of the following cycle, and rounded the total time of the sequence to 10 µs. This would correspond to a 100 kHz repetition rate; however, due to a pause of 40 ns introduced by the the FPGA between cycles, the actual repetition rate was 99.6 kHz. The magnetic field was set to 0.5 G along the cavity axis. At this field strength, the Zeeman splitting is approximately 0.3 MHz, which is comparable to the cavity linewidth and therefore not large enough to resolve individual Raman transitions between the sublevels. The output of the cavity is therefore a mixture of σ^+ and σ^- photons from different transitions.

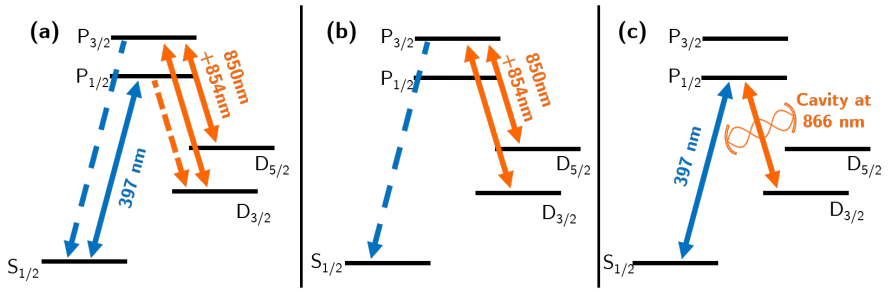

Figure 5.9: The laser pulse sequence for producing single photons. **(a)** Doppler cooling. **(b)** State preparation through optical pumping. **(c)** Cavity-assisted Raman transition.

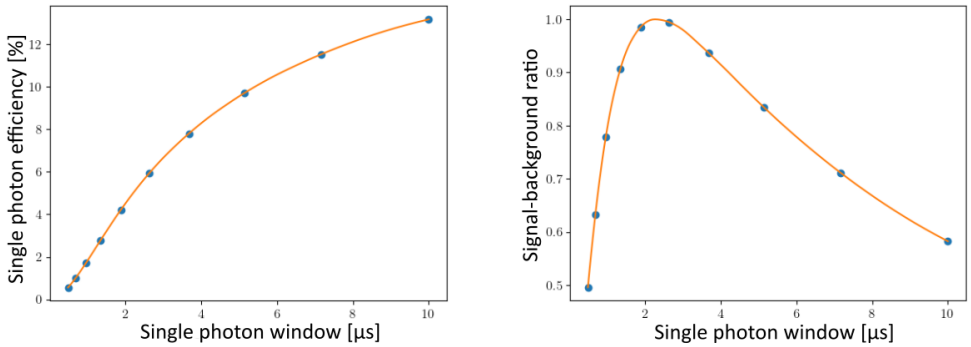

(a) **(b)**

Figure 5.10: (**a**) Single photon efficiency in arbitrary units with increasing laser pulse width and single photon window, extracted from simulations of the ion-cavity system. (**b**) The signal-background ratio assuming a linear increase in background count rate with window length, normalised to unity. The blue points are results from the simulation, and the orange curve is a quadratic interpolation used to find the maximum value of the signal-background ratio, which occurs at 2.3 µs.

The single photon pulse length was chosen to optimise the signal-to-background ratio (SBR) after QFC. As background counts are randomly distributed in time, the total background counts detected increases linearly as the photon window is increased. The single photon efficiency, however, has a nonlinear relationship with the length of the laser pulse that drives the cavity-assisted Raman transition, as shown in Fig. 5.10b. This is extracted from simulations of the ion-cavity system. The

width of the Gaussian pulse used to drive the single photon emission is increased in proportion to the photon window, and the expected photon generation probability is extracted. For short times there is a greater than linear increase in efficiency, but at a certain point there are diminishing returns. Fig. 5.10b shows the trend in SBR versus photon length based on these simulations. Based on an interpolation of the data, the optimal photon length for our system was 2.3 µs. With this pulse length, photons were detected with a probability of $P_{\text{det}} = 1.63(4)\,\%$. The uncertainty assumes Poissonian counting statistics. The known losses in the system are the bandpass filters for removing the locking light ($\eta_{\text{filter}} = 0.8$), the coupling to the collection fibre ($\eta_{\text{couping}} = 0.66$), the loss through the fibre beam splitter ($\eta_{\text{BS}} = 0.86$), and the detector efficiencies ($\eta_{\text{det}} = 0.8$). Based on these efficiencies, the probability of emitting a photon from the cavity was

$$P_{\text{emit}} = \frac{P_{\text{det}}}{\eta_{\text{filter}}\eta_{\text{coupling}}\eta_{\text{BS}}\eta_{\text{det}}} = 4.49\,\%. \tag{5.2.1}$$

The simulations give an efficiency of 5.13 %, a roughly 11 % discrepancy. The photon shapes match well between the simulation and data (see Fig. 5.15), suggesting that there are some losses not fully accounted for, rather than a problem with the simulation parameters.

5.3 Results

The raw data collected from the experiment are a list of photon arrival times and associated TDC channels. Only detections that occur during the single photon window are counted. This is done by gating the signal between the detectors and TDC with a simple AND gate. The ion lifetime in the trap is not long enough to obtain enough data for to achieve a reasonable uncertainty. The data collection was therefore stopped when the ion dropped out of the trap and a new data set started when a new ion was reloaded. These data sets were analysed individually and then summed. The intensity cross correlation function $g^{(2)}(\tau)$ is calculated by taking the difference between each time stamp on one channel and every time stamp on the other. Sorting the resulting time differences into time bins, a histogram such as the one in Fig. 5.11 is produced. The clearly distinguished peaks are due to the pulsed source; each peak separated by the period of the experimental cycle T, and the shape of the peaks are the autocorrelation of the single photon shape, which is approximately Gaussian. When evaluating $g^{(2)}$ we are interested in the value for the entire photon coincidence window, rather than a specific time. We therefore calculate $g^{(2)}(n)$, where $n \in \mathbb{Z}$ denotes the coincidence window n periods from $\tau = 0$. We then normalise the cross-correlation histogram to obtain the second-order coherence function as

$$g^{(2)}(n) = \frac{N_{\text{rep}} C_n}{N_1 N_2}, \tag{5.3.1}$$

where N_{trig} is the number of times the single photon sequence was repeated, C_n is the number of coincidences which occurred in the nth window, and N_1 and N_2 are the total numbers of counts on each detector. This produces a histogram such as the one in Fig. 5.12. For a single photon source, we expect $g^{(2)}(0) = 0$. However, the timestamps from the TDC do not correspond only to photons from the ion-cavity system, but also background counts. The correlations observed come from three sources: signal-signal, signal-background, and background-background. If we assume that the background counts are uncorrelated with each other and with the single photon source, then for a source with $g^{(2)}_{\text{source}}(n)$ and a signal-background ratio SBR, the measured value of $g^{(2)}(n)$ becomes

$$g^{(2)}_{\text{meas}}(n) = 1 + \rho^2 \left[g^{(2)}_{\text{source}}(n) - 1 \right], \tag{5.3.2}$$

where $\rho = \mathrm{SBR}/(1+\mathrm{SBR})$ [96]. We can see that as the SBR tends to zero, $g^{(2)}_{\mathrm{meas}}(n) \to 1$ for all n, as expected from uncorrelated noise, while as the SBR tends to infinity, $g^{(2)}_{\mathrm{meas}}(n) \to g^{(2)}_{\mathrm{source}}(n)$. It is always true that $g^{(2)}(n \neq 0) = 1$, and so the effect of the background counts is only seen in second-order correlation function as an offset on the value at zero delay. If we assume a perfect single photon source, then we have

$$g^{(2)}_{\mathrm{meas}}(0) = 1 - \rho^2. \tag{5.3.3}$$

If we measure $g^{(2)}(0) < 1$ then we have a verified nonclassical source of photons without any assumptions or subtraction of background. If we assume that the background is uncorrelated with itself or the source, and $g^{(2)}_{\mathrm{meas}}(0)$ agrees with Eq. (5.3.3), then we have verified that the source produces pure single photons with a negligible number of multi-photon events. If the experiment were run for infinite time, $g^{(2)}(n \neq 0)$ would average to unity. For a real data set, the arrival time difference cannot be greater than the data collection time, so the number of coincidence counts decreases as the time difference tends to infinity. We therefore only consider small values of n when averaging $g^{(2)}(n \neq 0)$.

Three sets of data were collected to produce three second-order coherence functions. The first was the direct cavity emission without frequency conversion, to verify and benchmark the ion-cavity system as a single-photon source. The second was after frequency conversion, to show that the conversion process does not introduce correlated background noise or multi-photon events . The third was after transmitting the frequency converted photons through a 10 km spool of optical fibre, to demonstrate that the nonclassical statistics of the source could still be measured after long-distance transmission.

5.3.1 Sources of background counts

For the direct cavity emission, the sources of background counts are the intrinsic dark counts of the detectors, ambient light and laser scatter coupled into the collection fibre, and residual cavity photons not generated by the Raman process. These background count rates were measured with the detectors gated as in the experiment. The detector dark counts were measured as 0.5 cps by blocking the detector inputs with a metal cap. With the system connected to the detectors but no lasers on, the background count rate increased to 1 cps, meaning ambient light accounted for 0.5 cps. With the lasers turned on and cavity locked, but no ion present, no increase in background count rate was observed. With an ion present in the trap but the Raman drive beam switched off, again no increase in counts was seen, meaning cavity emission from residual population is negligible. The background count rate is therefore entirely accounted for by detector dark counts and ambient light.

With the QFC system connected, additional background was introduced. Firstly, as different detectors were used for the telecom wavelength, the dark count rate and sensitivity to ambient light changed. A new detector dark count rate of 1 cps was measured. The strong pump light introduced another source of background counts both through directly coupling into the detectors, and through Raman scattering in the PPLN waveguide. Not all of this light was removed by the filters, resulting in a background count rate of 19 cps. When the 10 km fibre was included, the background signal from light coupled into the fibre experienced attenuation, reducing it from 18 cps to 7.2 cps, giving a total of 8.2 cps.

In addition to the background counts, there is also the possibility of multi-photon events from the Raman process. The finite lifetime of the $D_{3/2}$ state means there is a possibility for the ion to decay

to the $S_{1/2}$ state. If this occurs after a cavity photon has been produced in a Raman transition, the ion could undergo a second Raman transition and produce a second photon. This state has a lifetime of 1.17 s. The probability of this decay occurring within the single photon window, assuming the ion begins in the $D_{3/2}$ state, is $P_{\text{decay}} = 2{\times}10^{-6}$. The probability of producing a second photon is $P_{\text{decay}}P_{\text{det}} \approx 1{\times}10^{-8}$, negligible compared to the effect of the background light and detector dark counts.

Direct cavity emission

The data presented in Fig. 5.11 and Fig. 5.12 were collected over 180 s. A total of 294 020 photons were collected, a rate of $R_{\text{NIR}} = 1633$ cps. In this time, two counts occurred within the same single photon window. After normalisation using Eq. (5.3.2) this gives $g^{(2)}(0) = 1.7(12){\times}10^{-3}$. The average of $g^{(2)}(n \neq 0)$ is unity, showing that the histogram is properly normalised and that there are no correlations in the background or cavity emission between experimental cycles. Given the SBR of 1633, for a single photon source we expect $g^{(2)}(0) = 1.2{\times}10^{-3}$ from Eq. (5.3.3). This is within the uncertainty of the data, demonstrating that the observed coincidences are due to the background counts.

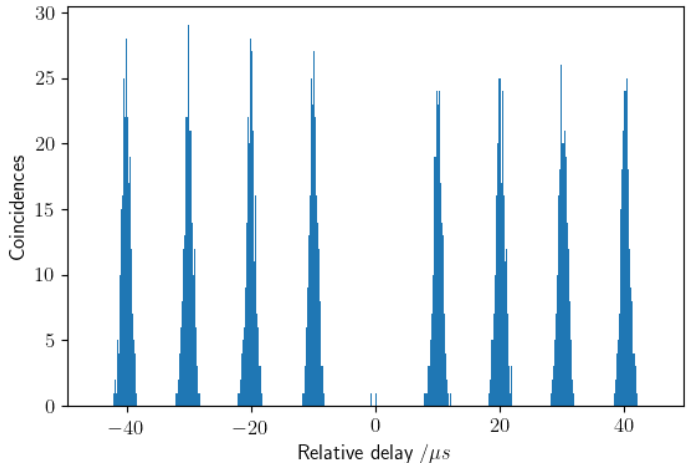

Figure 5.11: Histogram showing the relative difference in arrival times between photons emitted from the ion-cavity system without frequency conversion.

Frequency converted photons

After frequency conversion, the single photon detection rate dropped to $R_{\text{tel}} = 26.3$ cps. Half the photons from the cavity weren't converted due to their polarisation. The rest of the loss in counts is due to the external efficiency of the frequency conversion setup. The ratio of count rates

$$\eta_{\text{ext}} = \frac{R_{\text{tel}}}{R_{\text{NIR}}} = 0.032(6) \tag{5.3.4}$$

is consistent with the value measured when characterising the system with a laser, $\eta_{\text{ext}} = 0.03$. 1 325 433 detection events occurred over 8.1 h. The normalised histogram is shown in Fig. 5.13. A background count rate of 19.0 cps was measured, equating to a SBR of 1.38. From Eq. (5.3.2) we calculate $g^{(2)}(0) = 0.67(7)$, in agreement with the value of 0.660 from Eq. (5.3.3).

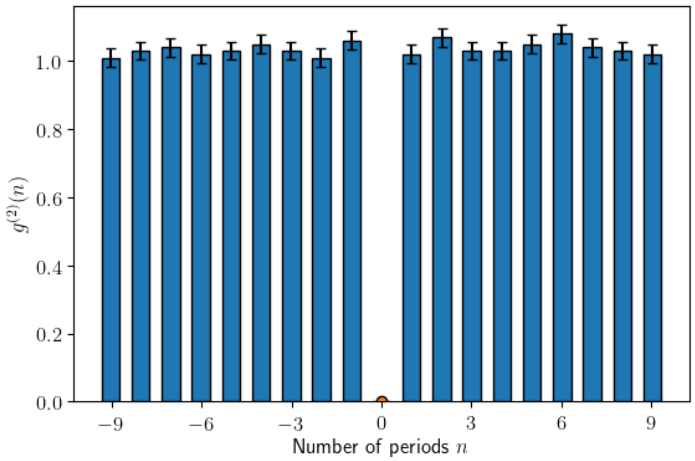

Figure 5.12: The second-order correlation function for the ion-cavity emission at 866 nm, before conversion. The blue bars represent the sums of the counts within each coincidence window n periods from zero delay, normalised to the total counts to produce $g^{(2)}$. The orange point at $n = 0$ indicates the value of $g^{(2)}_{\text{meas}}(0)$. The error bars are one standard deviation assuming Poissonian counting statistics.

Long-distance transmitted photons

After transmission through the optical fibre, the signal reduced to 13.0 cps. For an attenuation of 0.2 dB km^{-1} at 1530 nm, we would expect a rate of 16.6 cps. The additional loss may be due to coupling losses or a worse than specified fibre attenuation. The background count rate also reduced to 8.2 cps. The normalised histogram is presented in Fig. 5.14. For the SBR of 1.53, we expect to find $g^{(2)}(0) = 0.634$, in agreement with the value measured of 0.59(7).

Source	$g^{(2)}_{\text{meas}}(0)$	$g^{(2)}_{\text{SBR}}(0)$	$g^{(2)}(0)$
866 nm	$1.7(12)\times10^{-3}$	1.2	$0.5(12)\times10^{-3}$
1530 nm	0.67(7)	0.66	0.07(7)
1530 nm with 10 km fibre	0.59(7)	0.63	0.04(7)

Table 5.1: Values of $g^{(2)}(0)$ after background subtraction. All values are consistent with zero.

Photon temporal shape

For quantum networking, it is important to maintain the temporal shape of single photons be controllable and consistent, as it impacts the fidelity and efficiency of entanglement and state transfer schemes. To confirm that the frequency conversion process does not introduce time-jitter or otherwise affect the photon shape, the photon shapes are compared in Fig. 5.15. The temporal shape of the photon is the variation in the probability of detecting the photon in time. It can be constructed by building a histogram of photon arrival times at a detector with respect to a trigger. The data in the figure have had the background counts subtracted, assuming the background count rate is constant in time, and normalising the resulting histogram to unity. The shapes match well with each other, showing that no significant time-jitter is introduced. The data also match well with the simulation, also shown in the figure. As will be explored in greater detail in the following chapter, the observed photon shape is in actuality an average over many photon shapes rather than a single coherent wavepacket, due to the decoherence effects inherent to the photon generation process.

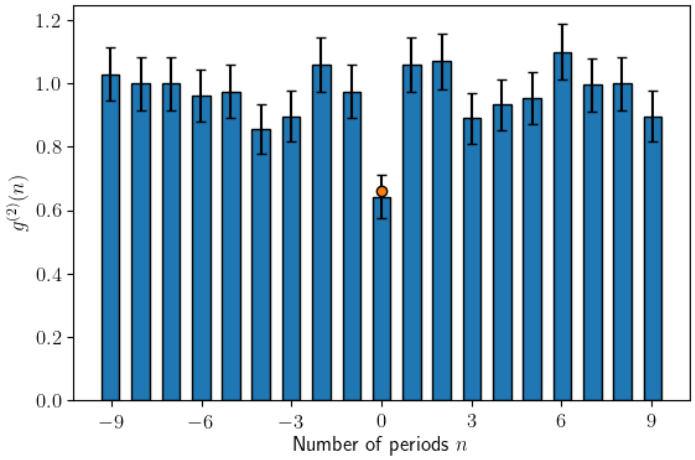

Figure 5.13: The second-order correlation function for the frequency converted cavity emission at 1530 nm. The blue bars represent the sums of the counts within each coincidence window n periods from zero delay, normalised to the total counts to produce $g^{(2)}$. The orange point at $n = 0$ indicates the value of $g^{(2)}_{\mathrm{SBR}}(0)$. The error bars are one standard deviation assuming Poissonian counting statistics.

5.4 Outlook

The aim of this experiment was to take a step towards the establishment of entanglement between trapped ions separated by long distances using frequency conversion. This was the first demonstration of quantum frequency conversion with a trapped ion-cavity system, enabling transmission of single photons over such a long distance. The agreement between the measured value $g^{(2)}(0) = 0.59(7)$ and the value calculated from the SBR of $g^{(2)}(0) = 0.634$ indicates that all measured multi-photon events can be attributed to background counts and that the ion-QFC system is a pure single-photon source. The measured $g^{(2)}(0)$ for the unconverted photons is comparable to other results using trapped ions [42].

An experiment establishing entanglement between a trapped $^{40}Ca^{+}$ ion and a telecom photon via QFC was published while the manuscript for this experiment was in preparation [88]. The second-order coherence function was not explicitly measured, but from the reported SBR of 24.3 after frequency conversion, a value of approximately 0.08 could be expected. The improvement compared to this work is mostly from to the significantly higher external conversion efficiency ($\eta_{\mathrm{ext}} = 26.5\,\%$), due in large part to the different noise filtering methods used, and the lower background counts due to the shorter photon length of 300 ns. That experiment did not use an optical cavity and converted to the more lossy telecom O-band at 1310 nm.

If one assumes a pure single-photon source, the second-order coherence function effectively becomes a measure of SBR, and may be used estimate the entanglement fidelity that could be measured using the source. Using the photon generation and background count rates in this experiment, with some reasonable improvements to the system to increase the signal-background ratio and assuming unity fidelity ion-photon entanglement, it was calculated that ion-ion entanglement could be established over 60 km using similar systems[1]. Since the paper was published, work has been completed in a different system using $^{40}Ca^{+}$ coupled to an optical cavity demonstrating ion-photon entanglement over 50 km of fibre via QFC [89]. Later, another group achieved matter-matter entanglement over 50 km of fibre using cold atomic ensembles coupled to ring cavities [93], with a reported

[1] See the supplemental material of the paper [87] for a full description of the entanglement scheme and assumptions made.

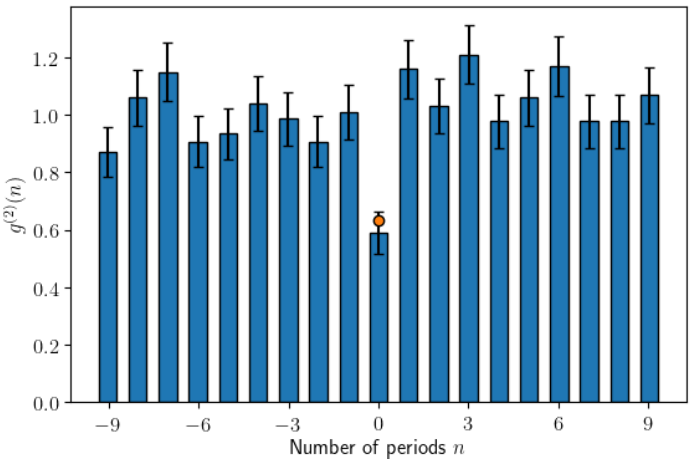

Figure 5.14: The second-order correlation function for the ion-cavity emission at 866 nm, before conversion. The blue bars represent the sums of the counts within each coincidence window n periods from zero delay, normalised to the total counts to produce $g^{(2)}$. The orange point at $n = 0$ indicates the value of $g^{(2)}_{\text{meas}}(0)$. The error bars are one standard deviation assuming Poissonian counting statistics.

$g^{(2)}(0) \approx 0.4$. Both of these results are comparable to our prediction that entanglement could be established over dozens of kilometres with relatively minor improvements to the SBR. This serves as further indication that long-distance quantum networks could be developed using systems such as the one presented in this thesis with current technology.

The estimation of entanglement over 60 km makes the assumption that the photons are indistinguishable; however, photons produced by such systems have a certain degree of mutual distinguishability, which reduces the fidelity of the entanglement. This distinguishability was cited as a source of reduction in fidelity in the cold atom entanglement experiment mentioned previously. The next chapter explores this distinguishability and demonstrates a new scheme for producing single photons that improves the indistinguishability.

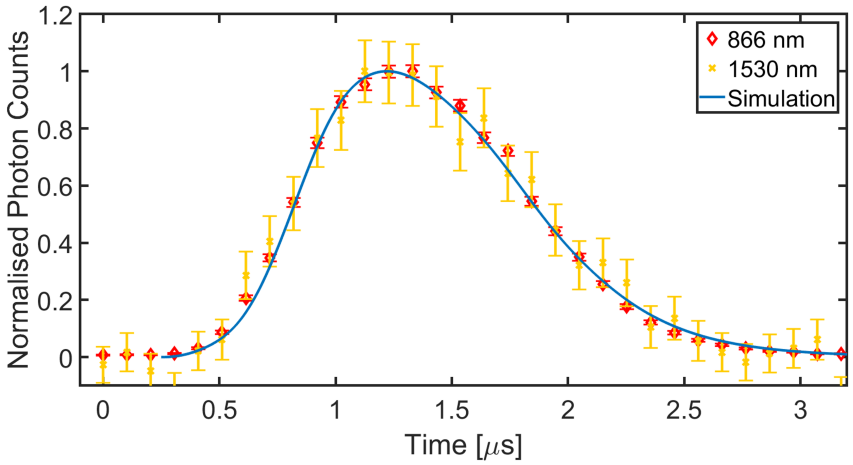

Figure 5.15: The temporal shapes of the single photons at 866 nm (red diamonds) line), 1530 nm (yellow crosses), and the simulated photon shape, with peak counts normalised to unity. Uncertainties are one standard deviation assuming Poissonian counting statistics. Photons were collected over 90 s for 866 nm and 1000 s for 1530 nm.

Chapter 6

Indistinguishable Single Photons

Quantum networking with photons relies on the ability to produce photons in a consistent manner in both the deterministic and probabilistic approaches outlined in Chapter 1. In deterministic networking, not only must photons be produced with near-unity efficiency, but they must be deterministic in their other properties, such as polarisation, spectral profile, and spatio-temporal structure [97]. Varying these properties affects the probability of a photon being absorbed or fidelity of the qubit state mapping. In the probabilistic scheme, the heralding of entanglement relies on the interference of two photons at a beam splitter. As discussed in more detail in Section 6.5, any distinguishability between the photons will result in a loss in visibility of the interference and therefore a loss in fidelity of the entanglement [98–100]. Distinguishability can occur in photons produced in coherent processes through decoherence in the quantum system or through experimental inhomogeneity.

The scheme for producing single photons in the previous chapter is similar to those used to produce ion-photon entanglement using $^{40}Ca^{+}$ in previous experiments [35, 88, 89], where the ion begins in the $S_{1/2}$ state and ends in one of the metastable D states. Similar schemes are used in other common ion species, such as barium [101]. In this chapter, we will discuss how distinguishability occurs in this process, and present a different scheme which can make the photons less distinguishable. The distinguishability of photons from each scheme is characterised using the Hong-Ou-Mandel two-photon interference effect.

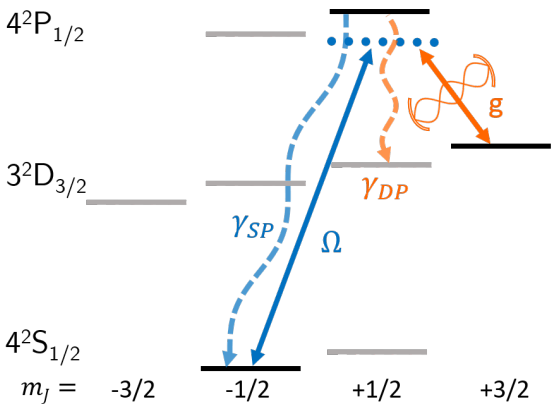

Figure 6.1: Cavity-STIRAP scheme for producing single photons starting in the state $|S_{1/2}; m_J = -1/2\rangle$ and ending in $|D_{3/2}; m_J = 3/2\rangle$. The decays γ_{SP} as γ_{DP} shown as dashed lines represent decays to all Zeeman sublevels.

6.1 Photon distinguishability

The first single photon scheme is shown in Fig. 6.1. A cavity-STIRAP process is driven from $|\mathrm{S}_{1/2}; m_J = -1/2\rangle$ to $|\mathrm{D}_{3/2}; m_J = 3/2\rangle$. A magnetic field splits the levels such that this transition can be resolved. In the previously mentioned ion-photon entanglement experiments, the $\mathrm{D}_{5/2}$ state was used, and the photons were produced using a far-detuned Raman process rather than a near-detuned STIRAP process, though the principles discussed apply broadly to both cases. A key source of distinguishability between photons emitted from the cavity is the spontaneous emission channel γ_{SP}. The large branching ratio to the $\mathrm{S}_{1/2}$ state ($\gamma_{SP} = 10.8\,\mathrm{MHz} \gg \gamma_{DP} = 0.744\,\mathrm{MHz}$) means that if the Raman transition fails and an off-resonant photon is scattered, there is a high chance that the ion will decay back to the initial state. For applications where the goal is to optimise only single photon efficiency, this is desirable, as after the population is recycled there is still the possibility to produce a photon. However, this reduces the coherence of the emitted photon. The recycling process creates a time-jitter in the emitted photon. Further, the drive beam has a time-dependant Rabi frequency ($\Omega_{\mathrm{driv}}(t)$), tailored to achieve adiabatic state transfer from the initial conditions $|\mathrm{S}_{1/2}; m_J = -1/2\rangle$, $\Omega_{\mathrm{driv}}(0) = 0$. If a decay occurs at a time t_1 after the onset of the drive beam, the ion will be projected to the $|\mathrm{S}_{1/2}; m_J = -1/2\rangle$ state with the drive beam at $\Omega_{\mathrm{driv}}(t = t_1)$. The photon produced by the resulting process will have an altered temporal profile, and the conditions for adiabaticity may not be met. This effect compounds with increasing spontaneous decay events occurring before a photon is produced. The photon emitted from the cavity is a probabilistic mixture of photons produced after different numbers of scatter events. This means that, while near-unity efficiency can be achieved, this scheme is not suitable for deterministic quantum networking. Spontaneous emission to a state other than the initial state does not lead to photon distinguishability, but rather reduces the efficiency of the process, as the atom no longer interacts with the laser or cavity field, and so system ceases to evolve.

To reduce the impact of spontaneous emission on the coherence of the photon, we introduce a new single photon scheme, shown in Fig. 6.2. In this scheme, a cavity-STIRAP is driven between $|\mathrm{D}_{3/2}; m_J = -3/2\rangle$ and $|\mathrm{D}_{3/2}; m_J = 1/2\rangle$. This means that recycling to the initial state depends on γ_{DP}, and so is greatly reduced compared to the $S_{1/2} \rightarrow D_{3/2}$ case. To demonstrate the difference between these two cases, a Monte Carlo simulation of the ion-cavity system can be performed, extracting the number of decays back to the initial state that occur before a photon is emitted from the cavity. The distribution of the number of decays for 20,000 simulated runs of each single photon scheme is shown in Fig. 6.3. The results show that in approximately 90% of cases for the $D_{3/2} \rightarrow D_{3/2}$ scheme, no decays occur before a photon is emitted, resulting in a highly pure photon state. Conversely, the $S_{1/2} \rightarrow D_{3/2}$ scheme shows a relatively flat distribution of decays (on a log scale), indicating a highly mixed photon state. We must still consider the effect of γ_{SP}, which now takes the ion out of the Raman process. The result is photons which are less distinguishable, but are produced with a lower probability. This is ideal for probabilistic networking protocols, where efficiency is sacrificed for fidelity.

The distinguishability of photons can be characterised through several key properties: polarisation, temporal profile, and spectral profile. Polarisation is generally fixed by the transition chosen, assuming the transitions are well resolved. However, after emission, time-dependent birefringence in optical components can cause polarisation distinguishability between the photons. Frequency broadening can be introduced by various experimental noise sources. Magnetic field noise shifts the Zeeman sublevels and therefore changes the laser and cavity detunings. Fluctuations in the laser frequency and cavity length can be introduced by mechanical or electronic noise. These all

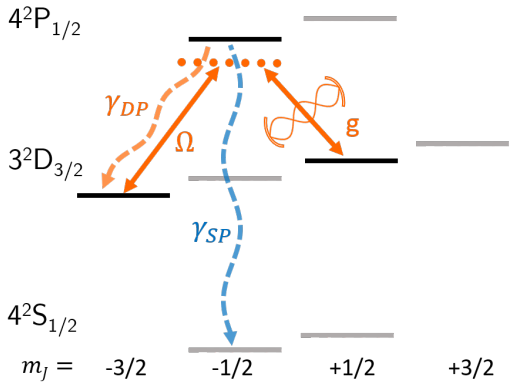

Figure 6.2: Cavity-STIRAP scheme for producing single photons starting in the state $|D_{3/2}; m_J = -3/2\rangle$ and ending in $|D_{3/2}; m_J = 1/2\rangle$. The decays γ_{SP} and γ_{DP} shown as dashed lines represent decays to all Zeeman sublevels.

contribute to inhomogeneous broadening of the frequency profile of the photons, and reduce the photon's coherence time.

6.2 Two-photon interference

To measure the distinguishability of photons we employ the Hong-Ou-Mandel (HOM) interference effect [37]. When two indistinguishable photons meet at a balanced beam splitter at the same time, they will always leave the same exit port. The HOM effect results directly from a quantum description of the beam splitter. Consider two identical photons incident on two input modes $\hat{a}^\dagger$ and $\hat{b}^\dagger$ of a beam splitter, described by the Fock states

$$\hat{a}^\dagger \hat{b}^\dagger |0,0\rangle_{a,b} = |1,1\rangle_{a,b} . \tag{6.2.1}$$

The beam splitter transforms these input modes into the output modes $\hat{c}^\dagger$ and $\hat{d}^\dagger$ by:

$$\begin{bmatrix} \hat{a}^\dagger \\ \hat{b}^\dagger \end{bmatrix} = \frac{1}{\sqrt{2}} \begin{bmatrix} 1 & 1 \\ 1 & -1 \end{bmatrix} \begin{bmatrix} \hat{c}^\dagger \\ \hat{d}^\dagger \end{bmatrix} . \tag{6.2.2}$$

The two-photon input state therefore becomes:

$$\hat{a}^\dagger \hat{b}^\dagger |0,0\rangle_{a,b} \rightarrow \frac{1}{2} \left(\hat{c}^\dagger + \hat{d}^\dagger\right) \left(\hat{c}^\dagger - \hat{d}^\dagger\right) |0,0\rangle_{cd} \tag{6.2.3}$$

$$= \frac{1}{2} \left(2\,|2,0\rangle_{cd} + |1,1\rangle_{cd} - |1,1\rangle_{cd} + 2\,|0,2\rangle_{cd}\right) \tag{6.2.4}$$

$$= \frac{1}{\sqrt{2}} \left(|2,0\rangle_{cd} - |0,2\rangle_{cd}\right) . \tag{6.2.5}$$

We can see that the probability amplitudes if cases where the photons leave by different ports cancel due to the π phase-shift induced in the reflection of the $\hat{b}^\dagger$ mode. The only possibilities, therefore, are those in which both photons leave by the same port. This is the HOM interference effect. If the input photons are not identical, but instead partially distinguishable, then the interference will not occur perfectly and there will be some probability of the photons leaving from different ports. The probability of the photons leaving from different ports depends on the degree of distinguishability between the photons, up to 50% if the photons are fully distinguishable. Placing detectors at each output port allows these probabilities to be measured via the intensity cross-correlation function.

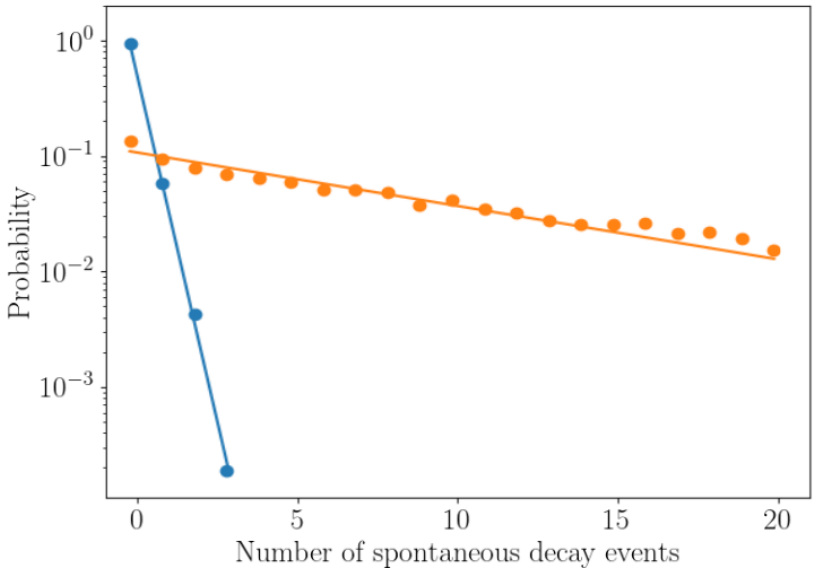

Figure 6.3: Distributions of the numbers of spontaneous decays that occur before a photon in produced in the $S_{1/2} \rightarrow D_{3/2}$ (orange) and $D_{3/2} \rightarrow D_{3/2}$ (blue) schemes. For the $D_{3/2} \rightarrow D_{3/2}$ scheme, no decays occur in 90% of cases, while the $S_{1/2} \rightarrow D_{3/2}$ exhibits a relatively flat distribution. The points derive from Monte Carlo simulations of the cavity-STIRAP processes with 20,000 trajectories each. Straight lines fits are shown for clarity.

By rotating the polarisation of one of the fields to be perpendicular to the other, a reference measurement where no interference occurs can be taken. The contrast between these perpendicular and parallel measurements gives a measure of the distinguishability between the input fields. It is conventional to give this contrast as the HOM visibility, defined as

$$V = 1 - \frac{P_\mathrm{c}}{P_\mathrm{ref}}, \tag{6.2.6}$$

where P_c is the coincidence probability for the interference measurement, and P_ref is the coincidence probability for the reference measurement.

The distinguishability of photons from a single source can be measured using the Hong-Ou-Mandel interferometer, shown in Fig. 6.4. Photons are emitted from the source at regular intervals separated by a time T. A beam splitter directs the photons down one of two arms, which meet at another beam splitter, where the interference occurs. One of the arms has a delay with a photon travel time of T, so the photons arrive simultaneously at the second beam splitter. Detectors at each output of the beam splitter are connected to a TDC, from which a cross-correlation measurement is performed.

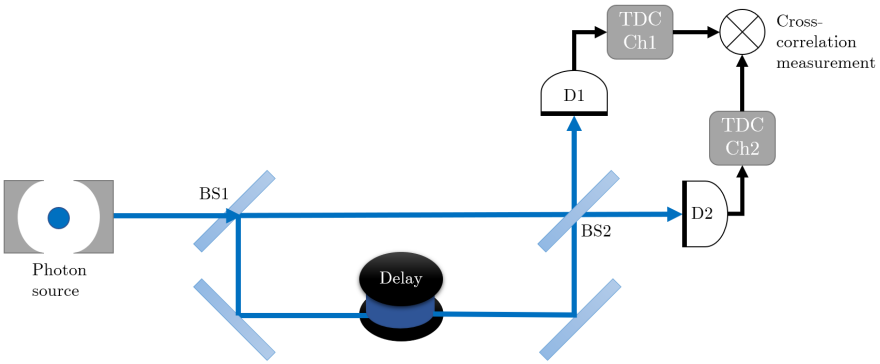

Figure 6.4: The Hong-Ou-Mandel interferometer.

6.2.1 Time-resolved two-photon interference

If the time resolution of the detectors is much smaller than the width of the photons, the time-resolved HOM interference pattern can be seen. In this case, the photons is expressed in terms of the time-dependent mode operator $\hat{a}(t)$, and we write the second-order cross-correlation function of the beam splitter outputs as:

$$G^{(2)}_{cd}(t, t+\tau) = \langle \hat{d}^\dagger(t)\hat{c}^\dagger(t+\tau)\hat{c}(t+\tau)\hat{d}(t)\rangle \,. \tag{6.2.7}$$

Rewriting the beam splitter equation in Eq. (6.2.2) for the output mode operators:

$$\begin{bmatrix} \hat{c} \\ \hat{d} \end{bmatrix} = \frac{1}{\sqrt{2}} \begin{bmatrix} 1 & -1 \\ 1 & 1 \end{bmatrix} \begin{bmatrix} \hat{a} \\ \hat{b} \end{bmatrix} . \tag{6.2.8}$$

We can write Eq. (6.2.7) in terms of the input fields:

$$\begin{aligned} \langle \hat{d}^\dagger(t)\hat{c}^\dagger(t+\tau)\hat{c}(t+\tau)\hat{d}(t)\rangle = \frac{1}{4}\sum_{(\hat{p},\hat{q})} [&\langle \hat{p}^\dagger(t)\hat{p}^\dagger(t+\tau)\hat{p}(t+\tau)\hat{p}(t)\rangle + \langle \hat{p}^\dagger(t)\hat{p}(t)\rangle \langle \hat{q}^\dagger(t+\tau)\hat{q}(t+\tau)\rangle \\ &- \langle \hat{p}^\dagger(t+\tau)\hat{p}(t)\rangle \langle \hat{q}^\dagger(t)\hat{q}(t+\tau)\rangle - \langle \hat{p}^\dagger(t+\tau)\hat{p}^\dagger(t)\rangle \langle \hat{q}(t+\tau)\hat{q}(t)\rangle \\ &+ \langle \hat{q}(t)\rangle \langle \hat{p}^\dagger(t)\hat{p}^\dagger(t+\tau)\hat{p}(t+\tau)\rangle + \langle \hat{q}^\dagger(t)\rangle \langle \hat{p}^\dagger(t+\tau)\hat{p}(t+\tau)\hat{p}(t)\rangle \\ &- \langle \hat{p}^\dagger(t+\tau)\rangle \langle \hat{p}^\dagger(t+\tau)\hat{p}^\dagger(t)\hat{p}(t)\rangle - \langle \hat{q}^\dagger(t+\tau)\rangle \langle \hat{p}^\dagger(t)\hat{p}(t+\tau)\hat{p}(t)\rangle]. \end{aligned} \tag{6.2.9}$$

Here, $(\hat{p}, \hat{q}) \in \{(\hat{a}, \hat{b}), (\hat{b}, \hat{a})\}$; that is, the sum is over all permutations of the operators $\hat{a}$ and $\hat{b}$. The first term depends on the second-order correlation function of the input modes. If we assume a pure single photon source, we may immediately neglect this term, as $g^{(2)}(\tau) = 0$. Due to the lack of fixed phase relation between photons in the input modes, the effect of the final five terms will average out over a large number of runs. This may be seen by considering the rewriting the operator as $\hat{p} = \hat{p}' e^{i\phi}$, where ϕ is the relative phase between the input fields. Taking the fourth term as an example, we have

$$\langle \hat{p}^\dagger(t+\tau)\hat{p}^\dagger(t)\rangle \langle \hat{q}(t+\tau)\hat{q}(t)\rangle = \langle \hat{p}'^\dagger(t+\tau)\hat{p}'^\dagger(t)\rangle \langle \hat{q}(t+\tau)\hat{q}(t)\rangle \, e^{-2i\phi}. \tag{6.2.10}$$

Averaging over a large number of runs approximates integrating over all values of ϕ, causing these phase-dependent terms to vanish, as

$$\int_{-\infty}^{\infty} e^{-2i\phi} d\phi = 0. \tag{6.2.11}$$

Eq. (6.2.9) then reduces to

$$\begin{aligned}\langle \hat{d}^\dagger(t)\hat{c}^\dagger(t+\tau)\hat{c}(t+\tau)\hat{d}(t)\rangle = \frac{1}{4}\sum_{(\hat{p},\hat{q})}[\,&\langle \hat{p}^\dagger(t)\hat{p}^\dagger(t+\tau)\hat{p}(t+\tau)\hat{p}(t)\rangle + \langle \hat{p}^\dagger(t)\hat{p}(t)\rangle \langle \hat{q}^\dagger(t+\tau)\hat{q}(t+\tau)\rangle \\ &- \langle \hat{p}^\dagger(t+\tau)\hat{p}(t)\rangle \langle \hat{q}^\dagger(t)\hat{q}(t+\tau)\rangle].\end{aligned} \tag{6.2.12}$$

Even given a fixed phase relation, these contributions would be expected to oscillate rapidly and have a relatively small contrition to the interference, and would therefore be unlikely to be observable in the experiment. We may simplify the equation further by considering that the inputs $\hat{a}(t)$ and $\hat{b}(t)$ in the experiment derive from the same source, and so are statistically identical. We can therefore write Eq. (6.2.12) in terms of a single input operator $\hat{a}$:

$$\langle \hat{d}^\dagger(t)\hat{c}^\dagger(t+\tau)\hat{c}(t+\tau)\hat{d}(t)\rangle = \frac{1}{2}[\langle \hat{a}^\dagger(t)\hat{a}^\dagger(t+\tau)\hat{a}(t+\tau)\hat{a}(t)\rangle \tag{6.2.13}$$

$$+ \langle \hat{a}^\dagger(t)\hat{a}(t)\rangle \langle \hat{a}^\dagger(t+\tau)\hat{a}(t+\tau)\rangle \tag{6.2.14}$$

$$- \langle \hat{a}^\dagger(t+\tau)\hat{a}(t)\rangle \langle \hat{a}^\dagger(t)\hat{a}(t+\tau)\rangle]. \tag{6.2.15}$$

As we are interested only in the relative arrival times of photons on the detectors, we integrate this two-time correlation function over all time t:

$$G^{(2)}_{cd}(\tau) = \int \langle \hat{d}^\dagger(t)\hat{c}^\dagger(t+\tau)\hat{c}(t+\tau)\hat{d}(t)\rangle \, dt. \tag{6.2.16}$$

$$G^{(2)}_{aa}(\tau) = \int \langle \hat{a}^\dagger(t)\hat{a}^\dagger(t+\tau)\hat{a}(t+\tau)\hat{a}(t)]\rangle \, dt, \tag{6.2.17}$$

and the second is the autocorrelation of the field intensity,

$$G^{(1)}_{n}(\tau) = \int \langle \hat{a}^\dagger(t)\hat{a}(t)\rangle \langle \hat{a}^\dagger(t+\tau)\hat{a}(t+\tau)\rangle \, dt \tag{6.2.18}$$

$$= \int \langle \hat{n}(t)\rangle \langle \hat{n}(t+\tau)\rangle \, dt. \tag{6.2.19}$$

Using the identity

$$\langle \hat{a}^\dagger(t)\hat{a}(t+\tau)\rangle = \langle \hat{a}^\dagger(t+\tau)\hat{a}(t)\rangle^*, \tag{6.2.20}$$

we see that the third term is the absolute square of the first-order correlation function,

$$|G^{(1)}_{a}(\tau)|^2 = \int \langle \hat{a}^\dagger(t+\tau)\hat{a}(t)\rangle \langle \hat{a}^\dagger(t)\hat{a}(t+\tau)\rangle \, dt. \tag{6.2.21}$$

We now have the second-order correlation function of the beam splitter outputs purely in terms of the intensity and first- and second-order correlation functions of the input fields:

$$G^{(2)}_{cd}(\tau) = G^{(2)}_{a}(\tau) + G^{(1)}_{n}(\tau) - |G^{(1)}_{a}(\tau)|^2 \tag{6.2.22}$$

As shown in Chapter 2, these may all be found through numerical solutions to the master equation. An important feature of this result is that, at $\tau = 0$, zero coincidence counts are seen, even if the photons are spectrally distinguishable. This leads to the characteristic HOM interference pattern in Fig. 6.5. The width of the dip narrows with increasing distinguishability.

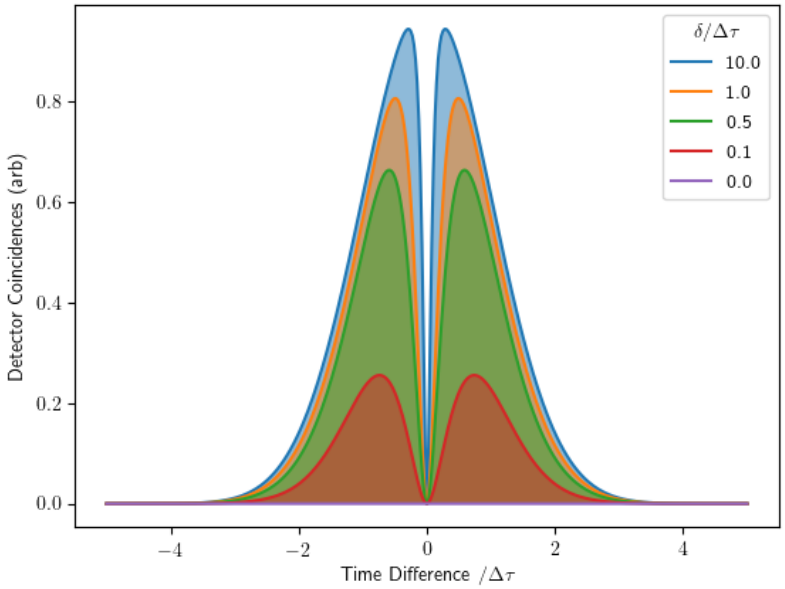

Figure 6.5: Hong-Ou-Mandel interference pattern for spectrally distinguishable photons. The STIRAP process is simulated for a range of laser linewidths δ as a fraction of pulse width $\Delta\tau$.

Until now we have assumed the input modes consist of a single polarisation, but we may extend our analysis by decomposing the fields into two orthogonal polarisation modes. If we take the polarisation of the input $\hat{a}$ to be horizontal, with that of $\hat{b}$ rotated by some angle ϕ, we may write the fields as

$$\hat{a}(t) = \hat{a}_H(t) \tag{6.2.23}$$

$$\hat{b}(t) = \cos(\phi)\hat{b}_H(t) + \sin(\phi)\hat{b}_V(t). \tag{6.2.24}$$

Substituting this into Eq. (6.2.7), we find

$$G^{(2)}_{cd}(\tau) = G^{(2)}_{aa}(\tau) + G^{(1)}_{n}(\tau) - \cos^2\phi|G^{(1)}_{a}(\tau)|^2. \tag{6.2.25}$$

As expected, when the fields have orthogonal polarisations ($\phi = \pi/2$), no interference occurs, and the output correlation function is only a function of the intensity and second-order coherence of the input fields. The effect of varying the polarisation on the HOM interference pattern is shown in Fig. 6.6.

6.3 The Experimental Setup

The experimental setup is shown in Fig. 6.7. Photons are emitted from the cavity at regular intervals through a repeated sequence of laser pulses. A quarter-wave plate transforms the cavity emission from circular to linear and a PBS filters out any photons of unwanted polarisation.

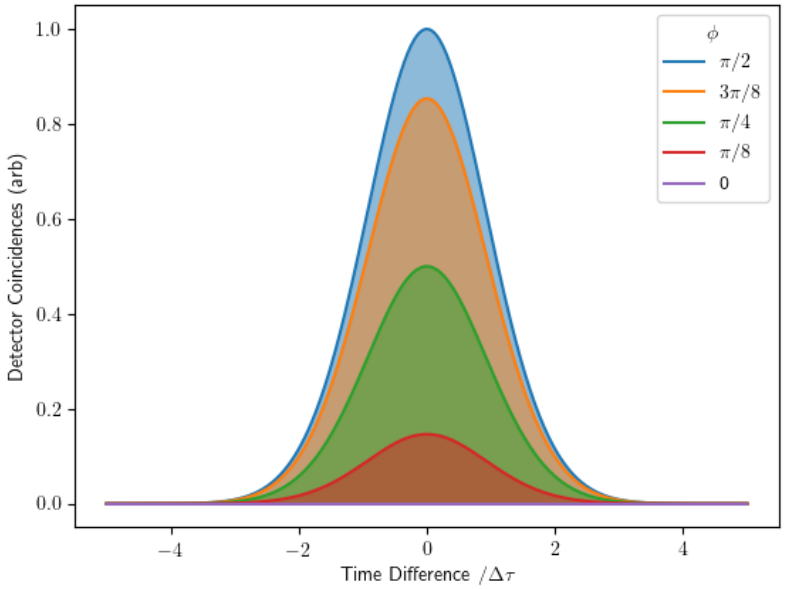

Figure 6.6: Hong-Ou-Mandel interference pattern for photons with relative linear polarisation angle ϕ.

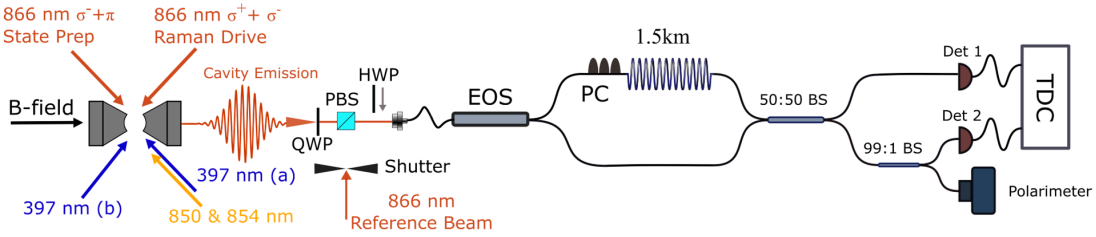

Figure 6.7: The experimental setup. The orientation and polarisation of the lasers are shown. The cavity emission is coupled into a fully fibre-spliced HOM interferometer.

Bandpass filters remove the cavity locking light. The cavity emission is then coupled into an adapted version of the HOM interferometer shown in Fig. 6.4. In place of the first beam splitter, a PM fibre-coupled electro-optical switch (EOS) is used to direct the light down a chosen channel. On arm of the switch, which we will call the direct arm, couples to a PM 50:50 fibre beam splitter (FBS). The other arm, which we will call the delay arm, couples through a 1.5 km single mode fibre spool. Polarisation control paddles (PC) allow the birefringence of the delay fibre to be adjusted, granting control over the polarisation of photons through the fibre. The delay fibre leads to the other input arm of the 50:50 FBS. One output arm of the beam splitter couples to a fibre leading to a SSPD. The other arm first couples through a PM 99:1 FBS before coupling to the other SSPD. The 99:1 FBS sends 1% of the photons to a polarimeter. All fibre-fibre connections were spliced to reduce the losses from butt-coupling. The splices all have transmissions of $> 90\%$.

As the delay fibre is not polarisation maintaining, the photons through the fibre experience a time-dependant polarisation drift with respect to the direct arm, as temperature changes and mechanical noise change the birefringence of the fibre. The fibre spool sits in a padded box to isolate it partially from mechanical noise, but there is no activate mechanical or temperature stabilisation. The polarimeter is therefore used in combination with the EOS to measure the polarisation of

photons through each arm, and the polarisation control paddles are used to correct for the drift. The drifts were typically on the order of a degree per minute, but this varied greatly hour-to-hour and day-to-day. The polarisation drift could be reduced by using a polarisation maintaining fibre instead; however, PM fibres typically cause greater attenuation than SM fibres, and the ability to actively control the polarisation of light through the fibre via the PC paddles would be lost. The polarimeter is not sensitive enough to detect single photons, so an 866 nm polarisation reference laser is used to measure the polarisation drift. The laser is overlapped with the cavity emission at the PBS, but is by default blocked by a mechanical switch. When polarisation drift is to be measured, the switch is opened and a half-wave place rotates the polarisation of the reference beam to match the axis of the PM fibres. Single photon generation is paused during this time. The light is directed first down the direct arm and the polarisation recorded. The light is then directed down the delay arm, and the polarisation control paddles adjusted to correct for the drift. This is done approximately every ten minutes.

Two sets of data were taken for each scheme: the parallel measurement, in which the polarisation of the photons through each arm were parallel at the FBS, and the perpendicular measurement, in which the photons through the delay arms were rotated 90° with respect to the direct arm. From these, the visibility of the interference, and therefore the distinguishability of the photons, was calculated.

6.3.1 Single photon sequence

The sequence of laser pulses used to produce single photons is shown in Fig. 6.8. The length of the sequence is 7.38 µs, fixed by the travel time through the delay line. For both schemes, the sequence is divided into 1.5 µs of cooling, 2.5 µs of state preparation, and a 2.5 µs single photon window. A 500 ns pause before and 380 ns pause after the single photon window allows the TDC to be gated such that it only accepts counts during this window. The magnetic field is set to 4.9 G to resolve the Raman transitions between different Zeeman sublevels.

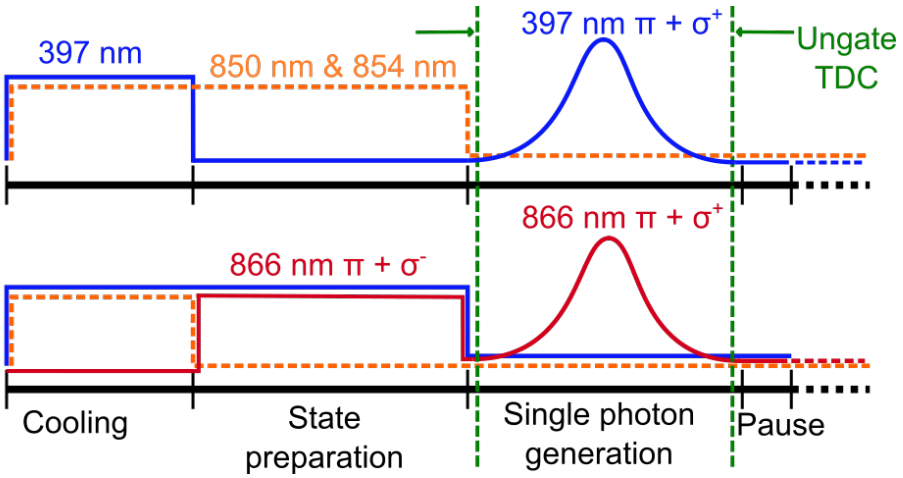

Figure 6.8: Pulse sequences for producing photons in the $S_{1/2} \rightarrow D_{3/2}$ (top) and $D_{3/2} \rightarrow D_{3/2}$ (bottom) schemes. Each is divided into cooling, state preparation, and single photon stages.

In the cooling stage, the 397 nm (a) beam blue-detuned $\Delta_{\text{cool}} = 2\gamma_{SP}$ from resonance Doppler cools the ion for 1.5 µs while 850 nm and 854 nm beams repump from the $D_{3/2}$ and $D_{5/2}$ levels. The ion is cooled to $1.4T_D$ and remains this temperature throughout.

The state preparation and single photon generation stages differ for each scheme. In the $S_{1/2} \rightarrow$

$D_{3/2}$ scheme, the ion is prepared across the Zeeman subelevels of $S_{1/2}$ by extinguishing the 397 nm beam and allowing repumpers to optically pump the ion. A Gaussian-shaped pulse of $\Delta_{\text{drive}} = 2\gamma_{SP}$ blue-detuned 397 nm light with width $\Delta\tau = 450$ ns and amplitude $\Omega_{\text{drive}} = \gamma_{SP}$ from beam (b) drives the cavity-STIRAP transition. In the $D_{3/2} \rightarrow D_{3/2}$ scheme, the ion is optically pumped into the $|\mathrm{D}_{3/2}; m_J = -3/2\rangle$ state using an on-resonance 866 nm beam polarised σ^+ and π and a 2γ blue-detuned 397 nm beam of mixed polarisation. $|\mathrm{D}_{3/2}; m_J = -3/2\rangle$ is a dark state for light of this polarisation, and so the ion is eventually pumped into this state (see Fig. 6.9). Simulations suggest that the ion should have 70 % of its population in this state at the end of the preparation stage. This is limited by the time available for state preparation. The cavity-STIRAP process is driven in this scheme by a $\Delta_{\text{drive}} = 2\gamma_{SP}$ red-detuned 866 nm pulse of width $\Delta\tau = 450$ ns and amplitude $\Omega_{\text{drive}} = 0.5\gamma_{SP}$. The polarisation of the drive beam is σ^+ and σ^-.

The constraint in the sequence length imposed by the length of the delay fibre means that is it is not as efficient as would be possible given an arbitrary amount of time. Ideally, optical pumping would be performed over a long time at low power. A shorter time can compensated for with higher laser power; however, this can lead to heating of the ion. Likewise, an increase in laser power can recover efficiency lost due the shorter time available for single photon generation, but this reduces the adiabaticity of the process. The laser parameters and relative lengths of the stages in the sequence were chosen to optimise empirically the single photon generation efficiency in both cases, given the time constraint. The optimal parameters were first estimated using simulations, and then iterated experimentally until the optimal values were found.

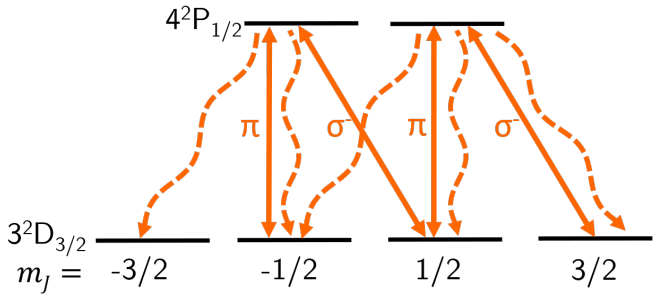

Figure 6.9: State preparation into the $|\mathrm{D}_{3/2}; m_J = -1/2\rangle$ state through optical pumping via a 866 nm laser with $\sigma^- + \pi$ polarisation. A 397 nm laser (not shown) excites the ion from $\mathrm{S}_{1/2}$to $\mathrm{D}_{3/2}$.

6.4 Results

As in the QFC experiment, the raw data are photon arrival times on the two TDC channels, gated during the single photon window. A histogram of arrival time differences is built, which is proportional to the second-order correlation function of the beam splitter outputs. The histogram for the $S_{1/2} \rightarrow D_{3/2}$ scheme with parallel polarisation is shown in Fig. 6.10, while the histogram for $D_{3/2} \rightarrow D_{3/2}$ is shown in Fig. 6.11. This histograms consists of peaks separated by the experimental sequence period T_{seq}. Due to the EOS, no photons from the cavity can arrive an odd number of periods apart, and so these peaks are suppressed. The counts here correspond only to coincidences between the signal and background, between pairs of background counts, or leakage through the switch. The peaks at even periods are larger than the at zero delay, again due to the action of the switch.

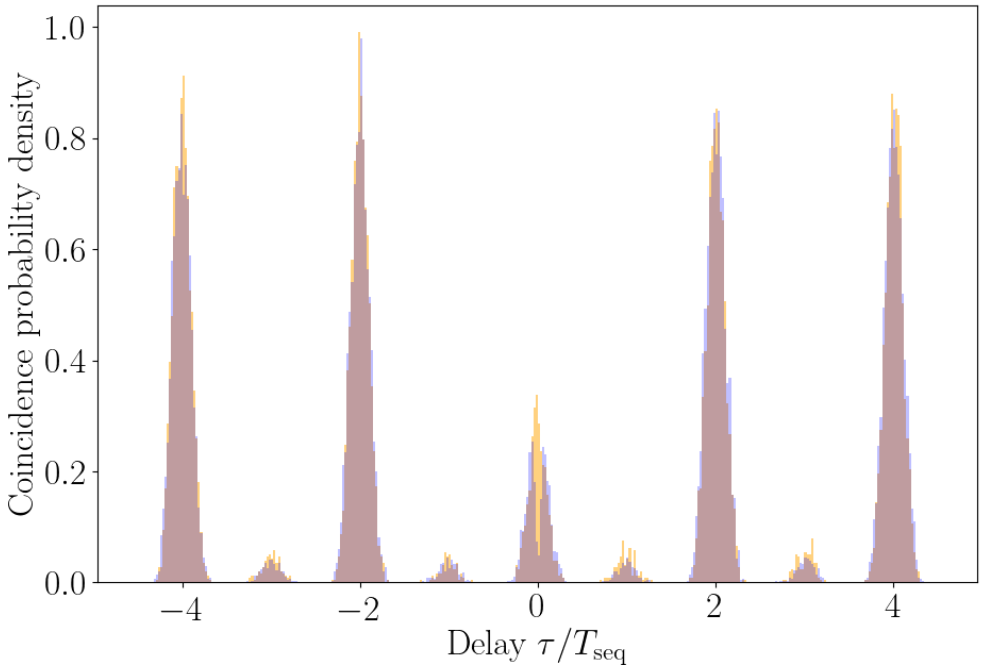

Figure 6.10: Coincidence probability density histogram from the $S_{1/2} \rightarrow D_{3/2}$ scheme with parallel (blue) and perpendicular (orange) polarisation, up to $\tau = 4.5T_{\mathrm{seq}}$. The coincidence probability density is given to account for the different total coincidence count for each polarisation. The bin width is 200 ns. The small peaks at odd multiples of T_{seq} are due to background counts and leakage through the EOM switch.

Single photons

The probability of photon detection versus time for the $S_{1/2} \rightarrow D_{3/2}$ and $D_{3/2} \rightarrow D_{3/2}$ schemes are shown in Fig. 6.12. This probability corresponds to a "photon shape" that is the the average over all possible coherent wavepackets. These photon shapes are constructed by comparing the arrival times at each detector with a trigger pulse sent every 256 cycles from the FPGA to a third TDC channel. The repetition rate was chosen to reduce the size of the file storing the timestamps. For the $S_{1/2} \rightarrow D_{3/2}$ scheme, the probability of detecting a single photon on either detector was $P_{\mathrm{det,SD}} = 0.360(3)\,\%$. The probability of emitting a photon can be estimated from the transmission efficiencies in the system. The transmission through each arm isn't equal, as there is signifiant attenuation through the delay fibre. This is measured as $\eta_{\mathrm{fibre}} = 0.44$, higher than the value of 0.35 expected from the specified attenuation of $3\,\mathrm{dB\,km^{-1}}$. The probability of emitting a photon is calculated as:

$$P_{\mathrm{emit}} = \frac{2P_{\mathrm{det}}}{\eta_{\mathrm{filter}}\eta_{\mathrm{coupling}}\eta_{\mathrm{BS}}\eta_{\mathrm{det}}\eta_{\mathrm{splice}}^2(1+\eta_{\mathrm{fibre}})(B + A\eta_{\mathrm{splice}}\eta_{\mathrm{tap}})} = 1.61\,\%, \tag{6.4.1}$$

where $\eta_{\mathrm{filter}} = 0.81$, $\eta_{\mathrm{coupling}} = 0.66$, $\eta_{\mathrm{det}} = 0.8$, and $\eta_{\mathrm{splice}} = 0.9$ are the measured efficiencies of the cavity bandpass filters, the collection fibre coupling, and the fibre splices respectively, and $A = 0.53$ and $B = 0.47$ are the branching fractions of the beam splitter. The reduced efficiency compared to the scheme in Chapter 5 ($P_{\mathrm{emit}} = 4.49\,\%$) can mostly be accounted for by considering the Clebsch-Gordan coefficient of the chosen transition ($\sqrt{1/2}$) and initial ion population. Simulations indicate an efficiency of 1.8 % should be achieved, indicating an additional 13 % loss not accounted for. This

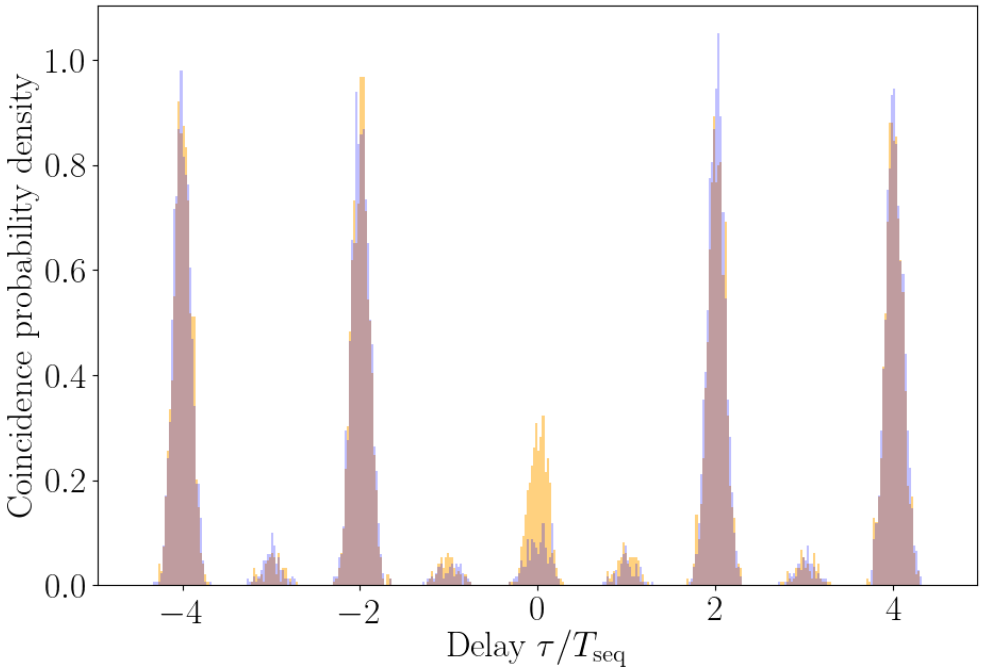

Figure 6.11: Coincidence probability density histogram from the $D_{3/2} \rightarrow D_{3/2}$ scheme with parallel (blue) and perpendicular (orange) polarisation, up to $\tau = 4.5T_{\mathrm{seq}}$. The coincidence probability density is given to account for the different total coincidence count for each polarisation. The bin width is 200 ns. The small peaks at odd multiples of T_{seq} are due to background counts and leakage through the EOM switch.

is similar to the 11 % reduced efficiency compared to simulations in the QFC experiment, indicating these losses are common between both experiments, for example in the detector efficiency.

For the $D_{3/2} \rightarrow D_{3/2}$ scheme, the detection probability was $P_{\mathrm{det,DD}} = 0.059\,04(3)\,\%$, giving an emission probability of $P_{\mathrm{emit,DD}} = 0.27\,\%$, using the above efficiencies. Part of the reduction in efficiency is due to the lower Clebsch-Gordan coefficient for this transition ($\sqrt{1/6}$). However, simulations suggest an emission efficiency of 0.75 % should be achieved. The source of this reduced efficiency is unclear. It is possibly a result of a lower state preparation efficiency than expected. The state preparation efficiency is strongly dependant on the 397 nm laser power, which is kept low to reduce heating, and the purity of the polarisation of the 866 nm state preparation beam. The results are consistent with 35 % population in the initial $|\mathrm{D}_{3/2}; m_J = -3/2\rangle$ state.

HOM interference patterns

The histograms for the parallel and perpendicular measurements must be normalised to calculate the visibility. However, there are polarisation dependencies in the fibre-coupled components of the setup, which affect the number of coincidences in each window. This must be accounted for when normalising the histograms. The fibre beam splitter has polarisation dependent losses, meaning the transmission is different in the parallel ($\eta_{\mathrm{BS},\parallel} = 0.86$) and perpendicular ($\eta_{\mathrm{BS},\perp} = 0.63$) cases. We define the combined transmissions through the delay fibre and beam splitter in the parallel and perpendicular cases as $\rho_{\parallel} = 0.38$ and $\rho_{\perp} = 0.28$, respectively. The branching ratios of the beam splitter also change depending on polarisation. The ratios for the direct arm and the delay arm with parallel polarisation are $A_{\parallel} = 0.53$ and $B_{\parallel} = 0.47$. With perpendicular polarisation, the

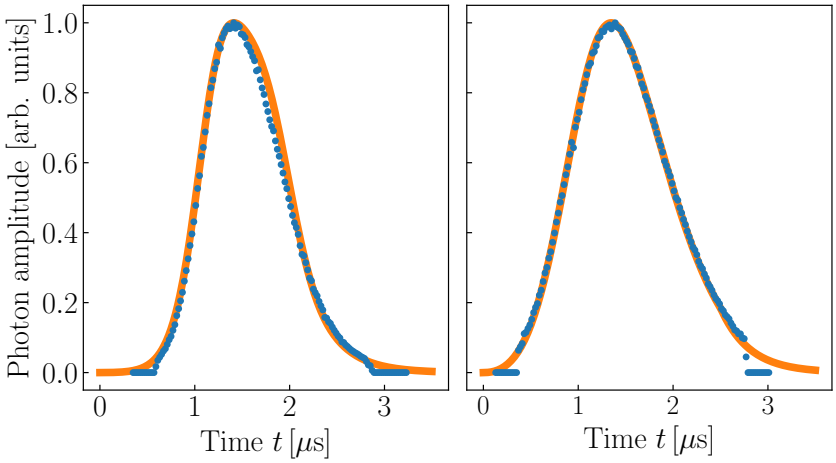

Figure 6.12: Temporal probability distribution of detecting single photon shown as blue dots for the $S_{1/2} \rightarrow D_{3/2}$ scheme (left) and $D_{3/2} \rightarrow D_{3/2}$ (right). To extract this plot, all the photon arrival times with respect to the sequence trigger during the measurements are sorted into 20 ns time bins and the resulting histograms are normalized to unity. The solid lines are the expected cavity population obtained by numerical simulation.

branching from the delay arm becomes $A_\perp = 0.75$ and $B_\perp = 0.25$. These imbalances affect the number of coincidences observed in the different peaks, and so must be considered when normalising HOM histograms. To account for the different number of coincidence counts for each data set, the histograms for perpendicular and parallel polarisations are scaled such that the average area under the peaks at $T = \pm 2$ is unity. The histogram for perpendicular polarisation is then scaled to account for the imbalance in transmission ratios and the branching ratios at the beam splitter by the scale factor

$$R = \frac{2A_\parallel B_\parallel \rho_\parallel}{(A_\parallel B_\perp + A_\perp B_\parallel)\rho_\perp}. \tag{6.4.2}$$

The normalised histograms are shown shown in 6.13. After scaling, the visibility is calculated as

$$V = 1 - \frac{\int_{T/2}^{-T/2} C_\parallel \mathrm{d}\tau}{\int_{T/2}^{-T/2} C_\perp \mathrm{d}\tau}, \tag{6.4.3}$$

where $C_\parallel$ and $C_\perp$ are the normalised coincidence counts for the parallel and perpendicular datasets respectively, and $T/2$ is the length of the single photon window. For the $S_{1/2} \rightarrow D_{3/2}$ scheme, a visibility of 50(2) % is calculated from the data, in agreement with the value of 53.0 % from the simulation to within 2σ. There is also good agreement between the shapes of the interference patterns, indicating the reliability of the simulations.

From the $D_{3/2} \rightarrow D_{3/2}$ data a visibility of 81(2) % is calculated. This is a clear improvement over the $S_{1/2} \rightarrow D_{3/2}$ scheme, demonstrating the improvement in the indistinguishability of photons produced by the new scheme. However, the simulations indicate that a visibility of 92.2 %should be achievable. Examining the interference pattern in Fig. 6.11, a flat offset in counts is seen, rather than the characteristic HOM dip. This indicates that the increase in counts is not due to distinguishability between the photons as they leave the cavity, but due to either a drift in polarisation that was not properly compensated, or a source of background counts that was not accounted for and was not present or apparent in the $S_{1/2} \rightarrow D_{3/2}$ case. We can estimate this polarisation drift we consider the polarisation dependence from Eq. (6.2.25) in the simulation and fit a value for the polarisation offset ϕ. In doing so, we find an average value of $\phi = 12$. Subtracting

the offset caused by this polarisation mismatch from the data, visibilities of 54(2) % and 89(2) % are calculated for $S_{1/2} \rightarrow D_{3/2}$ and $D_{3/2} \rightarrow D_{3/2}$, respectively, in closer agreement with the simulated values. This average offset is larger than the expected drift on the order a few degrees between polarisation corrections, implying that there may be contribution from other sources, such as a mode mismatch at the beam splitter or unexpected background counts, which would both have a similar effect on the interference pattern. However, the shape of the interference pattern indicates that the majority of the discrepancy from simulations is due to technical issues rather than photon distinguishability. The visibility demonstrated represents the best reported HOM visibility for an ion-cavity system to our knowledge.

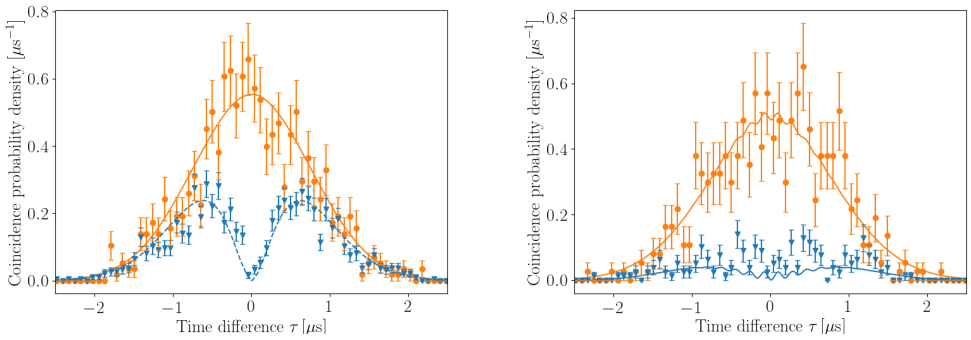

Figure 6.13: HOM interference pattern for the $S_{1/2} \rightarrow D_{3/2}$ scheme (left) and $D_{3/2} \rightarrow D_{3/2}$ scheme (right). Data for the parallel polarisation measurement are shown as green crosses, while data for the perpendicular polarisation measurement are shown as orange dots. Simulations are shown as dashed and solid lines respectively.

6.5 Comparison of the schemes

To compare the two schemes, we will look at their application to probabilistic entanglement schemes based on two-photon interference. The two figures of merit for an entanglement scheme of interest to us are the heralded entanglement rate R_{ent} and the fidelity F. In the entanglement scheme presented in [31], entanglement is generated between the electronic states of ions in distant traps and the polarisation states of emitted photons. The photons interfere at a beam splitter, and entanglement is heralded by a coincidence detection from perpendicularly polarised photons. Coincidences from partially distinguishable photons of parallel polarisation therefore constitute false-positives in the heralding. We can therefore write the fidelity in terms of the HOM visibility as $F = \frac{1+V}{2}$ [100]. Imperfect entanglement is acceptable if entanglement purification is employed [102]. This purification comes with a time and resources overhead that depends on the initial fidelity, and there is a minimum initial fidelity, so a higher fidelity is still desirable. The rate of entanglement is proportional to both the rate of photon emission R_{emit} and the rate of coincidence counts for perpendicularly polarised photons $R_{\perp}$. A higher rate of entanglement is desirable as it means faster network operations. The particular requirements for F and R_{ent}, and therefore V and R_{gen}, depend on the application and networking protocols used. The results of this experiment demonstrate how the choice of initial state can increase visibility at the cost of emission rate. There are other ways to improve the indistinguishability, which we will discuss here.

A commonly used technique is to temporally filter coincidence counts. Due to the shapes of the HOM interference patterns for parallel and perpendicular polarised photons, narrowing the maximum time T between detections considered reduces the rate of coincidences in the parallel

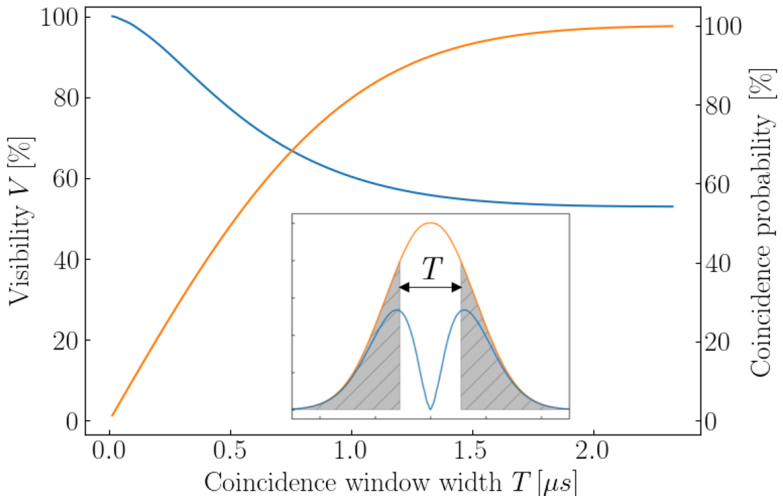

Figure 6.14: Visibility (blue) and coincidence count probability (orange) with varying window size T for the simulation of the $S_{1/2} \rightarrow D_{3/2}$ scheme. The coincidence count probability is normalised to the experimental rate. The insert demonstrates the temporal filtering; coincidences in the grey shaded area are neglected, increasing the visibility.

case faster than perpendicular, increasing the effective visibility. The visibility and coincidence rate as functions of the window width for the $S_{1/2} \rightarrow D_{3/2}$ scheme are shown in Fig. 6.14. For the experimental results presented here, For the visibility of the $S_{1/2} \rightarrow D_{3/2}$ results to exceed 81(2) %, a window of $T = 400$ ns is required, leaving 41 % of the collected coincidence counts. In comparison, the $D_{3/2} \rightarrow D_{3/2}$ scheme produces coincidence counts at a rate 3 % of the $S_{1/2} \rightarrow D_{3/2}$ scheme. However, if we instead compare the simulation results, with optimal state preparation, the schemes are more similar. To achieve the same visibility of 92.2 % from the simulation of the $D_{3/2} \rightarrow D_{3/2}$ scheme, a window of $T = 210$ ns is necessary. For this width, 23 % of coincidences are kept, while the simulated $D_{3/2} \rightarrow D_{3/2}$ scheme with optimal state preparation has a coincidence rate 53 % of the $S_{1/2} \rightarrow D_{3/2}$ scheme. Temporal filtering therefore only confers an advantage due to technical limitations such as the signal-background ratio and state preparation fidelity.

The visibility can also be improved by changing the experimental parameters of the single photon generation process. In this experiment, the laser parameters were chosen to maximise R_{emit} rather than the visibility. In either scheme, the visibility tends to increase as detuning increases and drive laser power decreases. This also reduces the single photon efficiency, and so again an efficiency-fidelity trade-off is made. Fig. 6.15 shows heat maps of the simulated visibilities and efficiencies for both schemes over a range of drive laser intensities and detunings. These simulations show that any given visibility can be achieved in the $D_{3/2} \rightarrow D_{3/2}$ scheme with a higher efficiency that would be possible with the $S_{1/2} \rightarrow D_{3/2}$ scheme. They also show the visibility in the $D_{3/2} \rightarrow D_{3/2}$ scheme is far less sensitive to laser parameters, with $V > 70\%$ over the entire parameter space examined.

In the far-detuned limit ($\Delta \gg \gamma_{SP}$), the population of the excited state tends to zero and an effective two-level system is formed [55]. The far-detuning method was used in another recent experiment in which the HOM interference between photons from $^{40}Ca^{+}$ coupled to an optical cavity was observed [43]. In this experiment, a visibility of $V_{SD} = 0.472(8)$ % was obtained. The visibility was found to be limited primarily by the spontaneous emission rate. While a direct

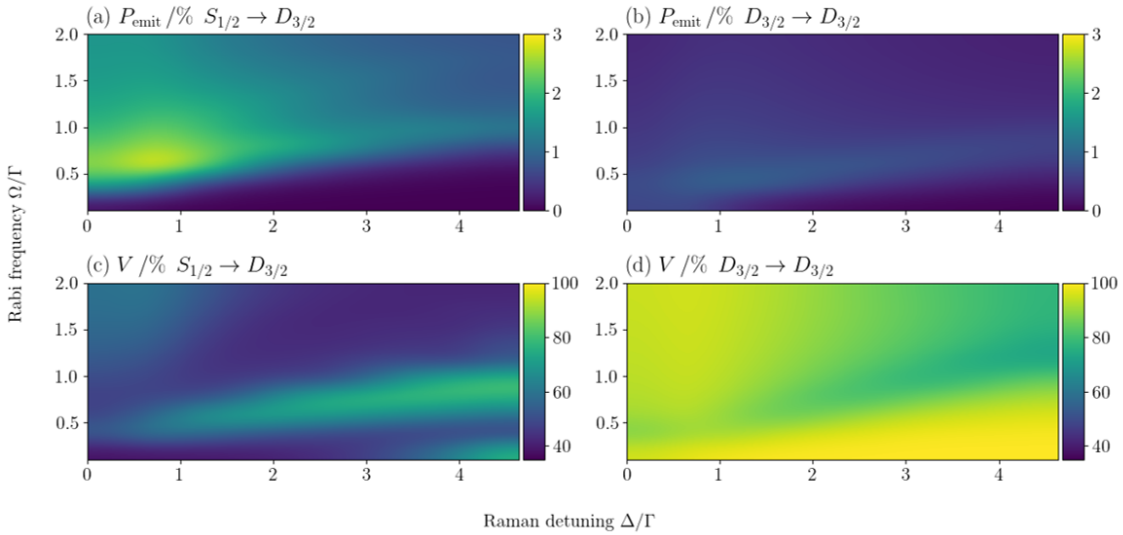

Figure 6.15: Simulated visibility and and emission probability for the $S_{1/2} \rightarrow D_{3/2}$ and $D_{3/2} \rightarrow D_{3/2}$ schemes plotted against Raman detuning and drive laser Rabi frequency in units of the transition linewidth Γ_{SD}. **(a)** $S_{1/2} \rightarrow D_{3/2}$ efficiency. **(b)** $D_{3/2} \rightarrow D_{3/2}$ efficiency. **(c)** $S_{1/2} \rightarrow D_{3/2}$ visibility. **(d)** $D_{3/2} \rightarrow D_{3/2}$ visibility.

comparison cannot be made between the experiments due to different experimental parameters (for example, cavity coupling and linewidth), this result shows that even in the far-detuned limit, the spontaneous emission rate is a key limiting factor to visibility.

The discrepancy in efficiency between the two schemes presented here is mainly due to the state preparation efficiency and Clebsch-Gordan coefficients of the transitions. A more favourable transition would be $|\mathrm{D}_{3/2}; m_J = -1/2\rangle \rightarrow |\mathrm{D}_{3/2}; m_J = 3/2\rangle$, which has the same Clebsch-Gordan coefficient as $|\mathrm{S}_{1/2}; m_J = -1/2\rangle \rightarrow |\mathrm{D}_{3/2}; m_J = 3/2\rangle$, $\sqrt{1/2}$. With perfect state preparation in each, both this scheme and $|\mathrm{S}_{1/2}; m_J = -1/2\rangle \rightarrow |\mathrm{D}_{3/2}; m_J = 3/2\rangle$ achieve similar single photon efficiencies according to numerical simulation (with laser parameters chosen to optimise efficiency). However, the difference in visibility is stark: $V = 0.96$ for $|\mathrm{D}_{3/2}; m_J = -1/2\rangle \rightarrow |\mathrm{D}_{3/2}; m_J = 3/2\rangle$ and $V = 0.54$ for $|\mathrm{S}_{1/2}; m_J = -1/2\rangle \rightarrow |\mathrm{D}_{3/2}; m_J = 3/2\rangle$. This means that this scheme is strictly superior to $S_{1/2} \rightarrow D_{3/2}$, provided the system can be initialised with high fidelity. Near-unity state preparation is feasible without a large time overhead; coherent state transfer using STIRAP in $^{40}\mathrm{Ca}^{+}$ has been demonstrated with 95 % efficiency, taking under 10 µs[103]. As the sequence length in this experiment was fixed by the length of the delay fibre, it was not possible to implement high-fidelity state preparation. However, this simply a feature of the HOM interferometer setup, and this limitation would not exist in a real quantum network. In long-distance networking, the repetition rate of the entanglement generation is limited by the travel time of the photon between nodes [89]. Therefore a small increase in state preparation time will not reduce the speed of entanglement generation in large networks. Over short distances, however, it may be a limiting factor.

6.6 Conclusion

We have shown how the choice of initial state in a cavity-assisted Raman transition can impact the distinguishability of the photons emitted from the cavity. Indistinguishable photons are a vital part of quantum networks, and the techniques demonstrated can be used in a variety of

systems and networking protocols. We have demonstrated through numerical simulation that measures to reduce the detrimental effects of spontaneous emission by changing laser parameters or temporally filtering coincidence counts do not reduce distinguishability enough to account for the loss of photon emission rate. By implementing coherent state transfer for high-fidelity state preparation, near-unity HOM visibility can be achieved with a $D_{3/2} \rightarrow D_{3/2}$ scheme without a significant loss of efficiency compared to the more typical $S_{1/2} \rightarrow D_{3/2}$ scheme for similar laser parameters. The visibility of 81(2) % measured in this experiment represents the highest visibility for photons from an ion-cavity system without subtraction of background or temporal filtering, due to the significantly lower detrimental effect of spontaneous decay on the photon coherence.

This result also brings trapped ions in line with the best reported visibilities from neutral atoms of $> 80\,\%$ [45, 46]. Neutral atoms have an advantage over ions in that it is much easier to achieve strong cavity coupling, diminishing the relative impact of decoherence effects. The results presented here demonstrate that this level of indistinguishability can be achieved even in weakly coupled atomic systems. As mentioned, HOM visibility is translatable to the fidelity of entanglement generation in remote ions; in this case, 91 % would be expected. The entanglement infidelity in turn contributes to the computational error rate. The tolerable error rate is typically on the order of 1 %, depending on the scheme being used [104, 105]. Entanglement purification protocols exist which reduce the tolerable error rate, but require a large overhead in time and number of qubits. Thus a HOM visibility of 99 % is desirable to create scalable quantum networks for fault-tolerant computing. The results from neutral atoms show that strong coupling is not enough to reach this threshold, but incorporating a single photon scheme such as the one demonstrated here into a strongly coupled trapped-ion systems could grant the required near-unity HOM visibility, along with increases in efficiency and photon generation rates, while benefiting from the long trapping times provided by rf traps. Other sources of decoherence, such as magnetic field instability and laser linewidth, also need to be minimised.

Quantum logic operations including two-photon gates and entanglement generation have been performed in a photonic chip fed by an atom-cavity system[106]. The HOM visibility measured using photons from this system was 85(5) % with an efficiency of $> 60\,\%$, and an entanglement fidelity of 82(10) % was achieved. This proof-of-principle experiment shows that applications such as linear optics quantum computing are within reach for already existing trapped-ion technologies with the photon indistinguishability shown here.

The technique for single photon generation shown here is a step towards realising trapped ions in cavities as a single photon source for a variety of quantum technology applications.

Chapter 7

Conclusions and Outlook

When this doctoral work was started, the ion trap, cavity, and most of the peripheral systems were already in place. In addition to adjustments and improvements to the system, such as the extension of the stability transfer lock to stabilise more lasers at one time, the setting up of new laser beams, the numerical simulation toolbox was rewritten to work with the Quantum Optics Toolbox in Python. The motivation behind this doctoral work was to develop and demonstrate techniques for quantum networking based on trapped ions coupled to optical cavities. To that end, two experiments were carried out focusing on the emission of single photons from the cavity.

In the first experiment, photons from the ion-cavity system were converted from near-infrared to a telecom C-band wavelength via quantum frequency conversion and transmitted over 10 km of optical fibre, where the nonclassical statistics of the photon source were verified without subtraction of background. This expands on previous work in which an ion-cavity system was used a single photon source [34]. Quantum frequency conversion to standard telecom wavelengths is expected to play a large role in building large-scale quantum networks, where the low attenuation in optical fibres allows for long-distance communication. This result was the first time QFC was demonstrated with an ion-cavity system, and the longest distance transmission of photons from a trapped ion. This is a significant step towards building quantum networks with trapped ions.

In the second experiment, a technique was demonstrated for producing indistinguishable single photons. Through careful selection of the initial state in a cavity-Raman transition, the destructive effects of spontaneous emission on the coherence of photons emitted from the cavity can be mitigated. This was shown experimentally with a large increase in HOM visibility (81(2) %) compared to a more conventional scheme in the same trap (50(2) %) and compares favourably with results from similar systems (47 %) when using the entire photon window [43]. This technique is readily applicable to other ion trap systems and ion species.

Numerical simulations of the system show that, by utilising coherent state transfer for high-fidelity state initialisation, both the efficiency of photon generation and indistinguishability of emitted photons can be further improved. The next step is to use this scheme to entangle the ion with a photon emitted from the cavity, potentially using frequency conversion to telecom as already demonstrated. From there, there are a several paths which could be explored. Firstly, it has been demonstrated that the trapped-ion-cavity system can couple up to five ions with $> 98\%$ coupling strength compared to a single ion, opening the door to the generation of multi-ion cluster states using the cavity. This has applications in both quantum information processing and quantum repeaters for quantum networking. Alternatively, the ion could be remotely entangled with an ion

in another trap, as has been demonstrated previously with trapped ions [31]. Utilising quantum frequency conversion, this other trap could be dozens of kilometres away [93]. Moving in a slightly different direction, the improved coherence in the single photon process could be utilised for time-bin encoding [107]. This paradigm of networking circumvents the issue of polarisation drift in optical fibres by encoding quantum information not in the photon's polarisation degree of freedom, but in its temporal profile. This requires a high degree of temporal coherence in the photon.

It is an incredibly exciting time to be working with trapped ions and optical cavities for quantum networking, and there are many paths yet to be explored.

Bibliography

1. Dowling, J. P. & Milburn, G. J. Quantum technology: the second quantum revolution. *Philosophical Transactions of the Royal Society of London. Series A: Mathematical, Physical and Engineering Sciences* **361,** 1655–1674 (2003) (cit. on p. 2).
2. Schrödinger, E. Are there quantum jumps? Part I. *The British Journal for the Philosophy of Science* **3,** 109–123 (1952) (cit. on p. 2).
3. Vengalattore, M. *et al.* High-resolution magnetometry with a spinor Bose-Einstein condensate. *Physical Review Letters* **98,** 200801 (2007) (cit. on p. 2).
4. Arute, F. *et al.* Quantum supremacy using a programmable superconducting processor. *Nature* **574,** 505–510 (2019) (cit. on p. 2).
5. Holevo, A. S. Bounds for the quantity of information transmitted by a quantum communication channel. *Problemy Peredachi Informatsii* **9,** 3–11 (1973) (cit. on p. 2).
6. Poplavskii, R. Thermodynamic models of information processes. *Soviet Physics Uspekhi* **18,** 222 (1975) (cit. on p. 2).
7. Ingarden, R. S. Quantum information theory. *Reports on Mathematical Physics* **10,** 43–72 (1976) (cit. on p. 2).
8. Benioff, P. The computer as a physical system: A microscopic quantum mechanical Hamiltonian model of computers as represented by Turing machines. *Journal of Statistical Physics* **22,** 563–591 (1980) (cit. on p. 2).
9. Feynman, R. P. Simulating physics with computers. *International Journal of Theoretical Physics* **21** (1999) (cit. on p. 2).
10. Deutsch, D. Quantum theory, the Church–Turing principle and the universal quantum computer. *Proceedings of the Royal Society of London. A. Mathematical and Physical Sciences* **400,** 97–117 (1985) (cit. on p. 2).
11. Friedenauer, A., Schmitz, H., Glueckert, J. T., Porras, D. & Schätz, T. Simulating a quantum magnet with trapped ions. *Nature Physics* **4,** 757–761 (2008) (cit. on p. 2).
12. Lanyon, B. P. *et al.* Universal digital quantum simulation with trapped ions. *Science* **334,** 57–61 (2011) (cit. on p. 2).
13. Shor, P. W. Polynomial-time algorithms for prime factorization and discrete logarithms on a quantum computer. *SIAM review* **41,** 303–332 (1999) (cit. on p. 2).
14. Grover, L. K. *A fast quantum mechanical algorithm for database search* in *Proceedings of the twenty-eighth annual ACM symposium on Theory of computing* (1996), 212–219 (cit. on p. 2).
15. Monroe, C. *et al.* Large-scale modular quantum-computer architecture with atomic memory and photonic interconnects. *Physical Review A* **89,** 022317 (2014) (cit. on p. 2).
16. Kimble, H. J. The quantum internet. *Nature* **453,** 1023–1030 (2008) (cit. on p. 2).
17. DiVincenzo, D. P. The physical implementation of quantum computation. *Fortschritte der Physik: Progress of Physics* **48,** 771–783 (2000) (cit. on p. 3).

18. Seidelin, S. *et al.* Microfabricated surface-electrode ion trap for scalable quantum information processing. *Physical Review Letters* **96,** 253003 (2006) (cit. on p. 3).
19. Harty, T. P. *et al.* High-Fidelity Preparation, Gates, Memory, and Readout of a Trapped-Ion Quantum Bit. *Physical Review Letters* **113,** 220501 (22 Nov. 2014) (cit. on p. 3).
20. Wang, Y. *et al.* Single-qubit quantum memory exceeding ten-minute coherence time. *Nature Photonics* **11,** 646 (2017) (cit. on p. 3).
21. Akerman, N., Navon, N., Kotler, S., Glickman, Y. & Ozeri, R. Universal gate-set for trapped-ion qubits using a narrow linewidth diode laser. *New Journal of Physics* **17,** 113060 (2015) (cit. on p. 3).
22. Ballance, C. J., Harty, T. P., Linke, N. M., Sepiol, M. A. & Lucas, D. M. High-Fidelity Quantum Logic Gates Using Trapped-Ion Hyperfine Qubits. *Physical Review Letters* **117,** 060504 (6 Aug. 2016) (cit. on p. 3).
23. Schäfer, V. *et al.* Fast quantum logic gates with trapped-ion qubits. *Nature* **555,** 75–78 (2018) (cit. on p. 3).
24. Walther, H., Varcoe, B. T., Englert, B.-G. & Becker, T. Cavity quantum electrodynamics. *Reports on Progress in Physics* **69,** 1325 (2006) (cit. on p. 3).
25. Cirac, J. I., Zoller, P., Kimble, H. J. & Mabuchi, H. Quantum state transfer and entanglement distribution among distant nodes in a quantum network. *Physical Review Letters* **78,** 3221 (1997) (cit. on p. 3).
26. Takahashi, H., Kassa, E., Christoforou, C. & Keller, M. Strong coupling of a single ion to an optical cavity. *Physical Review Letters* **124,** 013602 (2020) (cit. on p. 3).
27. Stute, A. *et al.* Quantum-state transfer from an ion to a photon. *Nature photonics* **7,** 219 (2013) (cit. on p. 3).
28. Boozer, A. D., Boca, A., Miller, R., Northup, T. E. & Kimble, H. J. Reversible state transfer between light and a single trapped atom. *Physical Review Letters* **98,** 193601 (2007) (cit. on p. 3).
29. Duan, L.-M., Lukin, M. D., Cirac, J. I. & Zoller, P. Long-distance quantum communication with atomic ensembles and linear optics. *Nature* **414,** 413–418 (2001) (cit. on p. 4).
30. Duan, L.-M. & Kimble, H. Efficient engineering of multiatom entanglement through single-photon detections. *Physical Review Letters* **90,** 253601 (2003) (cit. on p. 4).
31. Moehring, D. *et al.* Entanglement of single-atom quantum bits at a distance. *Nature* **449,** 68–71 (2007) (cit. on pp. 4, 77, 82).
32. Stephenson, L. *et al.* High-rate, high-fidelity entanglement of qubits across an elementary quantum network. *Physical Review Letters* **124,** 110501 (2020) (cit. on p. 4).
33. Barros, H. *et al.* Deterministic single-photon source from a single ion. *New Journal of Physics.* **11,** 103004 (2009) (cit. on pp. 4, 5, 16).
34. Keller, M., Lange, B., Hayasaka, K., Lange, W. & Walther, H. Continuous generation of single photons with controlled waveform in an ion-trap cavity system. *Nature* **431,** 1075 (2004) (cit. on pp. 4, 14, 16, 81).
35. Stute, A. *et al.* Tunable ion–photon entanglement in an optical cavity. *Nature* **485,** 482 (2012) (cit. on pp. 4, 64).
36. Casabone, B. *et al.* Heralded entanglement of two ions in an optical cavity. *Physical Review Letters* **111,** 100505 (2013) (cit. on pp. 4, 5).
37. Hong, C.-K., Ou, Z.-Y. & Mandel, L. Measurement of subpicosecond time intervals between two photons by interference. *Physical Review Letters* **59,** 2044 (1987) (cit. on pp. 4, 66).
38. O'brien, J. L. Optical quantum computing. *Science* **318,** 1567–1570 (2007) (cit. on p. 5).

39. Shor, P. W. & Preskill, J. Simple proof of security of the BB84 quantum key distribution protocol. *Physical review letters* **85,** 441 (2000) (cit. on p. 5).
40. Ha, N. *et al.* Single photon emission from droplet epitaxial quantum dots in the standard telecom window around a wavelength of 1.55 μm. *Applied Physics Express* **13,** 025002 (2020) (cit. on p. 5).
41. Senellart, P., Solomon, G. & White, A. High-performance semiconductor quantum-dot single-photon sources. *Nature nanotechnology* **12,** 1026 (2017) (cit. on p. 5).
42. Higginbottom, D. B. *et al.* Pure single photons from a trapped atom source. *New Journal of Physics* **18,** 093038 (2016) (cit. on pp. 5, 61).
43. Meraner, M. *et al.* Indistinguishable photons from a trapped-ion quantum network node. *Physical Review A* **102,** 052614 (2020) (cit. on pp. 5, 78, 81).
44. McKeever, J. *et al.* Deterministic generation of single photons from one atom trapped in a cavity. *Science* **303,** 1992–1994 (2004) (cit. on p. 5).
45. Specht, H. P. *et al.* Phase shaping of single-photon wave packets. *Nature Photonics* **3,** 469–472 (2009) (cit. on pp. 5, 80).
46. Nisbet-Jones, P. B., Dilley, J., Ljunggren, D. & Kuhn, A. Highly efficient source for indistinguishable single photons of controlled shape. *New Journal of Physics.* **13,** 103036 (2011) (cit. on pp. 5, 15, 80).
47. Sinha, U. *et al.* Single-photon sources. *Optics and Photonics News* **30,** 32–39 (2019) (cit. on p. 5).
48. Eisaman, M. D., Fan, J., Migdall, A. & Polyakov, S. V. Invited review article: Single-photon sources and detectors. *Review of scientific instruments* **82,** 071101 (2011) (cit. on p. 5).
49. Begley, S., Vogt, M., Gulati, G. K., Takahashi, H. & Keller, M. Optimized Multi-Ion Cavity Coupling. *Physical Review Letters* **116,** 223001 (22 May 2016) (cit. on p. 5).
50. Johansson, J. R., Nation, P. D. & Nori, F. QuTiP 2: A Python framework for the dynamics of open quantum systems. *Computer Physics Communications* **184,** 1234–1240 (2013) (cit. on p. 7).
51. Tan, S. M. A computational toolbox for quantum and atomic optics. *Journal of Optics B: Quantum and Semiclassical Optics* **1,** 424 (1999) (cit. on p. 7).
52. Law, C. & Kimble, H. Deterministic generation of a bit-stream of single-photon pulses. *Journal of Modern Optics* **44,** 2067–2074 (1997) (cit. on p. 14).
53. Kuhn, A., Hennrich, M., Bondo, T. & Rempe, G. Controlled generation of single photons from a strongly coupled atom-cavity system. *Applied Physics B* **69,** 373–377 (1999) (cit. on p. 14).
54. Bergmann, K., Vitanov, N. V. & Shore, B. W. Perspective: Stimulated Raman adiabatic passage: The status after 25 years. *The Journal of Chemical Physics* **142,** 170901 (2015) (cit. on p. 15).
55. Maurer, C., Becher, C., Russo, C., Eschner, J. & Blatt, R. A single-photon source based on a single Ca+ ion. *New Journal of Physics* **6,** 94 (2004) (cit. on pp. 15, 78).
56. Ballance, T. *et al.* Cavity-induced backaction in Purcell-enhanced photon emission of a single ion in an ultraviolet fiber cavity. *Physical Review A* **95,** 033812 (2017) (cit. on p. 16).
57. Müller, P. & Eschner, J. Single calcium-40 ion as quantum memory for photon polarization: a case study. *Applied Physics B* **114,** 303–306 (2014) (cit. on p. 17).
58. Plankensteiner, D., Schachenmayer, J., Ritsch, H. & Genes, C. Laser noise imposed limitations of ensemble quantum metrology. *Journal of Physics B: Atomic, Molecular and Optical Physics* **49,** 245501 (2016) (cit. on p. 19).

59. Khan, S., Kumar, M. P., Bharti, V. & Natarajan, V. Coherent population trapping (CPT) versus electromagnetically induced transparency (EIT). *The European Physical Journal D* **71,** 1–9 (2017) (cit. on p. 19).
60. Hettrich, M. *et al.* Measurement of dipole matrix elements with a single trapped ion. *Physical Review Letters* **115,** 143003 (2015) (cit. on p. 19).
61. Gosselin, R. N., Pinnington, E. & Ansbacher, W. Measurement of the lifetimes of the 4p levels in Ca i i using laser excitation of a fast beam. *Physical Review A* **38,** 4887 (1988) (cit. on p. 19).
62. Gerritsma, R. *et al.* Precision measurement of the branching fractions of the 4p 2 P 3/2 decay of Ca II. *The European Physical Journal D* **50,** 13–19 (2008) (cit. on p. 19).
63. Kreuter, A. *et al.* Experimental and theoretical study of the 3 d D 2–level lifetimes of Ca+ 40. *Physical Review A* **71,** 032504 (2005) (cit. on p. 19).
64. Gardiner, C. W. & Collett, M. Input and output in damped quantum systems: Quantum stochastic differential equations and the master equation. *Physical Review A* **31,** 3761 (1985) (cit. on p. 22).
65. Gardiner, C., Zoller, P. & Zoller, P. *Quantum noise: a handbook of Markovian and non-Markovian quantum stochastic methods with applications to quantum optics* (Springer Science & Business Media, 2004) (cit. on p. 23).
66. Foot, C. J. *et al. Atomic Physics* (Oxford University Press, 2005) (cit. on p. 25).
67. Brown, L. S. & Gabrielse, G. Geonium theory: Physics of a single electron or ion in a Penning trap. *Reviews of Modern Physics* **58,** 233 (1986) (cit. on p. 25).
68. Seymour-Smith, N. R. *Ion-trap cavity QED system for probabilistic entanglement* PhD thesis (University of Sussex, 2012) (cit. on pp. 26, 30, 32, 38, 41).
69. Begley, S. P. *Optimisation of the coupling of ion strings to an optical cavity* PhD thesis (University of Sussex, 2016) (cit. on p. 30).
70. Vogt, M. O. *Toward coherent ion-cavity coupling* PhD thesis (University of Sussex, 2017) (cit. on pp. 30–32, 39, 40, 42, 45, 46).
71. Herskind, P. F., Dantan, A., Albert, M., Marler, J. P. & Drewsen, M. Positioning of the rf potential minimum line of a linear Paul trap with micrometer precision. *Journal of Physics B: Atomic, Molecular and Optical Physics* **42,** 154008 (2009) (cit. on p. 32).
72. Berkeland, D., Miller, J., Bergquist, J. C., Itano, W. M. & Wineland, D. J. Minimization of ion micromotion in a Paul trap. *Journal of applied physics* **83,** 5025–5033 (1998) (cit. on p. 34).
73. Chuah, B. L., Lewty, N. C., Cazan, R. & Barrett, M. D. Detection of ion micromotion in a linear Paul trap with a high finesse cavity. *Optics Express* **21,** 10632–10641 (2013) (cit. on p. 34).
74. Donley, E. A., Heavner, T. P., Levi, F., Tataw, M. & Jefferts, S. R. Double-pass acousto-optic modulator system. *Review of Scientific Instruments* **76,** 063112 (2005) (cit. on p. 37).
75. Seymour-Smith, N., Blythe, P., Keller, M. & Lange, W. Fast scanning cavity offset lock for laser frequency drift stabilization. *Review of Scientific Instruments* **81,** 075109 (2010) (cit. on p. 39).
76. Diedrich, F., Bergquist, J., Itano, W. M. & Wineland, D. Laser cooling to the zero-point energy of motion. *Physical Review Letters* **62,** 403 (1989) (cit. on p. 41).
77. Roos, C. *et al.* Experimental demonstration of ground state laser cooling with electromagnetically induced transparency. *Physical Review Letters* **85,** 5547 (2000) (cit. on p. 41).
78. Kassa, E. *Single ion coupled to a high-finesse optical fibre cavity for cQED in the strong coupling regime* PhD thesis (University of Sussex, 2017) (cit. on p. 43).

79. Briegel, H.-J., Dür, W., Cirac, J. I. & Zoller, P. Quantum repeaters: the role of imperfect local operations in quantum communication. *Physical Review Letters* **81,** 5932 (1998) (cit. on p. 47).
80. Kumar, P. Quantum frequency conversion. *Optics letters* **15,** 1476–1478 (1990) (cit. on p. 47).
81. Rakher, M. T., Ma, L., Slattery, O., Tang, X. & Srinivasan, K. Quantum transduction of telecommunications-band single photons from a quantum dot by frequency upconversion. *Nature Photonics* **4,** 786–791 (2010) (cit. on p. 47).
82. De Greve, K. *et al.* Quantum-dot spin–photon entanglement via frequency downconversion to telecom wavelength. *Nature* **491,** 421 (2012) (cit. on p. 47).
83. Radnaev, A. *et al.* A quantum memory with telecom-wavelength conversion. *Nature Physics* **6,** 894–899 (2010) (cit. on p. 47).
84. Dudin, Y. O. *et al.* Entanglement of light-shift compensated atomic spin waves with telecom light. *Physical Review Letters* **105,** 260502 (2010) (cit. on p. 47).
85. Farrera, P., Maring, N., Albrecht, B., Heinze, G. & de Riedmatten, H. Nonclassical correlations between a C-band telecom photon and a stored spin-wave. *Optica* **3,** 1019–1024 (2016) (cit. on p. 47).
86. Ikuta, R. *et al.* Heralded single excitation of atomic ensemble via solid-state-based telecom photon detection. *Optica* **3,** 1279–1284 (2016) (cit. on p. 47).
87. Walker, T. *et al.* Long-distance single photon transmission from a trapped ion via quantum frequency conversion. *Physical Review Letters* **120,** 203601 (2018) (cit. on pp. 47, 48, 61).
88. Bock, M. *et al.* High-fidelity entanglement between a trapped ion and a telecom photon via quantum frequency conversion. *Nature Communications* **9,** 1–7 (2018) (cit. on pp. 47, 61, 64).
89. Krutyanskiy, V. *et al.* Light-matter entanglement over 50 km of optical fibre. *npj Quantum Information* **5,** 1–5 (2019) (cit. on pp. 47, 61, 64, 79).
90. Tanzilli, S. *et al.* A photonic quantum information interface. *Nature* **437,** 116–120 (2005) (cit. on p. 47).
91. Ikuta, R. *et al.* Wide-band quantum interface for visible-to-telecommunication wavelength conversion. *Nature Communications* **2,** 1544 (2011) (cit. on p. 47).
92. Ikuta, R. *et al.* High-fidelity conversion of photonic quantum information to telecommunication wavelength with superconducting single-photon detectors. *Physical Review A* **87,** 010301 (2013) (cit. on p. 47).
93. Yu, Y. *et al.* Entanglement of two quantum memories via fibres over dozens of kilometres. *Nature* **578,** 240–245 (2020) (cit. on pp. 47, 61, 82).
94. Boyd, R. W. *Nonlinear optics* (Academic press, 2019) (cit. on p. 48).
95. Maring, N. Quantum frecuency conversion for hybrid quantum networks (2018) (cit. on p. 48).
96. Becher, C. *et al.* Nonclassical radiation from a single self-assembled InAs quantum dot. *Physical Review B* **63,** 121312 (2001) (cit. on p. 58).
97. Cirac, J., Van Enk, S., Zoller, P., Kimble, H. & Mabuchi, H. Quantum communication in a quantum network. *Physica Scripta* **1998,** 223 (1998) (cit. on p. 64).
98. Simon, C. & Irvine, W. T. Robust long-distance entanglement and a loophole-free Bell test with ions and photons. *Physical Review Letters* **91,** 110405 (2003) (cit. on p. 64).
99. Maunz, P. *et al.* Quantum interference of photon pairs from two remote trapped atomic ions. *Nature Physics* **3,** 538 (2007) (cit. on p. 64).

100. Craddock, A. *et al.* Quantum interference between photons from an atomic ensemble and a remote atomic ion. *Physical Review Letters* **123,** 213601 (2019) (cit. on pp. 64, 77).
101. Crocker, C. *et al.* High purity single photons entangled with an atomic qubit. *Optics express* **27,** 28143–28149 (2019) (cit. on p. 64).
102. Dür, W., Briegel, H.-J., Cirac, J. I. & Zoller, P. Quantum repeaters based on entanglement purification. *Physical Review A* **59,** 169 (1999) (cit. on p. 77).
103. Sørensen, J. L. *et al.* Efficient coherent internal state transfer in trapped ions using stimulated Raman adiabatic passage. *New Journal of Physics* **8,** 261 (2006) (cit. on p. 79).
104. Knill, E. Quantum computing with realistically noisy devices. *Nature* **434,** 39–44 (2005) (cit. on p. 80).
105. Raussendorf, R. & Harrington, J. Fault-tolerant quantum computation with high threshold in two dimensions. *Physical review letters* **98,** 190504 (2007) (cit. on p. 80).
106. Holleczek, A. *et al.* Quantum logic with cavity photons from single atoms. *Physical review letters* **117,** 023602 (2016) (cit. on p. 80).
107. Brendel, J., Gisin, N., Tittel, W. & Zbinden, H. Pulsed energy-time entangled twin-photon source for quantum communication. *Physical Review Letters* **82,** 2594 (1999) (cit. on p. 82).